Hydrogen Permeation through Low Alloy Steels

Neruda Barakat

Submitted for the degree of Doctor of Philosophy

Heriot-Watt University

School of Engineering and Physical Sciences

August 2009

Abstract

A sensitive method of measuring hydrogen permeation is presented, whereby hydrogen is introduced to the entry side of a thin metallic membrane by applying a sinusoidal oscillation about an appropriate value of electrical potential to a cell containing 0.1N NaOH. The corresponding current is taken as the hydrogen incident flux to the surface. The exit side of the membrane is in contact with an ultra-high vacuum chamber where hydrogen partial pressure is measured using a mass spectrometer against a known pump rate in order to obtain a measure of the exit flux. Measurements have been made on a thin nickel membrane as a material with well known and stable hydrogen permeation parameters, and these have been used to assess the sensibility of the technique. A newly developed mathematical model is presented that uses Fourier analysis to determine the phase lag (φ) and amplitude ratio (Λ) between the current or potential and hydrogen partial pressure. Analytical relationships between (φ), (Λ) and the applied frequency (the newly introduced parameter) have been used to determine the relevant thermodynamic and kinetic parameters (such as hydrogen diffusion coefficient and solubility) which enable the effects of both surface and bulk kinetics to be distinguished. Results from the experiments on nickel showed a very good consistency with the literature [diffusion coefficient, $D = (3.6\pm0.5)\times10^{-14}$ and $(1.8\pm0.29)\times10^{-13}$ m^2/s at 22°C and 60°C, respectively, and solubility of $(2.11\pm0.09)\times10^{-2}$ and $(3.2\pm0.18)\times10^{-2}$ mol $H_2/m^3mbar^{0.5}$ at 22°C and 60°C, respectively]; this formed a well established calibration for undertaking and interpreting experiments on heat-treatable En24 low alloy steel. Permeation experiments were done for three heat treatment conditions and the results for diffusion coefficient were $(6\pm1)\times10^{-10}$ m^2/s for the annealed, $(7.89\pm1.2)\times10^{-12}$ m^2/s for the quenched and $(3.25\pm0.8)\times10^{-11}$ m^2/s for the quenched and tempered condition. Solubilities were $(5.3\pm1.5)\times10^{-9}$ for the annealed, $(3.28\pm0.94)\times10^{-5}$ for the quenched and $(1.22\pm0.6)\times10^{-7}$ mol $H_2/m^3mbar^{0.5}$ for the quenched and tempered condition and trapping parameters measured here were $\frac{kN}{p} = 7$, $\frac{kN}{p} = 834$ and $\frac{kN}{p} = 2055$, respectively. Results from these experiments helped to explain the variability reported in the literature for the values of the diffusion coefficient and solubility. The differences in behaviour from classical permeation are more easily attributed to trapping than to surface kinetic effects.

Dedication

To the memory of my uncle Safwan and grandmother Nazeera

To my wonderful family; Mum Nawal and Dad Talal, sisters Hala and Nora, and my beautiful niece, Nesma. I love you all so much.

Acknowledgements

I would like to express my gratitude to my supervisor Professor R. L. Reuben for his invaluable support throughout the period of my research. It has been a great pleasure working under his supervision and learning from his amazing experience.

My thanks will go too to members of staff and postgraduate students in the School of Engineering and Physical Sciences who provided help when I needed it; I would like to give a special thank you to Mr Iain Drummond for his outstanding support and suggestions.

This research was funded by Tishreen University, Syria, under the Capacity Building Project contracted between the Syrian Ministry of Higher Education and the British Council.

Table of Contents

List of Tables

List of Figures

Chapter 1

Introduction

1.1 Background: Hydrogen Damage as a Technological Problem

Hydrogen may be introduced into steels by a wide range of industrial processes such as electroplating, acid pickling, welding (Popov et al., 1994, Merrick, 1989), cathodic over-protection or corrosion (Yen and Huang, 2003, Warren, 1987). The last of these is particularly prevalent in the oil and gas industry where produced fluids containing hydrogen sulphide and/or the activity of sulphate reducing bacteria (SRB) can give rise to high chemical potentials of hydrogen.

Hydrogen can only dissolve monatomically in steels due to its nature as an interstitial solute, given the average size of interstitial sites. To dissolve, atoms must first adsorb onto the steel surface before being absorbed by it. Upon encountering defects such as voids, inclusions and carbides, atomic hydrogen diffusing into the steel lattice can recombine to form hydrogen molecules which are too big to migrate and therefore become trapped. Because of its high chemical potential, this hydrogen gas is present at a very high partial pressure which can lead to local cracking in more brittle steels or, in very ductile steels, a gas blister can build up and may split the metal.

Hydrogen embrittlement (HE) is the general term used to describe the effect of dissolved hydrogen on the mechanical properties of steels. It happens as a result of hydrogen atoms interfering with dislocation movement inside the steel lattice (Warren, 1987) which results in a greater susceptibility to cracking (general or local) of the steel part.

Depending on the strength level of the steel and its stress-state, there may be different forms or mechanisms of hydrogen damage (Owczarek and Zakroczymski, 2001). In lower strength steels (which normally have a lower level of other interstitial solutes, notably carbon) the type of internal damage resulting from dissolved hydrogen is most likely to involve blistering, whereas higher strength steels will crack near sites of evolving hydrogen as the stress concentrations at the periphery of the blister lead to cracking of the adjacent embrittled steel (known as HIC, hydrogen induced cracking). There have been many proposed detailed mechanisms for HIC and hydrogen

embrittlement involving decohesion, hydride formation, enhanced plastic flow and transport models (Maroef et al., 2002) each of which may be considered to contribute to hydrogen damage.

All steels which have a surface tensile stress (residual or applied) may suffer from stress corrosion in the presence of hydrogen, the susceptibility being greater for higher strength steels. Sulphide stress corrosion cracking (SSCC) (sometimes referred to as SSC) is known to be a very serious problem in the oil industry, particularly in areas where high pressure and high temperature produced fluids contain a high concentration of H_2S. In this type of failure, hydrogen atoms are generated on the surface at stress concentrations, diffusing short distances into the steel to microstructural defects where they become trapped generating opening stresses around these defects, cracking being aided by the surface tensile stress (Timmins, 1997). The severity of such damage depends on the steel composition, strength, microstructure and applied or residual stress levels, as well as the severity of the environment, described principally by H_2S partial pressure and temperature. Such problems, especially encountered in the oil industry, were addressed by the (US) National Association of Corrosion Engineers (NACE) by designing standard material requirements e.g. MR-01-75 (NACE, 1984) to solve industrial problems related to sulphide stress cracking, and standard test methods e.g. TM-01-77 (NACE, 1977) to determine the resistance of metals, particularly steels, to hydrogen induced cracking and sulphide stress cracking. This last standard was revised in 2005 to deal with the resistance of metals to both sulphide stress cracking and stress corrosion cracking in H_2S environments (NACE, 2005).

For any hydrogen damage phenomenon to occur, susceptible steels and environments capable of producing atomic hydrogen are required. The susceptibility of steels to hydrogen cracking depends primarily upon their metallurgical condition (for ferritic steel, this can be assessed by hardness) and upon the nature and size of inclusions which can act as initiating sites for hydrogen evolution.

In general, ferritic and martensitic steels are more vulnerable to hydrogen damage than austenitic steels partly due to lower hydrogen diffusivity in FCC than in BCC steels (Iacoviello et al., 1998) but, more significantly, due to the higher solubility of interstitials (both carbon and hydrogen) in austenite, leading to a greater tolerance to dissolved hydrogen. However, this very tolerance means that austenitic steels are not as

easily strengthened as are ferritic ones, and duplex stainless steels (DSSs) are sometimes used instead of austenitic grades for their cost efficiency (principally due to the lower levels of chromium and nickel) and their higher mechanical properties and corrosion resistance (Owczarek and Zakroczymski, 2001). However, DSSs can also experience hydrogen embrittlement when in contact with environments containing sulphides (due to their ferrite content) and SCC in chlorides (due to their austenite content), the combined synergistic effect being a matter of concern for corrosion engineers.

The examination of events taking place as hydrogen atoms transport through the metal is considered an important tool in understanding hydrogen effects in metals and is measured by determining parameters such as the hydrogen diffusion coefficient and hydrogen solubility. Critically, the behaviour of surfaces and details of the hydrogen transport mechanism, such as trapping, have not been widely investigated particularly at the relatively low temperatures of interest in the oil and gas industries.

1.2 Objective of this Study

The overall aim of this work is to measure the effects of surface hold-up (due to a corrosion layer) and trapping on the permeation of hydrogen through low-alloy steels. The measurements will ultimately have relevance on the resistance of steels to various damaging processes involving hydrogen, most notably SCC and HIC.

In this work, a heavily modified version of the Devanathan cell (Devanathan and Stachurski, 1962) is presented using an electrochemical flux at one side of the membrane and a vacuum at the other side giving highly reproducible surface kinetics. The technique presented here uses an oscillatory probe which offers a new dimension to the measurement (probe frequency), leading to different characteristics for different types of kinetic process. The method of measuring permeation presented here involves hydrogen being introduced to the entry side of a thin metallic membrane by applying an oscillation as a sine wave about an appropriate value of electrical potential to a cell containing sodium hydroxide (NaOH). The corresponding electrical current, measured using a potentiostat, is taken as the incident flux of hydrogen to the surface. The exit side of the membrane is in contact with an ultra-high vacuum chamber where hydrogen partial pressure is measured using a mass spectrometer (residual gas analyser) against a known pump rate in order to obtain a measure of the exit flux.

1.3 Outline of the Thesis

The thesis is divided into eight chapters. In chapter one, the background to hydrogen damage to engineering alloys is presented, while chapter two offers a detailed literature review on hydrogen transport in metals covering experimental techniques as well as mathematical models.

In chapter three, the experimental rig used for the permeation experiments is described and a comparison between it and the Devanathan cell and other techniques is shown. Chapter four is devoted for the data analysis along with the newly developed analytical model for trap-limited and surface-limited permeation.

In chapter five, the calibration experiments on nickel are presented with both the results and analyses. Experiments on the low alloy steel samples studied in this work are described and their data analysed in chapter six.

Chapter seven contains the discussion and chapter eight is used for presenting the conclusions and future recommendations.

Chapter 2

Literature Review

2.1 Introduction

The processes leading to hydrogen damage involve the dissolution, transport and internal evolution of hydrogen in steels, a matter which has been the subject of some detailed study. The commonest way of assessing the interaction between hydrogen atoms and the metal lattice both on the surface and in the bulk, is to use hydrogen permeation experiments and a number of different techniques have evolved, the most widely used of which is the electrochemical permeation technique pioneered by (Devanathan and Stachurski, 1962). The examination of events taking place as hydrogen atoms transport through the metal is considered an important tool in understanding hydrogen effects in metals and is measured by determining parameters such as the hydrogen diffusion coefficient and hydrogen solubility and evaluating models for the permeation flux.

This review covers first the theory of hydrogen permeation which underlies any experiment. Next, modifications introduced to permeation theory to account for trapping are reviewed. Next, the range of experimental arrangements for permeation experiments are covered followed by a final section on the various parameters that have been measured for diffusion, solubility, trapping and surface hold-up in the materials of interest for this study, i.e. nickel and low alloy steel.

2.2 Theory of Permeation

The description of permeation of hydrogen through metals is often dealt with using a one-dimensional model of a metal slab, with hydrogen entering at one surface, diffusing through the bulk of the metal and exiting at the other surface (Addach et al., 2005, Turnbull, 1995, Bockris, 1973, Devanathan and Stachurski, 1962). These processes include the following stages starting from the entry side of the metal membrane: adsorption, dissociation and dissolution at the entry surface, diffusion (and, possibly, trapping and/or evolution) in the bulk of the metal, and recombination and desorption at the exit surface.

2.2.1 Surface Effects

Hydrogen is introduced to the metal as a result of its surface being exposed to a high chemical potential, which can be induced by simulating some types of corrosive environment (Turnbull et al., 1989b) or simply by raising the potential of an alkaline or acid solution (Warren, 1987).

If hydrogen ions are present at the surface, they may become adsorbed via the following reaction which occurs in alkaline solutions such as NaOH:

$$H_2O + e^- \rightarrow H_{ads} + OH^- \tag{2-1}$$

and, subject to the thermodynamic and kinetic parameters at the surface, may simply evolve as hydrogen gas (Devanathan and Stachurski, 1964):

$$2H_{ads} \rightarrow H_2 \tag{2-2}$$

The second of these is known as the Tafel recombination reaction which, if inhibited by a recombination poison which occurs in environments such as those containing sulphides, leads to the absorption reaction, (Bockris et al., 1965):

$$H_{ads} \rightarrow H_{abs} \tag{2-3}$$

Once absorbed, hydrogen atoms can readily diffuse through the metal which may lead to embrittlement and/or evolution within the material in a class of phenomena known as “hydrogen damage”. Many studies in the literature, (McBreen et al., 1966, Devanathan and Stachurski, 1964, Kim and Wilde, 1971, Iyer et al., 1989), have included developments of mathematical models to describe phenomena like the hydrogen absorption and evolution which occur on the surface of the metal and such phenomena could have some effect on permeation.

In one study (Iyer et al., 1989) the hydrogen evolution reaction was assumed to be a coupled discharge-recombination (Volmer-Tafel) where the charging current, i_c, is given as follows:

$$i_c = i_r + i_\infty \tag{2-4}$$

where i_r is the recombination current density and i_∞ is the steady state permeation current density (all current densities have units of A/cm^2). The charging and recombination current densities were given as follows:

$$i_c = Fk_1 C_H (1-\theta_H)\exp(-a\alpha\eta) \tag{2-5}$$

$$i_r = Fk_2\theta_H^2 \tag{2-6}$$

where C_H is the hydrogen ion concentration (mol/l), $a=F/RT$, F is Faraday constant (96484.6 C/mol), R is the universal gas constant (8.314 J/mol.K), T is the absolute temperature (K), α is the transfer coefficient, η is the hydrogen overpotential (V), k_1 is the discharge rate constant (cm/s), k_2 is the recombination rate constant (mol/cm^2.s) and θ_H is the hydrogen surface coverage (dimensionless).

The flux at the steady state and the corresponding current density are given as follows, (Devanathan and Stachurski, 1962, Devanathan and Stachurski, 1964):

$$J = \frac{DC_H^0}{L} \Rightarrow i_\infty = \frac{FDC_H^0}{L} \tag{2-7}$$

where C_H^0 is the concentration at the entry side of the membrane, D is the hydrogen diffusion coefficient (cm^2/s) and L is the thickness of this membrane.

Considering that the steady state permeation current is given by the following equation, (Kim and Wilde, 1971):

$$i_{\infty} = Fk_{abs}\theta_H - Fk_{des}C_H^0 \tag{2-8}$$

some arrangement leads to a relationship between i_{∞} and i_r as follows, (Iyer et al., 1989, Al-Faqeer and Pickering, 2002):

$$i_{\infty} = k\sqrt{\frac{F}{k_2}}\sqrt{i_r} \tag{2-9}$$

where k is referred to as the kinetic-diffusion constant (mol/cm^2.s) and is given as, (Elhamid et al., 2000):

$$\frac{1}{k} = \frac{1}{k_{abs}} + \frac{L}{D}\frac{k_{des}}{k_{abs}} \tag{2-10}$$

where k_{abs} is the absorption rate constant (mol/cm^2.s) and k_{des} is the desorption rate constant (cm/s).

Another equation can be derived from rearranging equation (2-5) and $i_{\infty} = Fk\theta_H$ which gives a relationship between the charging current density, i_c, and the steady state permeation current density, i_{∞}:

$$i_c \exp(a\alpha\eta) = i_0^{'}(1 - \frac{1}{Fk}i_{\infty}) \tag{2-11}$$

where

$$i_0^{'} = Fk_1C_H \tag{2-12}$$

In any electrochemical permeation system, k and $i_0^{'}$ can be found from equation (2-11) and then, using equation (2-9), k_2 can be calculated. Finally, equation (2-12) can be used to calculate k_1. The values of desorption and absorption constants can then be derived from equation (2-10), and the surface coverage θ_H can finally be found using $i_\infty = Fk\theta_H$.

Other models have been proposed that describe the effects of absorption and desorption on the hydrogen permeation in metals. One example is given by two equations which make it possible to define and evaluate an absorption parameter k_p (mol/cm^2.s) and a desorption parameter k (cm/s) in addition to finding the hydrogen diffusion coefficient D (cm^2/s), (Zhang and Zheng, 1998, Popov et al., 1994):

$$\frac{J}{J_\infty} = 1 + 2(2D + kL)\sum_{m=1}^{\infty} \frac{[k\cos(\lambda_m L) - D\lambda_m \sin(\lambda_m L)]e^{-D\lambda_m^2 t}}{[(D^2\lambda_m^2 + k^2)L + 2kD]} \tag{2-13}$$

$$J_\infty = \frac{k_p}{2 + \frac{kL}{D}} \tag{2-14}$$

where L is the thickness of the metal membrane (cm), J/J_∞ is the normalised flux, J_∞ is the steady state flux (mol/cm^2.s) and λ_m is obtained from:

$$\tan(\lambda_m L) = \frac{2kD\lambda_m}{D^2\lambda_m^2 - k^2} \tag{2-15}$$

Compounds of substances such as *P, As, Se, Sb, Te,* and *I,* in addition to *S* may promote the entry of hydrogen into metals (McCright, 1973).

Newman and Shreir (1969) showed that, when the foregoing elements are present in the form of hydrides H_2X (where X stands for any of the elements), they make better promoters of hydrogen entry into metals than HX^- and X^{--} and their pH values decrease in the sequence $H_2X \rightarrow HX^- \rightarrow X^{--}$ where HX^- and X^{--} are the products in the reactions $H_2X \rightarrow H^+ + HX^-$ and $HX^- \rightarrow H^+ + X^{--}$ (Newman and Shreir, 1969).

2.2.2 Diffusion-limited Permeation

On the assumption that there is no trapping in the metal, the diffusion of hydrogen atoms through a metal slab can be described by Fick's second law:

$$\frac{\partial C}{\partial t} = D\frac{\partial^2 C}{\partial x^2} \tag{2-16}$$

where C is the concentration, D is the diffusion coefficient, x is the distance from the input surface and t is time.

According to the Devanathan method (Devanathan and Stachurski, 1962), the initial and boundary conditions assumed are:

$$C = C_0;\ x = 0;\ t \geq 0 \tag{2-17}$$

i.e. concentration is constant at the input surface, and:

$$C = 0;\ x = L;\ t \geq 0 \tag{2-18}$$

i.e. concentration is equal to zero at the exit surface, and

$$C = 0;\ 0 < x \leq L;\ t = 0 \tag{2-19}$$

i.e. the initial concentration is zero at all points, where L is the thickness of the membrane in the x direction.

Inherent in the above conditions is that the input surface is in equilibrium with the prevailing hydrogen potential and the output surface is in equilibrium with a negligible hydrogen potential. Such conditions inherently assume that the surface kinetic processes are far more rapid than the bulk one, i.e. diffusion.

Given this, the solution of the differential equation (2-16) corresponding to conditions (2-17) to (2-19) is given as follows (Crank, 1975):

$$\frac{C}{C_0} = 1 - \frac{x}{L} - \frac{2}{\pi}\sum_{1}^{\infty}\frac{1}{n}\sin\frac{n\pi x}{L}\exp(-Dn^2\pi^2 t/L^2) \tag{2-20}$$

By differentiating (2-20) with respect to *x* taking into account Fick's first law for the steady state condition:

$$J_\infty = \frac{DC_0}{L} \tag{2-21}$$

The flux can be obtained as follows:

$$\frac{J}{J_\infty} = 1 + 2\sum_{1}^{\infty}\cos\frac{n\pi x}{L}\exp(-Dn^2\pi^2 t/L^2) \tag{2-22}$$

In any permeation experiment, it is the flux which is measured and (Figure 2-1 shows schematically a classic hydrogen permeation curve which follows equation (2-22). This curve consists of three stages: a time lag, T_{Lag}, (variously defined as described later), a maximum constant level at steady state permeation, and a decline at the termination of the hydrogen charging process (Maroef et al., 2002). The rising transient in this curve follows equation (2-22) until the steady state status is obtained, while the decay part is given by the expression $[-2\sum_{1}^{\infty}\cos\frac{n\pi x}{L}\exp(-Dn^2\pi^2 t/L^2)]$. These curves have been simplified by many authors (e.g. (McBreen et al., 1966, Turnbull et al., 1989b, Devanathan and Stachurski, 1962)) and used to calculate the diffusion coefficient.

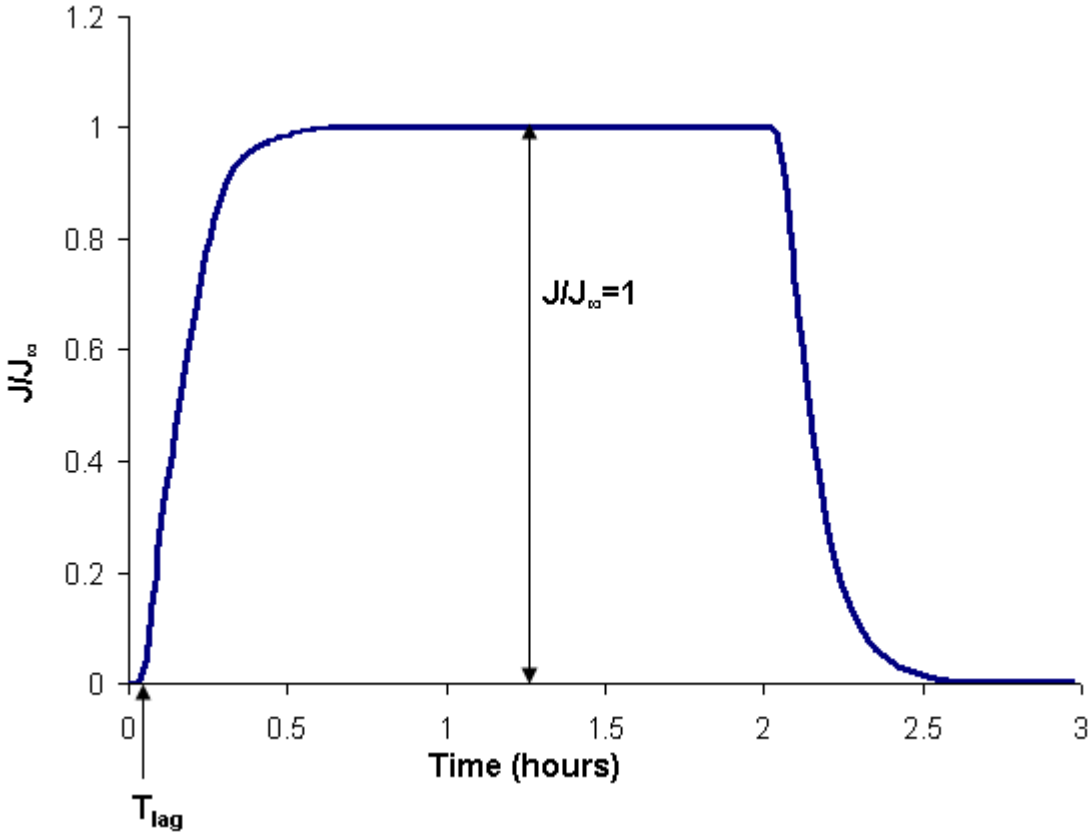

Figure 2-1: Schematic representation of hydrogen permeation curve through a metal membrane.

For example, (Kiuchi and McLellan, 1983, McBreen et al., 1966, Yen and Shih, 1988) have derived simplified forms of equation (2-22) to describe the permeation transient required to evaluate the hydrogen diffusion coefficient D for the metal.

Devanathan and Stachurski (1962) showed that the diffusion coefficient could be calculated by either the time to breakthrough method or the time lag:

- Time-to-breakthrough: $D = \frac{L^2}{15.3 t_b}$ where t_b is found by extrapolating the linear portion of the initial rising flux transient to $J = 0$.

- Time-lag (Crank, 1975): $D = \frac{L^2}{6 T_{lag}}$, where T_{lag} (corresponds to the point of the permeation curve at which $J = 0.63\ J_\infty$.

McBreen *et al* (1966) used both Laplace and Fourier transforms to solve Fick's second law as follows (only the first term of the summation is presented here):

using the Laplace transform:

$$\frac{J_t}{J_\infty} = \frac{2}{\sqrt{\pi\tau}} \exp(-\frac{1}{4\tau}) \tag{2-23}$$

Using the Fourier transform:

$$\frac{J_t}{J_\infty} = 1 - 2\exp(-\frac{\pi^2}{\tau}) \tag{2-24}$$

where J_t is the flux at any time t, $\tau = \frac{Dt}{L^2}$ is the normalized time, and D, J_∞ and L are as defined earlier.

Another mathematical approximation was derived by Yen and Shih (1988) leading to the equation:

$$\frac{J_t}{J_\infty} = 1 - \exp(-6\tau) \tag{2-25}$$

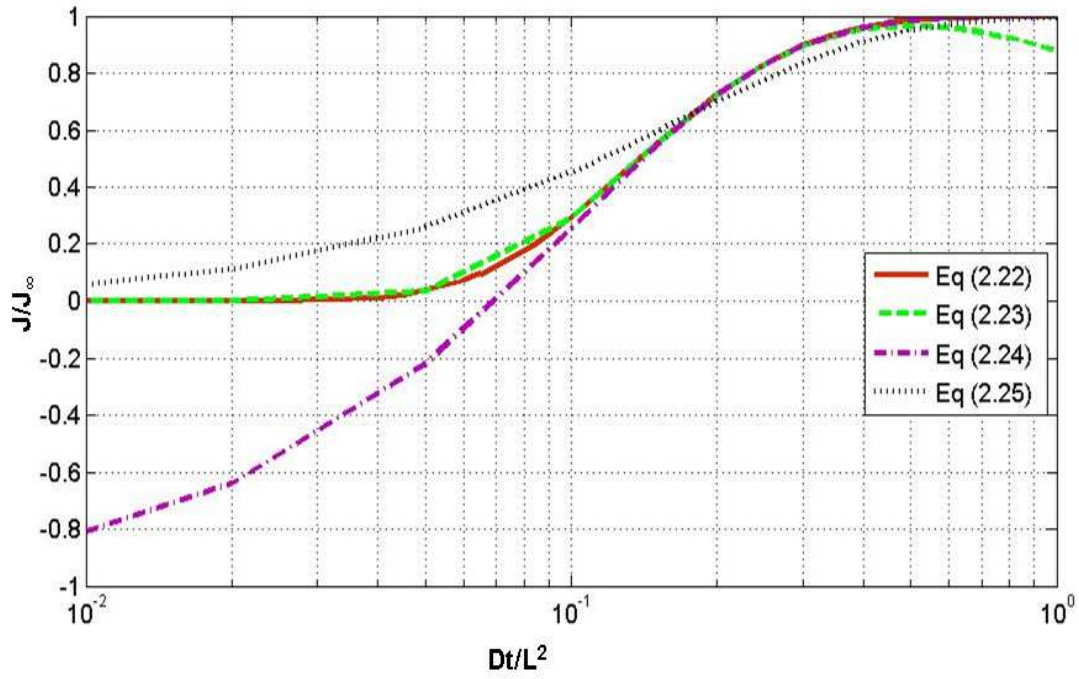

Figure 2-2: Normalised flux vs. normalised time for various approximations to the permeation transient (equations (2-22) to (2-25)).

In Figure 2-2, the curves representing the full solution (2-22) and equations (2-23) to (2-25) are plotted. It may be noted that the Fourier solution, equation (2-24), gives incompatible results for $\tau < 0.1$ as the normalised flux is less than zero. Also, the Laplace solution, equation (2-23), is incompatible as the flux decays when $\tau > 0.5$. Equation (2-25) seems to be a better approximation over the range than equations (2-23) and (2-24) as it gives compatible values for the normalized flux for all values of normalised time in a simpler and more consistent way. Most of the models are convergent between τ = 0.1 and 0.2, except equation (2-25), reflecting their development as time-lag analysis approximations.

2.2.3 Surface-limited Permeation

A model describing hydrogen diffusion through a metal/oxide system was developed by Pyun and Oriani (1989) which took into consideration hydrogen transport through the metal and a passivating layer (oxide). A specific rate parameter, k_s, was introduced which embodies a proton jump through the passive film and this parameter was assumed to be related to the applied anodic potential, (Pyun and Oriani, 1989). A summary of the analysis is given below.

As before, Fick's second law gives the hydrogen concentration C as:

$$\frac{\partial C}{\partial t} = D\frac{\partial^2 C}{\partial x^2} \tag{2-26}$$

and the initial and boundary conditions are:

$$t = 0,\ C = 0 \text{ for all } x,$$

$$t \geq 0,\ J = -D(\frac{\partial C}{\partial x})_{x=0} = q\,,$$

$$\text{and } t \geq 0,\ J = -D(\frac{\partial C}{\partial x})_{x=L} = k_s C_L = J(t)$$

where x is the distance from the entry side, q is the constant hydrogen flux, k_s is the specific rate parameter (cm/s), L is the thickness of the metal membrane, C_L is the concentration at $x = L$ and $J(t)$ is the hydrogen flux at the exit side.

The solution for equation (2-26) is found by assuming two independent functions, v and w where $C = v + w$, assigning the boundary conditions for each of them and finally finding $C(x,t)$ by the sum of solutions v (x,t) and w (x,t). The functions v and w are chosen such that v represents the part of the concentration driving the net output and w the part driving the net input.

Thus, the boundary conditions for v are:

$$-D(\frac{\partial v}{\partial x})_{x=0} = 0 \text{ and } -D(\frac{\partial v}{\partial x})_{x=L} = J(t)$$

and the boundary conditions for w are:

$$-D(\frac{\partial w}{\partial x})_{x=0} = q \text{ and } -D(\frac{\partial w}{\partial x})_{x=L} = 0$$

and the final solution is given as:

$$C(L,t) = -\frac{1}{\sqrt{\pi D}}\int_0^t \{\frac{J(\tau)}{\sqrt{t-\tau}}[\sum_{n=0}^{\infty}\exp(-\frac{(2nL)^2}{4D(t-\tau)}) + \sum_{n=0}^{\infty}\exp(-\frac{(2n+2)^2 L^2}{4D(t-\tau)})]\}d\tau +$$

$$+ 4q\sqrt{t/D}\sum_{n=0}^{\infty} ierfc\frac{(2n+1)L}{2\sqrt{Dt}} \qquad (2\text{-}27)$$

where $J(\tau)$ in (atom H / cm^2.s) is the measured flux at any value of the time variable τ.

Measured permeation transients $J(\tau)$, a measured hydrogen diffusion coefficient, a known value of q (which is the steady-state flux) and L enable the calculation of the concentration C at any given time t. From this, k_s can be determined by:

$$k_s = \frac{J(t_i)}{C(L,t_i)} \qquad (2\text{-}28)$$

2.2.4 Trapping-limited Permeation

It is well known now that hydrogen transport through metals is not merely controlled by diffusion between interstitial lattice sites, but also by trapping of hydrogen atoms at microstructural sites such as grain boundaries, dislocations, carbides, inclusions and precipitate particles (Kiuchi and McLellan, 1983, Turnbull, 1995).

Trapping decreases the rate at which hydrogen atoms migrate since those atoms have a certain likelihood of jumping into trap sites and staying there for a longer time than in the normal diffusion sites (Turnbull et al., 1989a). Traps are usually classified into reversible and irreversible traps according to the binding energy of the hydrogen atom to the trapping site.

A reversible trap is one that captures hydrogen atoms and releases them at a certain rate; in contrast, an atom in an irreversible trap has a very low probability of acquiring enough thermal energy to overcome the energy barrier so, after being captured, remains

there until a further treatment of the metal has been made (Hirth, 1980, McNabb and Foster, 1963), such as heating.

The formulation of McNabb and Foster (1963) was originally developed for reversible traps, although it has been adapted in other work (Turnbull et al., 1989a, Turnbull and Carroll, 1990, Iino, 1982, Leblond and Dubois, 1983a) to deal with irreversible traps in steel.

The model is represented by the following equation:

$$\frac{\partial C_L}{\partial t} = D_L \frac{\partial^2 C_L}{\partial x^2} - N \frac{\partial \phi}{\partial t} \tag{2-29}$$

where $\frac{\partial \phi}{\partial t}$ is the rate of trapping and ϕ is the fraction of occupied traps; and N is the total number of lattice and trap sites.

The rate constants for hydrogen atom capture, k, and release, p in the presence of a reversible trap are incorporated in the following:

$$\frac{\partial \phi}{\partial t} = kC_L(1-\phi) - p\phi \tag{2-30}$$

A simple model was developed by Oriani (1970) assuming that the trapping sites are very much fewer than the normal lattice sites. Here, Fick's first law is written in the form:

$$J = -D_L \frac{dC_L}{dx} \tag{2-31}$$

where D_L is the hydrogen diffusion coefficient in a defect (trap) free BCC iron matrix; C_L is the hydrogen concentration in the lattice sites.

Experiments can be described by the relationship between the observed flux and the total concentration as follows:

$$J = -D_a \frac{dC}{dx} \tag{2-32}$$

where C is the total hydrogen concentration and D_a is the apparent diffusion coefficient.

Under the assumption of rapid equilibrium between normal diffusion sites and those for trapping and taking C as the sum of C_L and C_T^0, the following equation was derived:

$$D_a = D_L \frac{dC_L}{dC} = \frac{D_L}{1 + C_T^0 \exp(E_B / RT)} \tag{2-33}$$

where E_B is the binding energy for the traps and C_T^0 is the concentration of trap sites in the matrix. When the fractional occupancy of the trap sites is low, the effective diffusion coefficient is given by (Oriani, 1970):

$$D_{eff} = \frac{D_L}{1 + K_a N_x / N_L} \tag{2-34}$$

where K_a is the ratio of activity of the hydrogen in trapping sites to activity in normal sites; and N_x and N_L are the number of traps and normal sites per unit volume respectively.

A number of other mathematical models have been developed to describe hydrogen diffusion and trapping (e.g. (Turnbull and Carroll, 1990, Leblond and Dubois, 1983b)) although these generally contain too many unknown parameters for practical application (Turnbull et al., 1989a). Even then, a few important assumptions have been made. First, there are no specifically attractive trap sites that may capture more hydrogen atoms than other types of sites. Secondly, the metal contains only three types of sites (type 1: diffusion sites, type 2: reversible traps, type 3: irreversible traps). Another assumption is that all trap sites are encircled by diffusion sites.

The model of Leblond and Dubois (1983a) can be simplified, (Turnbull et al., 1989a) to:

$$\frac{\partial n_1}{\partial t} = D_1 \frac{\partial^2 n_1}{\partial x^2} + p_2 \frac{n_2}{\tau_2} - p_2 \frac{n_1}{\tau_1}\left[1 - \frac{n_2}{n_2^S}\right] - p_3 \frac{n_1}{\tau_1}\left[1 - \frac{n_3}{n_3^S}\right] \tag{2-35}$$

$$\frac{\partial n_2}{\partial t} = \frac{n_1}{\tau_1}\left[1 - \frac{n_2}{n_2^S}\right] - \frac{n_2}{\tau_2} \tag{2-36}$$

$$\frac{\partial n_3}{\partial t} = \frac{n_1}{\tau_1}\left[1 - \frac{n_3}{n_3^S}\right] \tag{2-37}$$

where n_1 is the concentration of hydrogen atoms in diffusion sites; n_2 and n_3 are the concentrations of hydrogen atoms in sites of type 2 and 3 respectively, i.e. the number of hydrogen atoms in those sites per unit volume of metal; p_2 and p_3 are the volumetric proportions of sites of types 2 and 3 respectively; τ_1, τ_2 and τ_3 are the average times of transfer from a site of type 1, 2 and 3 to another site; and n_3^S is the saturation concentration of hydrogen atoms in sites of type 3. As can be seen, even this simplified model contains six new parameters governing the bulk process over and above the diffusion coefficient.

Amongst the developments of the McNabb and Foster model (1963) is one due to Turnbull *et al.* (Ferriss and Turnbull, 1988, Turnbull et al., 1989b) who have proposed a model that represents hydrogen diffusion and trapping as follows:

$$\frac{\partial C}{\partial t} = D\frac{\partial^2 C}{\partial x^2} - N_r \frac{\partial \theta_r}{\partial t} - N_i \frac{\partial \theta_i}{\partial t} \tag{2-38}$$

$$\frac{\partial \theta_r}{\partial t} = k_r C(1 - \theta_r) - p\theta_r \tag{2-39}$$

$$\frac{\partial \theta_i}{\partial t} = k_i C(1 - \theta_i) \tag{2-40}$$

where C is the concentration of hydrogen atoms in interstitial lattice sites, D is the lattice diffusion coefficient of atomic hydrogen, N_r and N_i are the density of reversible and irreversible trap sites, θ_r and θ_i are their fractional occupancy, and k_r, p and k_i are respectively, the rate constants for trapping and release, the latter obviously only for reversible traps.

The two types of traps will influence the rate of hydrogen atom transport through the metal during a first permeation test (i.e. one in which no traps are occupied). As the irreversible trap occupancy increases with time, transport becomes faster as there are fewer vacancies left to trap the diffusing atoms. At steady-state, the irreversible trap sites are occupied completely. After that, removing the hydrogen atoms and running the permeation test again will make it possible to evaluate the role of irreversible trapping on the whole transport process (Turnbull, 1995).

The model developed by Turnbull *et al.* (Ferriss and Turnbull, 1988, Turnbull et al., 1989b) seems to be so far the most appropriate one of all mentioned above as it is less complicated regarding the number of unknown parameters and it covers all types of traps that might exist in the bulk of the metal. Furthermore, it is also valid when the concentration of hydrogen atoms on the entry side of the slab is high, e.g. when a strong acid is used to enhance permeation rates. This model along with the original model pioneered by McNabb and Foster (1963) are the ones modified and developed in this work as described in chapter four.

2.3 Permeation Techniques

The electrochemical method first developed by Devanathan and Stachurski (1962) and its adaptations (e.g. (Turnbull et al., 1989a) has been widely utilised to study hydrogen transport through metals because of the simple electrochemical equipment required although temperatures are limited by the boiling point of the electrolyte. The basic Devanathan electrochemical cell is illustrated schematically in Figure 2-3 while an adaptation to it, (Turnbull et al., 1989a), is shown in Figure 2-4.

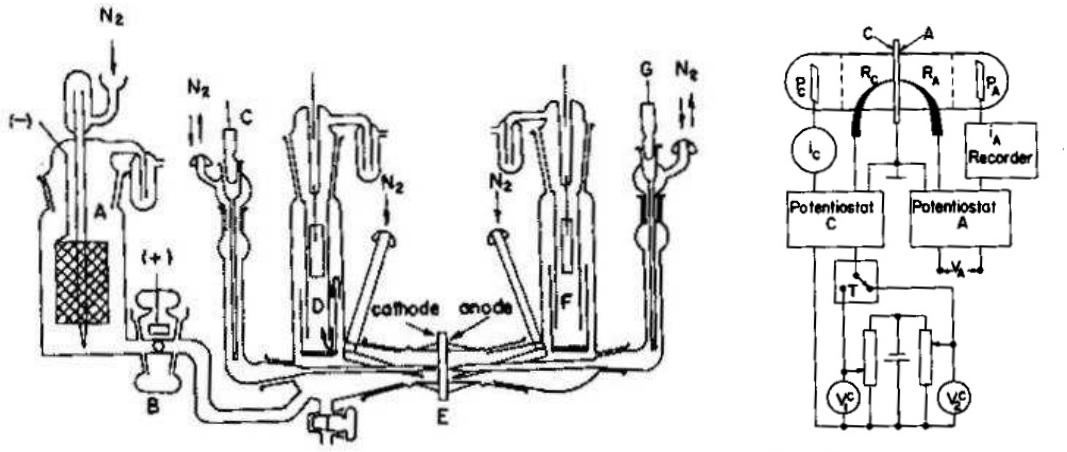

a b

Figure 2-3: a. Devanathan and Stachurski cell and b. Associated electrical circuit.
a) A-Cathodic compartment; B-Anodic compartment; C, G-Saturated calomel electrodes; D, F-Auxiliary electrodes; E-Sample.
b) C-Cathodically charged side of the sample; A-Anodically polarized side; PC, PA:Auxiliary electrodes; RC, RA: Reference electrodes; T: Electrical timer & coupled relay, (Devanathan and Stachurski, 1962).

Devanathan's cell comprised two identical compartments each of which was filled with 0.1N NaOH as an electrolyte. Each compartment was equipped with a platinum auxiliary electrode and a calomel reference electrode. The electrodes were connected to two independent potentiostats, one of which was used for cathodic charging at the input and the other for ionising hydrogen atoms that leave the membrane, hence measuring the permeation flux (Devanathan and Stachurski, 1962).

Thus, in this method (Devanathan and Stachurski, 1962), one surface of the membrane is cathodically polarised while the other is anodically polarised. The rate of hydrogen permeation will be directly measured by the current on the anodic side of the circuit.

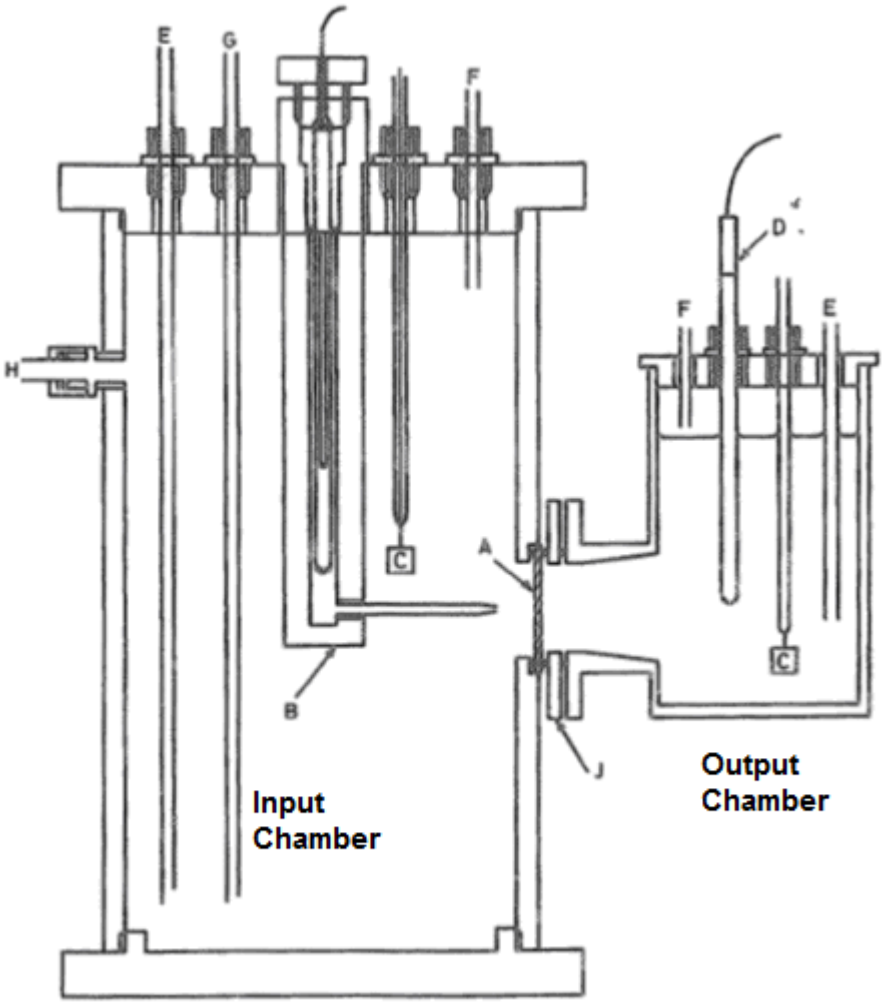

Figure 2-4: Hydrogen permeation set up. (A) Specimen (B) Double junction reference electrode in PTFE Luggin Capillary (C) Platinum electrodes (D) Double junction reference electrode (E) Gas inlet (F) Gas exhaust (G) Solution inlet (H) Solution outlet (J) Specimen clamp, (Turnbull et al., 1989b).

The adaptation to Devanathan's cell, (Turnbull et al., 1989b, Turnbull, 1995), introduced few changes to the original; the oxidation compartment for example was smaller than the charging cell and that allowed it to be attached to pipes or pressure vessels to give a wider range of output conditions. Also, contamination of reference electrodes solutions could be avoided by the use of double junction reference electrodes as shown in Figure 2-4.

Hydrogen electrochemical permeation not only depends on diffusion and trapping, but also on surface phenomena (Manolatos et al., 1995). In their work on iron and low

alloy steels, Manolatos et al (1995) pointed out that the boundary condition of hydrogen concentration at the entrance side of the metal membrane is not constant. In addition, they demonstrated that a passive layer formed on the exit side could act as a barrier to hydrogen evolution, so the hydrogen concentration on the exit side is not zero as assumed in other studies. They suggested that the exit surface concentration increases with time, decreasing the concentration gradient slowly as shown in Figure 2-5 and the permeation flux decreases similarly.

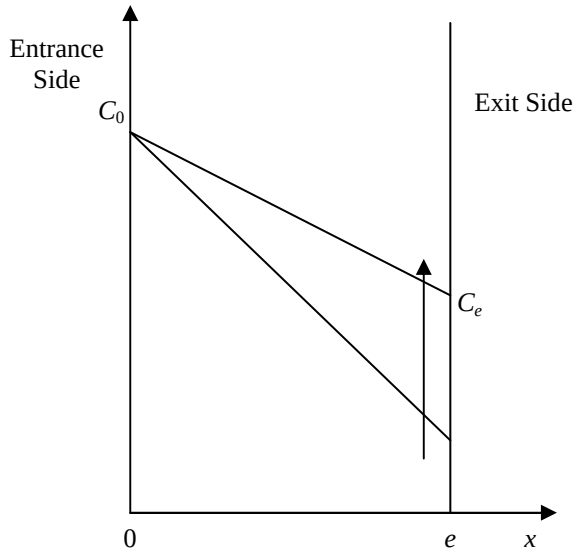

Figure 2-5: Schematic evolution of hydrogen concentration profile during permeation.

Palladium coatings have been used by many authors (Owczarek and Zakroczymski, 2001, Pyun and Oriani, 1989, Ningshen et al., 2001) to minimise surface hold-up by any oxide layers on the surface of the sample. Palladium has higher diffusivity of hydrogen than such oxide layers but coatings on charging surfaces influence the hydrogen concentration under the surface and that eventually will affect the permeation characteristics, (Turnbull, 1995).

As it is difficult to determine the input hydrogen chemical potential, it being dependent on the nature of the electrolyte used (acid or basic) and the potential, a gas phase charging method has been used (Johnson and Hill, 1960) to give control of the hydrogen fugacity at the entry site but this method could not be utilised at low temperatures due to surface impedance problems (Maroef et al., 2002).

Other techniques than electrochemical permeation have also been used to measure the hydrogen diffusion and permeation parameters through metals. One of those is the gas

phase permeation used by Perng and Altstetter (Perng and Altstetter, 1986, Perng and Altstetter, 1988) in which hydrogen was introduced to an austenitic steel membrane situated between two ultrahigh vacuum chambers. The hydrogen flux passing through the sample was measured and compared with the input hydrogen pressure, and then the permeability and effective diffusivity and solubility constants were calculated using the data obtained from transient and steady-state fluxes. This technique has the advantage of being able to carry out permeation experiments at elevated temperatures and does not involve any possibility of chemical contamination (such as from reference electrodes) that might affect the permeation data.

Another technique worthy of mention is the electrochemical impedance spectroscopy (EIS) used by Bruzzoni et al. (Bruzzoni et al., 1999) to study hydrogen permeation in ferritic iron. The experimental rig used for that study, illustrated in Figure 2-6, consists of a hydrogen gas charging compartment at the bottom side of the membrane and a detection cell on top of it. While non-linear differential equations are usually used to describe the relationship between variables such as current, potential and flux, which represent the electrochemical systems, the electrochemical impedance spectroscopy technique allows the transformation of these non-linear equations into linear ones to be solved analytically by applying a perturbation to any of the variables mentioned above (Bruzzoni et al., 1999) and using a transfer function in rather a similar way to the approach in the current work.

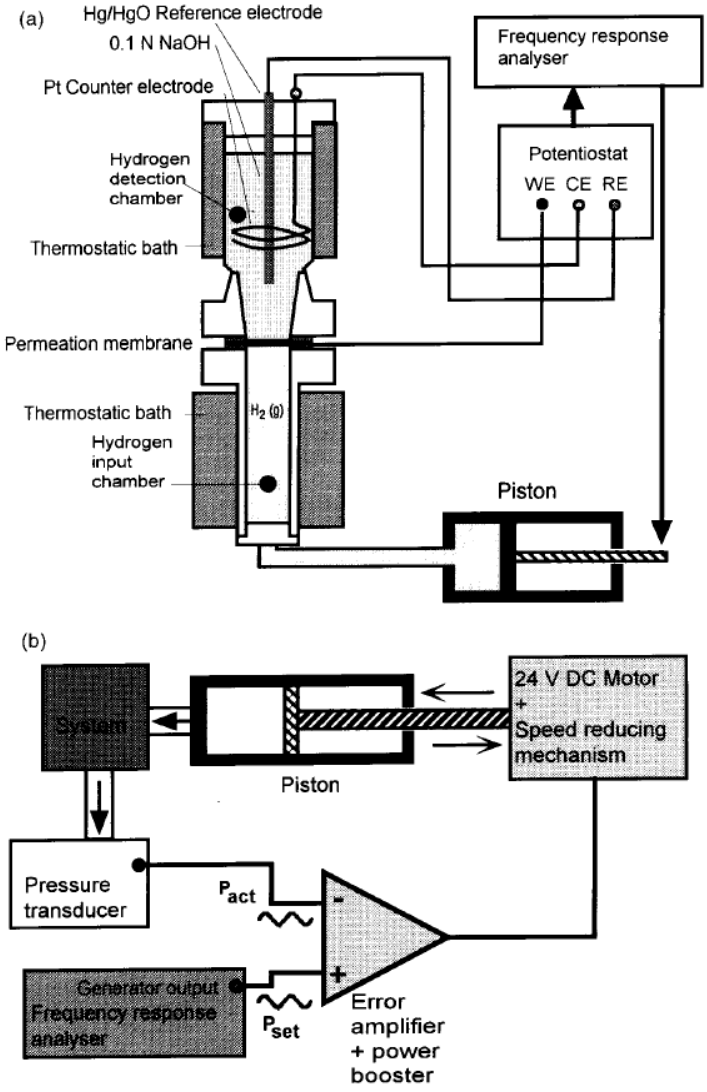

Figure 2-6: (a) Schematic experimental setup. (b) Feedback loop for pressure modulations (Bruzzoni et al., 1999).

The technique of Bruzzoni et al involves controlling the surface dynamics at the input side of the metal membrane where, for example, if a sinusoidal perturbation is applied to the hydrogen concentration, a corresponding perturbation of hydrogen flux will emerge at the output. Fitting the transfer function to experimental data resulted in obtaining hydrogen diffusion coefficient values consistent with those in the literature measured using other techniques. Many authors had already used a similar approach to study hydrogen transport in metals (Boes and Zuchner, 1976, Nagano, 1982, Pyun and Oriani, 1989).

In order to separate the surface effects from bulk ones on the hydrogen permeation through metals, Cummings et al. (Cummings et al., 1984) demonstrated that hydrogen diffusivity and solubility in metals can be assessed by measuring the amplitude and phase lag of pressure modulations through a sheet of metal situated between two vacuum chambers. They developed a generalised approach using a linear approximation for small perturbations and broke down the solution into a number of different components for the description of the modulated hydrogen flow. For example, equation (2-41) shows the relationship for the phase lag ϕ between the input and output pressures, while equation (2-42) gives the relationship for the amplitude ratio Λ between those pressures.

$$\tan\phi = \frac{\tan\zeta - \tanh\zeta}{\tan\zeta + \tanh\zeta} \tag{2-41}$$

$$\Lambda = \frac{DK_{sm}ART}{\sqrt{p_s}Sl}\frac{\zeta}{\sqrt{\cosh 2\zeta - \cos 2\zeta}} \tag{2-42}$$

where $\zeta = l\sqrt{\frac{\omega}{2D}}$, ω is the angular frequency at which the input pressure is modulated, l is the thickness of the metal sheet, A is the cross-section area of this sheet, R is the universal gas constant, T is the absolute temperature, p_s is the steady state input pressure, and S is the pumping speed of the pump used to evacuate the output chamber.

Thus, the phase lag can be used to obtain the diffusion coefficient and the amplitude ratio can be used to obtain the solubility coefficient, also providing a check on internal consistency of the diffusion coefficient. The advantage of the technique is that its time dependence allows signal averaging whereas the use of frequency as an experimental variable allows separation of different phenomena.

2.4 Published Hydrogen Permeation Data

This section reviews data on surface and bulk processes relevant to the work in question. As well as diffusion and solubility coefficients other data, such as trapping and surface kinetic parameters are reviewed, along with the methods used to determine them.

2.4.1 In Nickel

The diffusion of hydrogen in nickel has been investigated substantially and much of the data in the literature, including the diffusion coefficient, permeability and/or solubility, is consistent mainly at temperatures above 100°C while there is some scatter below that temperature (Volkl and Alefeld, 1978).

In their wide review of hydrogen diffusion in metals, Volkl and Alefeld summarised the diffusion coefficient of hydrogen in nickel in the following equations (Volkl and Alefeld, 1978):

$$D = 6.9\times10^{-7}\exp(-\frac{40510}{RT}) \quad (\mathrm{m^2/s}) \quad T \geq 627\mathrm{K} \tag{2-43}$$

$$D = 4.8\times10^{-7}\exp(-\frac{39340}{RT}) \quad (\mathrm{m^2/s}) \quad T \leq 627\mathrm{K} \tag{2-44}$$

where R is the universal gas constant (R = 8.3145 J/K.mol) and T is the absolute temperature (K).

Another well known review of hydrogen permeation data was undertaken by (Robertson, 1973) in which the diffusion coefficient for hydrogen in 99.98% nickel at temperatures between 273K and 1669K is given as:

$$D = 6.44\pm0.35\times10^{-7}\exp(-\frac{40200\pm300}{RT}) \ (\mathrm{m^2/s}) \tag{2-45}$$

In the same work, (Robertson, 1973), the permeability, P, was given as a function of temperature as follows:

$$P = 32.2\pm0.1\times10^{-7}\exp(-\frac{54800\pm200}{RT}) \ (\mathrm{mol\ H_2/m.s.mbar^{0.5}}) \tag{2-46}$$

Knowing the diffusivity and permeability, solubility can be derived from the equation:

$$P = KD \tag{2-47}$$

where K (mol $H_2/m^3.mbar^{0.5}$) is the solubility coefficient (sometimes referred to as Sievert's constant).

Santos and Miranda (1998) carried out permeation experiments on pure nickel using different cathodic potentials and had the following results for diffusivity and solubility at 313K, Table 2-1 where the solubility S is related to the solubility coefficient K by Sievert's law $S = K\sqrt{P_{H_2}}$, where P_{H_2} is the hydrogen partial pressure.

Reference	***E* (mV vs. SCE)**	***D* (m^2/s)**	***S* (mol H_2/ m^3)**
(Santos and Miranda, 1998)	-1650	4.4×10^{-14}	113
(Santos and Miranda, 1998)	-1350	$3.3\pm0.01\times10^{-14}$	87±8
(Santos and Miranda, 1998)	-2000	$7.3\pm0.2\times10^{-14}$	748±12

Table 2-1: Variations of the diffusion coefficient and solubility in nickel with cathodic hydrogen generation potential at 313K.

More data about hydrogen permeation is included in the following table, Table 2-2. These data are considered further in chapter seven in the light of experimental results from the current work.

Reference	***D* (m^2/s)**	***P* (mol H_2/m.s.$mbar^{0.5}$)**	**Conditions**
(Cummings et al., 1984)	$6.12 \pm 0.12 \times 10^{-7} \exp(-\frac{39800 \pm 200}{RT})$	$35.1 \pm 0.15 \times 10^{-7} \exp(-\frac{51900 \pm 300}{RT})$	600K < *T* < 1000K
(Altunoglu and Braithwaite, 1995)	$7.12 \pm 0.12 \times 10^{-7} \exp(-\frac{40640}{RT})$	$33.5 \times 10^{-7} \exp(-\frac{54250}{RT})$	373K < *T* < 623K
(Yamakawa and Fujita, 1977)	$19 \pm 1.1 \times 10^{-7} \exp(-\frac{37190 \pm 130}{RT})$	-	220K < *T* < 330K
(Ebisuzaki et al., 1967)	$5.22 \pm 0.18 \times 10^{-7} \exp(-\frac{40020 \pm 160}{RT})$	-	473K < *T* < 693K

Table 2-2: Hydrogen permeation data in nickel.

2.4.2 In Iron, Low Alloy Steels, En24 (approximately equivalent to AISI 4340)

Hydrogen permeation through iron and iron-based alloys has been studied by a number of authors but with a major degree of inconsistency mostly attributed to uncontrolled surface conditions (Kiuchi and McLellan, 1983) or trapping of hydrogen atoms at impurities, precipitates, grain boundaries, and other discontinuities, (Volkl and Alefeld, 1978).

Kiuchi and McLellan (1983) have assessed a considerable amount of hydrogen diffusivity data (62 sets of data) for BCC ferrous alloys and found a large variation. They divided the data into two ranges of temperature and recommended best fit lines for the diffusion coefficient as:

$$D = 7.23\times10^{-8}\exp(-\frac{5690}{RT}) \quad (\mathrm{m^2/s}) \qquad 233 \leq T \leq 353\ \mathrm{K} \tag{2-48}$$

and

$$D = (1-2.52)\times10^{-7}\exp(-\frac{6700-7120}{RT}) \quad (\mathrm{m^2/s}) \quad 323 \leq T \leq 823\ \mathrm{K} \tag{2-49}$$

Equations (2-48) and (2-49) are plotted on Figure 2-7 along with a selection of the relationships reported by Kiuchi and McLellan. As can be seen the degree of disagreement between 323 and 373 K is significantly greater than at higher temperatures. Since then, a number of other studies have measured permeation in iron and Table 2-3 gives a selection of these (where D is the diffusion coefficient and S is the hydrogen solubility).

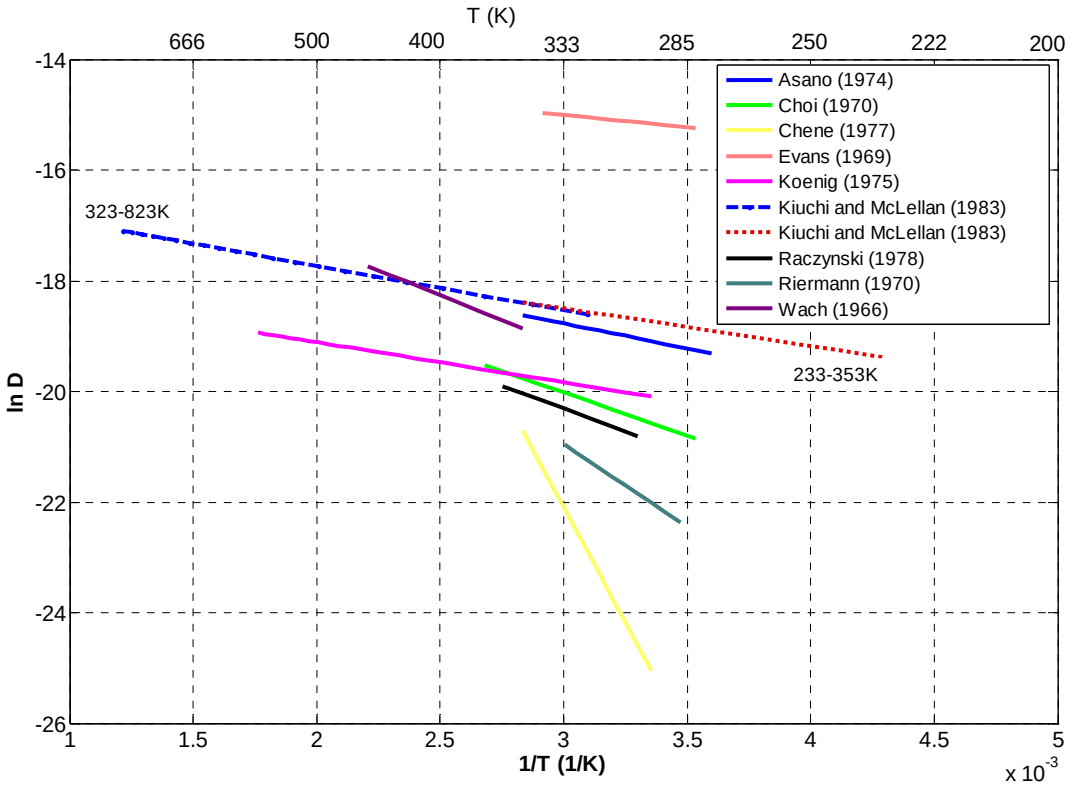

Figure 2-7: Kiuchi and McLellan's representation of hydrogen diffusivity data along with a selection of these data.

Reference	***D* (m^2/s)**	***S* (mol H_2/m^3)**
(Pyun and Oriani, 1989)	$(3.24\pm0.45)\times10^{-11}$, at 298K	0.918, at 298K
(Addach et al., 2005)	5.8×10^{-10}, at 298K	0.15, at 298K
(Addach et al., 2005)	9.3×10^{-10}, at 318K	0.35, at 318K
(Warren, 1987)	1.6×10^{-9}, at 298K	-
(Warren, 1987)	1.38×10^{-8}, at 673K	2.46, at 673K

Table 2-3: Hydrogen diffusion coefficient in BCC Iron.

(Garet et al., 1998) compared the diffusion coefficient values obtained from rising and decay transients for three low alloy steels from the permeation experiments using two different charging conditions as described in Table 2-4. 4140 steel samples were of two different sulphur contents, S 4140 being the one with the highest sulphur content of (0.087 wt%); the other one, Ca 4140, contained (0.0017 wt%) calcium and (0.01 wt%) sulphur.

Steel	**0.1M NaOH at 1105 mV/NHE**		**1N H_2SO_4 at 405 mV/NHE**	
	Rising transient	Decay transient	Rising transient	Decay transient
4120	5.3±0.9	1.06±0.7	36±5	3.6±0.08
Ca 4140	4.6±0.3	1.6±0.3	32.7	1.1
S 4140	1.5±0.1	0.12±0.007	4.1	0.18

Table 2-4: Diffusion coefficient D ($\times 10^{-11}$ m^2/s) at 298±0.1 K calculated using the time lag method with two charging conditions.

Clearly, not only did the alloy have an effect on diffusion coefficient but also, too, did the time and the surface conditions. Garet et al attributed these differences to the influence of sulphur content where the specimen with the highest sulphur amount had a smaller diffusion coefficient.

Some trapping parameters were calculated in a study on other low alloy steels, (Griffiths et al., 1994); details of their findings are presented in Table 2-5. The trapping model they used was the one developed by Turnbull *et al.* (Ferriss and Turnbull, 1988, Turnbull et al., 1989b) which was detailed in chapter two.

Steel	N_r (sites/m^3)	ΔE (kJ/mol)	D (m^2/s)	C_0 (ppm, mass)
BS4360 50D	$(3.2\pm1)\times10^{23}$	-46.5±1.1	4×10^{-11}	8.7×10^{-4}
3.5% Ni-Cr-Mo-V	$(4.9\pm0.6)\times10^{24}$	-50.3±0.3	5.3×10^{-12}	1.6×10^{-3}
AISI 4340	$(2.1\pm0.5)\times10^{24}$	-49±0.5	1.1×10^{-11}	1×10^{-3}

Table 2-5: Trap density, N_r, trap site binding energy, ΔE, diffusion coefficient, D, and subsurface concentration C_0 for three low alloy steels, (Griffiths et al., 1994).

AISI 4340 low alloy steel at various heat treatment conditions has been the subject of a few studies (Devanathan and Stachurski, 1963, McBreen et al., 1966, Griffiths et al., 1994, Scully and Moran, 1988b, Popov et al., 1994). These are summarised in Table 2-7.

In addition, Scully and Moran (1988b) have measured some surface kinetic parameters during this study of hydrogen permeation in AISI 4340 for a number of charging conditions. Their results for steady-state flux (J) were plotted against various sample thicknesses (L) and were fitted with the already derived expression, (Devanathan and Stachurski, 1962):

$$\frac{1}{J} = \left(\frac{LK_{des}}{D\theta K_{abs}} + \frac{1}{K_{abs}\theta}\right) \tag{2-50}$$

where D is the diffusion coefficient, θ is the hydrogen surface coverage, K_{abs} is the absorption rate, and K_{des} is the desorption rate.

Table 2-6 compares some of the results from the above study, (Scully and Moran, 1988b), for an acid electrolyte that contained a hydrogen absorption promoter (higher θK_{abs}) and an alkaline electrolyte which exhibited lower absorption rates (lower θK_{abs}).

Parameter	Acid electrolyte	Alkaline electrolyte
K_{des} (cm/s)	1.24×10^{-7}	1.19×10^{-6}
θK_{abs} ($\mu A/cm^2$)	1.158	1.0217

Table 2-6: Surface kinetic parameters related to hydrogen permeation in AISI 4340 for different charging conditions at 298±2 K.

Reference	D (m^2/s)	S	Heat Treatment
(Nanis and Namboodhiri, 1973)	7.5×10^{-10} at 295 K	0.174 mol H_2/m^3 at 295K	Annealed
(Nanis and Namboodhiri, 1973)	0.238×10^{-10} at 295 K	4.18 mol H_2/m^3 at 295K	Quenched from 1075K; tempered at 622K for 2 hours
(Nanis and Namboodhiri, 1973)	0.217×10^{-10} at 295 K	7.36 mol H_2/m^3 at 295K	Quenched from 1144K; tempered at 504K for 2 hours
(Robinson and Hudson, 1990)	2.5×10^{-11} at 295 K	-	Quenched and tempered
(Scully and Moran, 1988a)	4.5×10^{-11} at 298±2 K	-	Tempered
(Griffiths et al., 1994)	1.1×10^{-11} at 295±0.3 K	1×10^{-3} ppm (mass)	Oil quenched and tempered
(Popov et al., 1994)	4.2×10^{-11} at 296±1 K	-	Bismuth layer electroplated
(Devanathan and Stachurski, 1963)	2×10^{-11} at 298±1 K	-	Tempered

(Scully and Moran, 1988b)	1×10^{-11} at 298±2 K	-	Tempered
(Lee and Lee, 1982)	-	0.5488 ppm at 298 K	Spheroidized carbide
(Lee and Lee, 1982)	-	0.4867 ppm at 298 K	Pearlitic
(Dull and Nobe, 1982)	4.95×10^{-11} at 295 K	0.26 ppm	Annealed at 813 K for 1 hour
(Dull and Nobe, 1982)	9.75×10^{-11} at 295 K	0.16 ppm	Annealed 1143 K for 1 hour
(Dull and Nobe, 1982)	4.7×10^{-11} at 295 K	0.2 ppm	Tempered 703 K for 2 hours
(Dull and Nobe, 1982)	8.85×10^{-11} at 295 K	0.12 ppm	Tempered 923 K for 2 hours

Table 2-7: Hydrogen permeation data for AISI 4340.

Chapter 3

Experimental Setup

3.1 The Experimental Rig

The experimental rig used for the permeation experiments consisted essentially of a metal membrane which lies between two main sections; an electrochemical cell and an ultra high vacuum (UHV) system as shown in Figure 3-1.

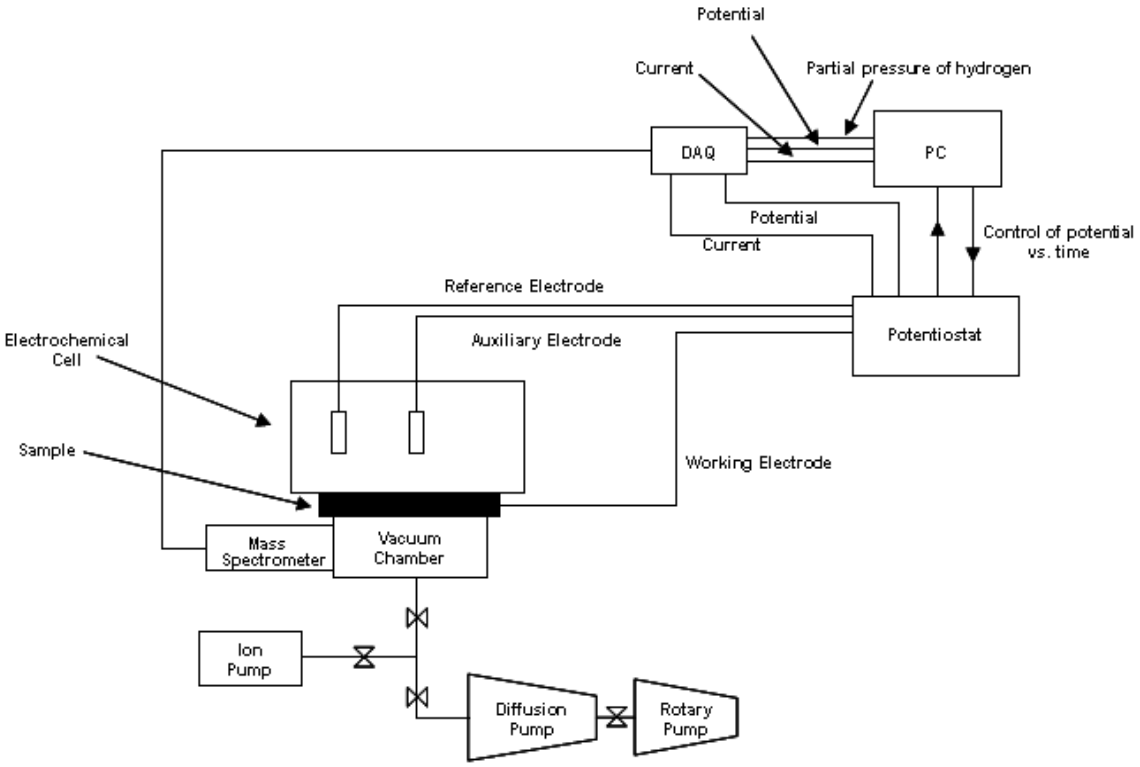

Figure 3-1: A schematic representation of the experimental rig used for the permeation experiments.

The electrochemical cell was made of Perspex and was designed to hold the chemical solution used for producing hydrogen (0.1N NaOH) as shown in Figure 3-2 and schematically in Figure 3-3. The sample was positioned between two flanges in the following order starting from the top flange: top flange, rubber gasket, sample, Viton UHV gasket, bottom flange. Both flanges were specially adapted UHV flanges with a flat sealing face so that a bakeable UHV seal could be made between the specimen and the UHV system. A U-bend was built into the sample assembly so that, if the sample were to be perforated through corrosion, any leaking solution would be trapped and the Viton valve could be closed to alleviate damage to the vacuum system.

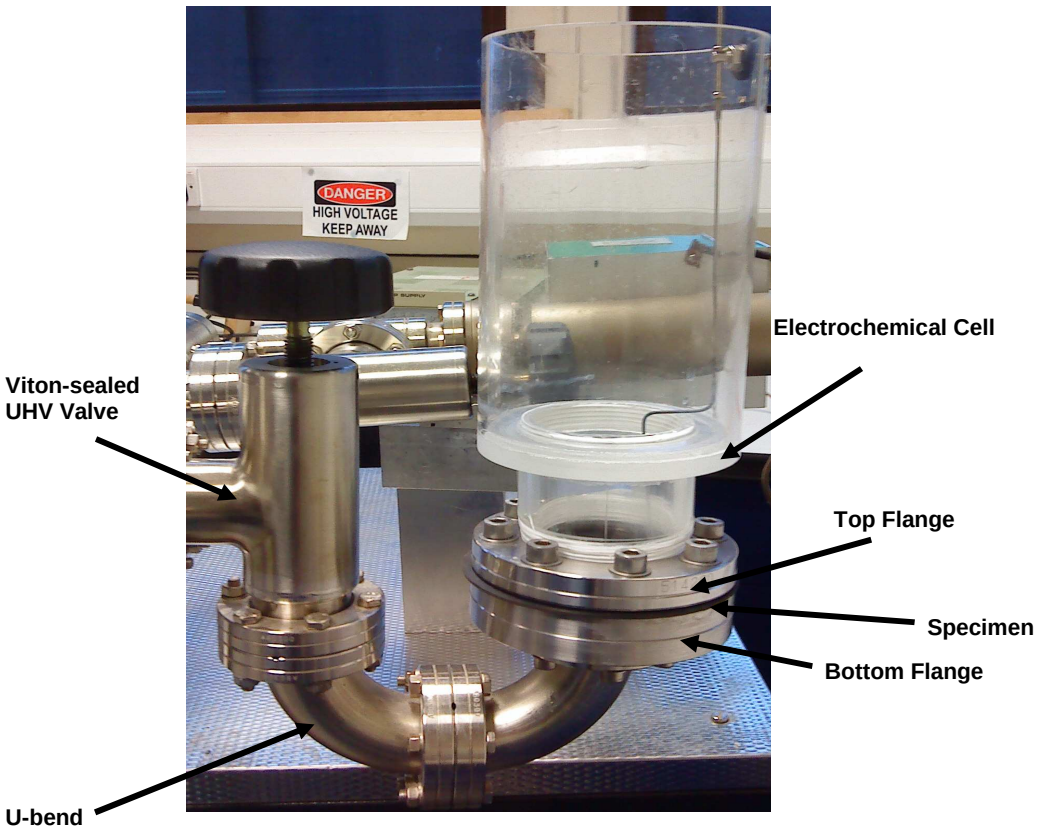

Figure 3-2: The Perspex cell attached to the top side of the membrane.

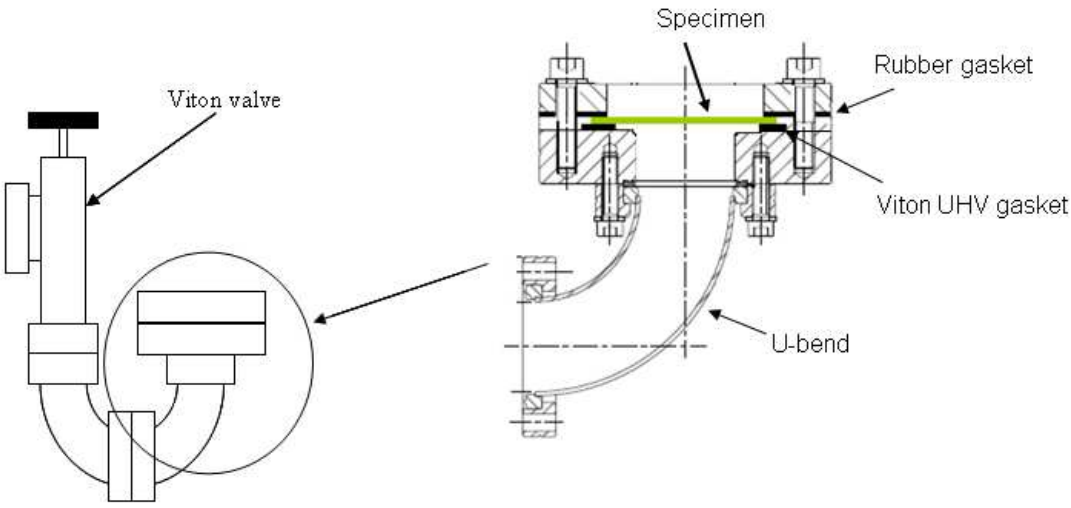

Figure 3-3: A schematic representation of how the membrane is positioned in the experimental rig.

The electrochemical cell contained a reference electrode, R.A., (which was a saturated calomel electrode SCE with a 3.5M KCl solution), an auxiliary platinum electrode,

A.E., and the sample acted as the working electrode, W.E., as illustrated in Figure 3-4. The three electrodes were connected to a computerized potentiostat (supplied by Sycopel Scientific Ltd) through which the working electrode potential was controlled using a simple LabView programme. The potential, current and partial pressure were measured using 3 channels of a data acquisition card, while a multi-meter and a voltmeter were connected to the potentiostat so that the potential and the current could be observed during the experiments.

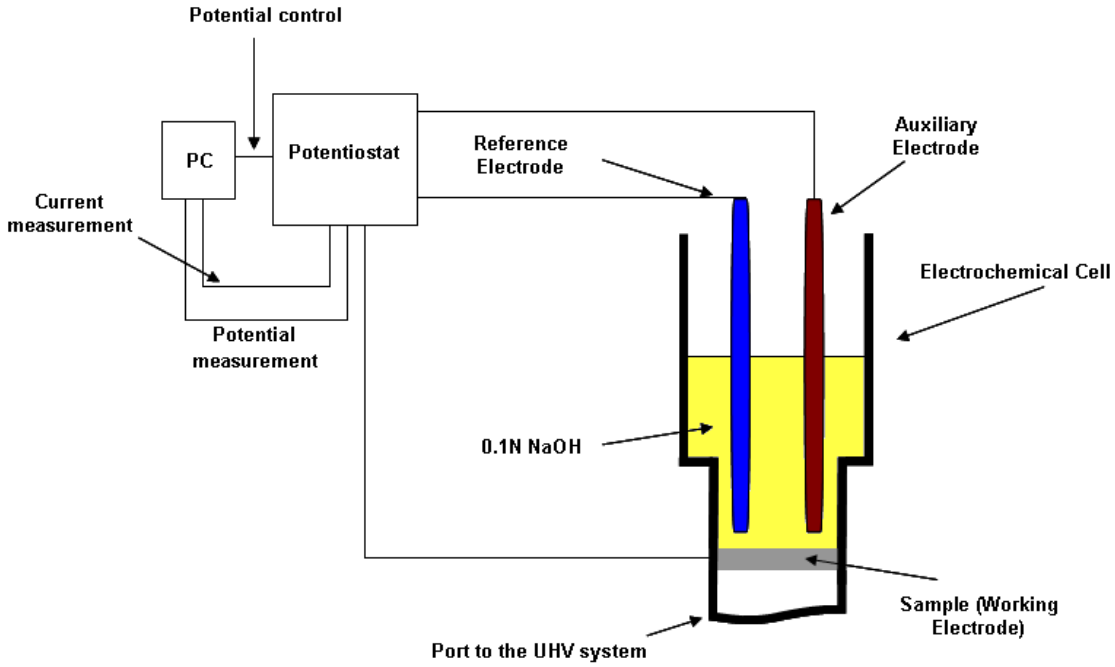

Figure 3-4: Illustration of the electrochemical cell with the electrodes (Reference Electrode, Auxiliary Electrode and Working Electrode) and the potentiostat.

The UHV system consisted of a vacuum chamber in contact with one surface of the metal sample, a quadrupole mass spectrometer (residual gas analyser, RGA) from Vacuum Generators (now known as Vacuum Scienta) for measuring the hydrogen partial pressure in the chamber, a diode-type ion pump (PID Series from MECA2000) with a dry air pumping speed of 25 l/s (hydrogen pumping speed is 200% of the dry air one i.e. 50 l/s) , an air-cooled vapour diffusion pump (EO4 Series, from SPEEDIVAC, Edwards High Vacuum Ltd.), an active inverted magnetron gauge (Penning gauge), and a two-stage rotary pump (Model ED50, from Edwards Vacuum Components). The Penning gauge was used during the conditioning of the vacuum system to check the pressure in the chamber before switching on the RGA, which cannot be used if the

pressure in the chamber exceeds 10^{-5} torr. Figure 3-5 shows the main parts of the UHV system, where the diffusion pump, cold trap and rotary pump were used to pump down the system and outgas after specimen changes.

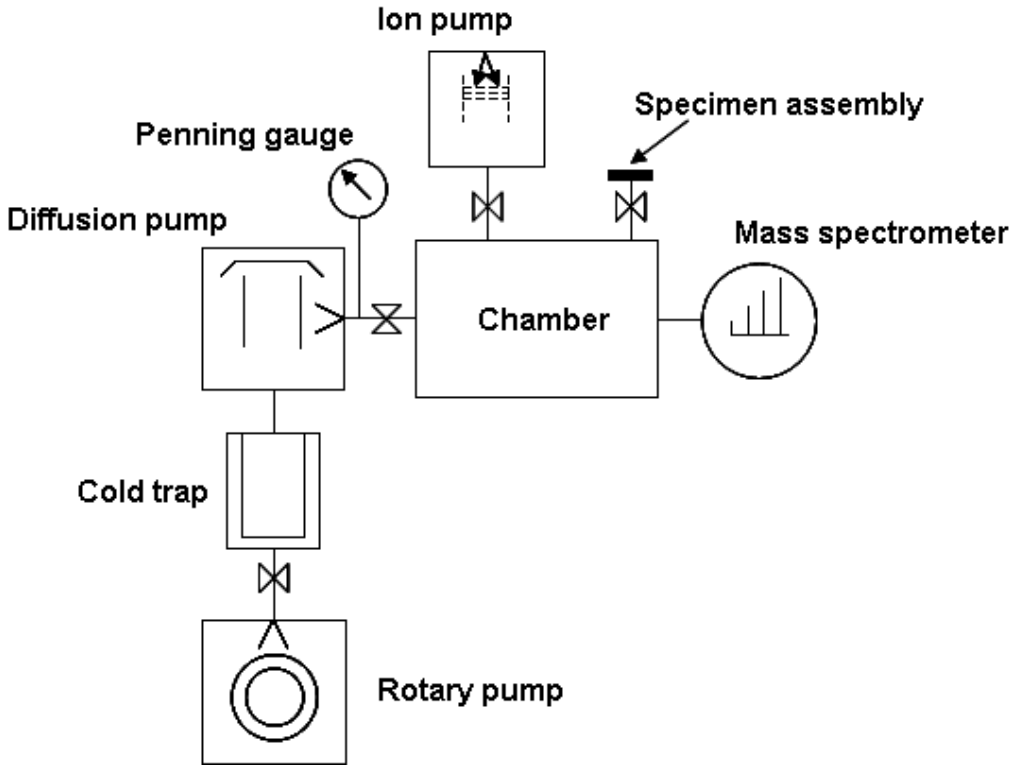

Figure 3-5: A diagram showing the UHV system.

3.2 Materials

Pure nickel (99%) was used for the validation experiments because of its well-known and reproducible permeation characteristics. The nickel specimen was supplied by Goodfellow Cambridge Limited as a disc of 83 mm diameter and 0.25 mm thickness. En24 (equivalent to BS 970 817M40 and approximately equivalent to AISI 4340) steel, whose major chemical constituents are shown in Table 3-1, was used for the main experiments. The steel was used in three heat-treatment conditions; the annealed condition (hardness 260±2 HV), the as-quenched condition (hardness 508±1 HV) and the quenched and tempered condition (hardness 413±2 HV). All steel specimens were in the form of discs 83mm in diameter with different thickness as described below and the effective area that was in contact with the chemical solution was 25.5 cm^2 in all cases.

The annealed specimen (as-received condition) was machined from disks of 1 mm thickness to the final thickness of 0.25 mm. The as-quenched specimen was prepared by heating up an as-received annealed specimen (0.5 mm thick) in a furnace to a temperature of 850°C, held for about 30 min then quenched immediately in oil. The quenched disk was then hand-ground in a specially-prepared jig to the final thickness of 0.35 mm. The tempered specimen was prepared by placing a quenched but unground specimen (prepared as above) into a preheated furnace (at 500°C) for about 1 hour then left to cool in air; the thickness was again reduced by hand-grinding to 0.65 mm.

C	Mn	Cr	Mo	Ni	Fe
0.38	0.69	0.95	0.26	1.58	Balance

Table 3-1: Chemical composition (wt %) of low alloy steel used for the permeation experiments (main alloying elements only).

Sodium hydroxide solution (0.1N NaOH) prepared from laboratory reagent grade NaOH supplied by Fisher Scientific, and distilled water was used as the electrochemical charging solution.

3.3 Vacuum Preparation

The sensitivity of the experiment relies heavily on a well-calibrated vacuum system where outgassing and leak rates are kept as low as possible. Much of this is assured by the measurement only of hydrogen partial pressure as leak rates and outgassing rates will be a very small fraction of those of the main constituents (water, nitrogen and oxygen), although every attempt was made to obtain low total pressure.

3.3.1 Pumping Rate Calculations

The vacuum chamber was continuously pumped by the ion pump to achieve an ultimate total pressure inside the chamber of which the hydrogen partial pressure is low enough to allow the detection of hydrogen produced and permeated through the metal membrane. The power supply attached to the ion pump was set at a pumping speed of 20 (l/s) for air so, for hydrogen, the pumping speed is 40 (l/s) because hydrogen pumping speed is 200% of the pumping speed of air (from the ion pump specifications).

The effective hydrogen pumping speed (by the ion pump) can be calculated from the following formula (Chambers et al., 1998):

$$S = \frac{S^* \times C}{S^* + C} \tag{3-1}$$

where S (l/s) is the effective speed, C (l/s) is the total conductance (which is a measure of the ease of flow in a vacuum system) of the components between the pump and the chamber, and S^* (l/s) is the given pumping speed of the pump. When components are in series, C, the overall conductance, is given by:

$$\frac{1}{C} = \frac{1}{C_1} + \frac{1}{C_2} + ... \tag{3-2}$$

where C_1, C_2,… are the conductances of the components in the system, such as valves, bends and constrictions.

In this system, there are two valves (in series) between the ion pump and the chamber; an all-metal valve and a Viton valve; both valves have conductance values of 34 (l/s) so, C is 0.0588 l/s and the estimated pumping speed for hydrogen is 0.05873 l/s.

In order to assess the actual pumping speed the partial pressure of hydrogen in the chamber was allowed to float up to 2.55×10^{-8} torr and the all-metal UHV valve opened quickly to allow full pumping of the chamber by the ion pump. Over period of 20 minutes, partial pressure readings were recorded until the ultimate pressure of 0.41×10^{-8} torr was reached. The results of this calibration (which represents the mean of ten similar runs) are shown below, Figure 3-6, and were fitted to the equation:

$$\ln (P - P_u) = \ln P_0 - t/(V/S) \tag{3-3}$$

which is derived from the pumping equation for the pressure, P, at a time, t:

$$P = P_u + P_0 \exp(-\frac{t}{V/S}) \tag{3-4}$$

where P_0 is the initial pressure, P_u is the ultimate hydrogen partial pressure, V is the volume of the chamber, S is the pumping speed.

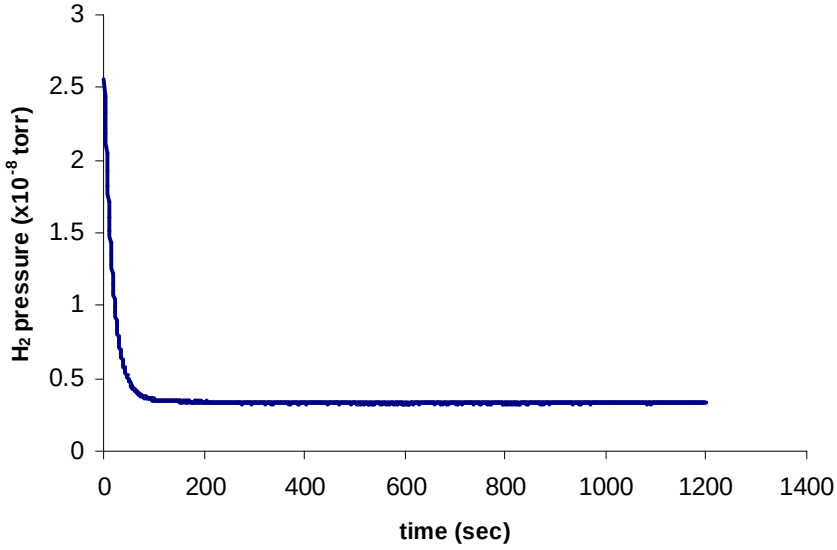

Figure 3-6: Hydrogen partial pressure readings for 20 minutes after rapid valve opening.

Figure 3-7 shows the individual readings plotted on a log-linear scale along with the best fit straight line ($\ln(P-P_u) = -0.0215\ t + 7.754$), giving a pumping speed of 0.05805 (l/s) which is very close to the estimated pumping speed (S = 0.05873(l/s)).

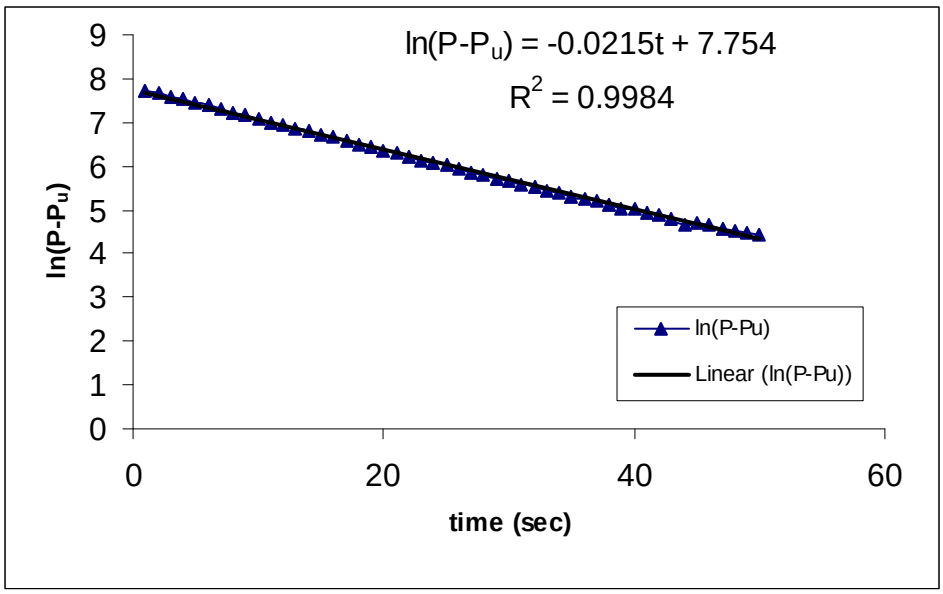

Figure 3-7: Pumping equation fit to Figure 3-6.

So, the pumping rate of hydrogen at the ultimate partial pressure of hydrogen of 0.41×10^{-8} torr:

$$Q = S \times P = 0.05805 \times 0.41 \times 10^{-8} \times 1.33 = 3.135 \times 10^{-10}\ \text{mbar.l/s} \qquad (3\text{-}5)$$

The hydrogen pumping rate given in equation (3-5) should be smaller than the hydrogen flux introduced into the vacuum system through the membrane during the permeation experiment in order that this flux can be detected by the residual gas analyser and used for analysis.

The above calibration is essential for deriving the parameter β which is calculated from the fit mentioned in Figure 3-7 as $\beta = 2.15\times10^{-2}$ (s^{-1}). This will be used later (as detailed in chapter four) for assessing the pumping rate phase lag and then used for the analysis of experiments in chapters five and six.

Pure nickel, as will be discussed further in chapter five, is a metal of well known hydrogen permeation characteristics (diffusion coefficient, solubility) and with no surface or trap effects as it does not corrode when in contact with alkaline solutions (0.1N NaOH in this work) and contains few interstitial sites with abnormal

characteristics. Therefore, nickel has been chosen for the calibration/validation experiments against which the technique was proven.

A rough estimation of the hydrogen flux through a nickel sample is given below. One study of hydrogen permeation through nickel is chosen because of its simplicity and the clear steady-state calculations of the permeation parameters, (Santos and Miranda, 1998), in which the diffusivity D is given as 4.4×10^{-14} m^2/s and the subsurface concentration C is given as 113 mol H_2/ m^3 (although the experiments were done at 40°C the difference is not significant for the design calculations carried out here).

From Fick's first law, assuming a steady-state with an exit concentration near zero, the flux can be calculated as:

$$J = \frac{DC}{L} = \frac{4.4\times10^{-14}\times113}{0.25\times10^{-3}} = 1.98\times10^{-8}\ \text{mol } H_2/m^2s \tag{3-6}$$

where L is the thickness of the sample (0.25 mm in this work). The above unit can be converted into (mbar.l/s) taking into account the surface area of the sample in contact with hydrogen, A (m^2), the universal gas constant R (mbar.l/mol H_2.K) and the absolute temperature T (K):

$$J = 1.98\times10^{-8}\times A\times R\times T = 1.98\times10^{-8}\times0.00255\times83.14\times313 \Rightarrow$$
$$J = 1.3\times10^{-6}\ \text{mbar.l/s} \tag{3-7}$$

This value of the flux is higher than the hydrogen pumping rate estimated earlier, so it is expected that the hydrogen flux entering the vacuum chamber will be detectible in the pressure provided that the same sub-surface concentration can be obtained.

3.3.2 Vacuum System Maintenance

Before running any experiments, it is an essential requirement to have the vacuum system as clean and sound as possible. This will ensure that the outgassing and leak rates are small, measurable by a low ultimate hydrogen partial pressure. The leak rate and the outgassing rate can be minimised by careful assembly (including mounting of

the specimen) and the outgassing rate is reduced by careful handling of internal parts and by baking out the system (including all components) up to the allowed temperature.

In the vacuum system described earlier, Figure 3-1, a total pressure in the range of 10^{-8} mbar was typically achieved with a hydrogen partial pressure in the range of 10^{-9} mbar.

Following a sample change, i.e. opening the system to atmosphere, the system has to be baked out thoroughly to get back to the previously-mentioned state of total pressure of 10^{-8} mbar and partial pressure of hydrogen not bigger than 10^{-9} mbar. The reason for the first requirement is to ensure that the leak rate and outgassing rate are acceptably low as the ratio of partial pressure of hydrogen to total pressure can vary due to hydrogen exposure in earlier experiments.

Heating tapes from VG Scienta were used for the bakeout process. The tapes were wrapped around all fittings, valves and also the ion pump body, after removing its magnets.

The process of baking out the system started with the ion pump as it can be baked up to 350°C. This was done to remove lightly-bonded hydrogen gas deposited in previous experiments. After that, another bakeout was carried out for the whole system up to 200°C as this is the maximum temperature for baking out the body of the RGA. Figure 3-8 shows the vacuum system wrapped with heating tapes while baking out.

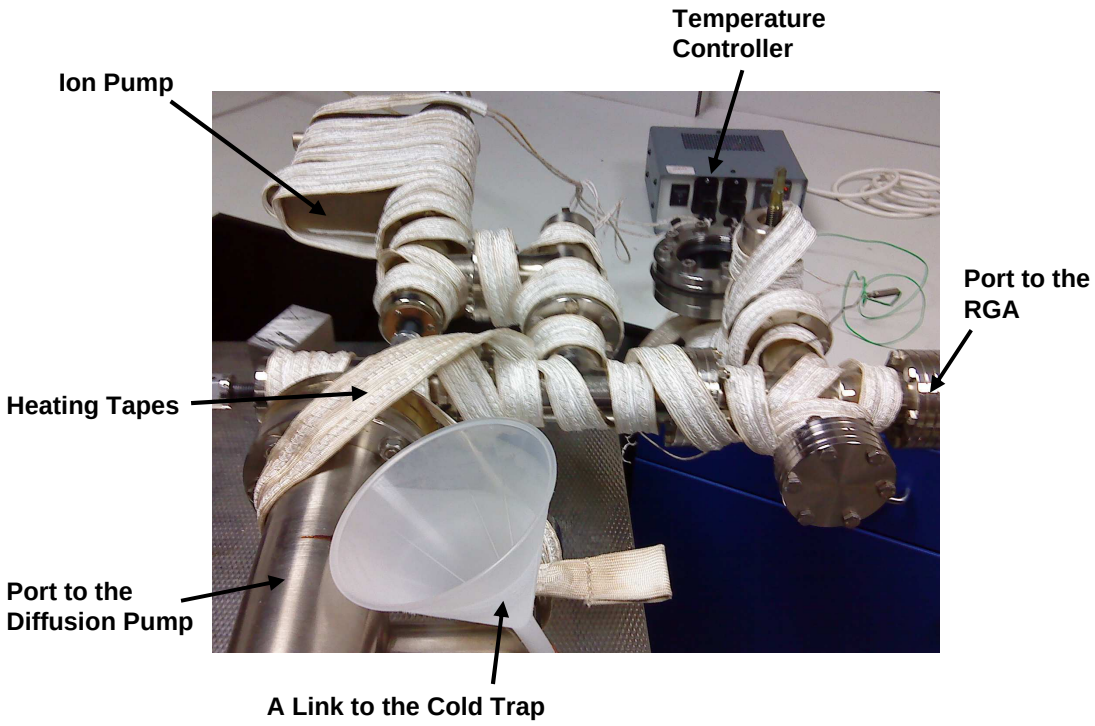

Figure 3-8: Baking out the vacuum system.

Baking out was done with the diffusion pump pumping all gases and vapours out of the system, the diffusion pump being backed by the rotary pump. Liquid nitrogen LN_2 was regularly added to a cold trap attached to the mouth of the diffusion pump to stop any backstreaming into the chamber. Finally the RGA filament was outgassed into the ion pump. Typically, a bakeout sequence would take about 48 hours.

3.4 Experimental Methodology

Hydrogen was introduced to the entry side of the membrane by applying an electrical potential to the electrochemical cell containing 0.1N NaOH. The potential was modulated about an appropriate level (as a sine wave) and the corresponding (modulated) electrical current was measured using the potentiostat. At the exit side of the membrane, which was in contact with the ultra-high vacuum chamber, the corresponding modulated hydrogen partial pressure was measured using the mass spectrometer. All data were acquired synchronously.

The phase lag (φ) and the amplitude ratio (Λ) between the potential or current and the partial pressure of hydrogen were calculated by obtaining the Fourier Coefficients of the

first harmonic of the averaged signals of the potential, current and hydrogen partial pressure.

Given that the frequency was known, signal averaging was undertaken by summing points one period apart (for each signal, the input and the output) into a single sinusoidal wave with one period (2π); then the phase lag and the amplitude ratio between the averaged signals were calculated. Figure 3-9 shows a schematic representation of signal averaging for a sinusoidal wave in which the averaged wave is given as follows:

$$B(t) = \frac{\sum_{n=0}^{N} A_{t+nT}}{N} \tag{3-8}$$

where N is the number of periods.

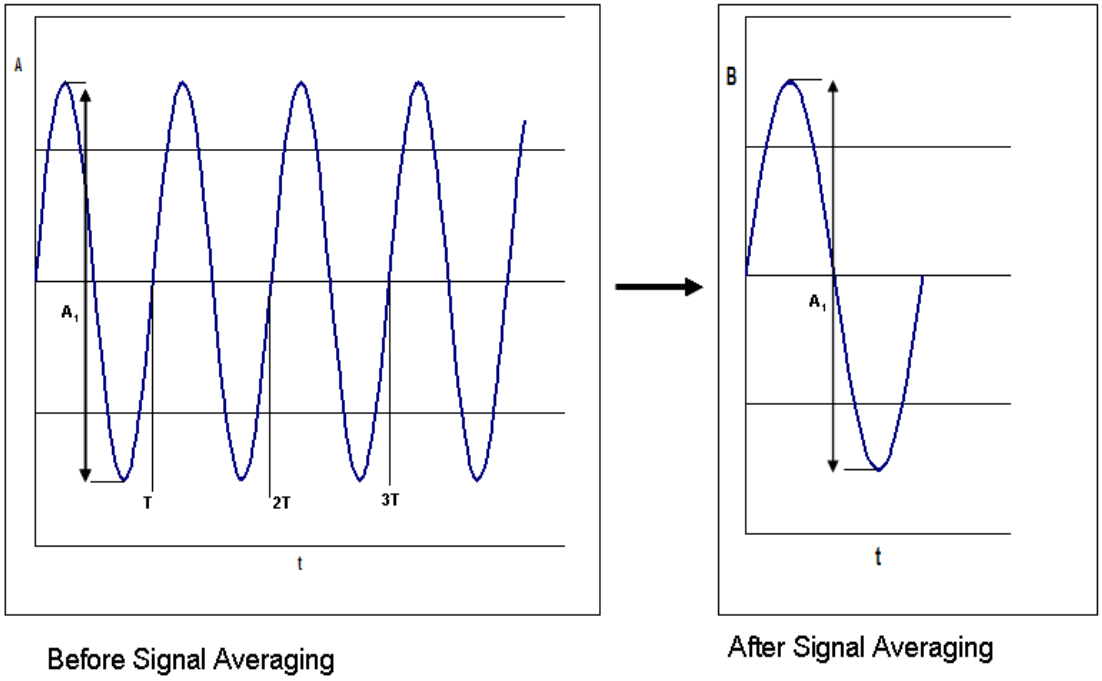

Figure 3-9: Signal averaging.

Any periodic signal (of period 2*L*) can be represented by a Fourier series, (Stroud, 1996):

$$f(x) = a_0 + \sum_{i=1}^{\infty}\left(a_i \cos\frac{i\pi}{L}x + b_i \sin\frac{i\pi}{L}x \right) \tag{3-9}$$

where a_0, a_i, and b_i are the Fourier Coefficients of *f(x)*.

Since the input is nominally a sinusoid of controlled period, *T*, and the input and output signals are averaged to give *N* points over a single period for $0 \le t \le T$, the mean value and the first Fourier Coefficients are given by:

$$a_0 = \frac{1}{T}\sum_{n=0}^{N} f_{t_n} \tag{3-10}$$

$$a_1 = \frac{2}{T}\sum_{n=0}^{N} f_{t_n} \cos\frac{2\pi t_n}{T} \tag{3-11}$$

$$b_1 = \frac{2}{T}\sum_{n=0}^{N} f_{t_n} \sin\frac{2\pi t_n}{T} \tag{3-12}$$

where the f_{t_n} are the values of potential, current or pressure.

Higher order Fourier Coefficients are not of interest since they should, in principle, be small and, anyway, the experiments at higher frequencies should yield similar information.

The phase of each signal is given as:

$$\varphi_k = \tan^{-1}\left(\frac{a_1}{b_1}\right) \tag{3-13}$$

and the amplitude as:

$$\Lambda_k = \sqrt{a_1^2 + b_1^2} \tag{3-14}$$

where *k* may represent potential, current or hydrogen partial pressure.

The primary interest in this work is the relationship between the input and output signals expressed by the phase lag and amplitude ratio, respectively:

$$\varphi = \varphi_o - \varphi_i \tag{3-15}$$

$$\Lambda = \Lambda_o / \Lambda_i \tag{3-16}$$

where the subscript '*o*' represents the partial pressure of hydrogen and the subscript '*i*' represents current or potential.

3.5 Assessment of the Required Potential and Frequency

Prior to applying the modulated electrical potential in a systematic series of experiments, it was necessary to assess a suitable potential that will allow enough hydrogen to be dissolved in the entry side of the specimen in order that a measurable hydrogen partial pressure could be detected on the exit side of the specimen (the vacuum side). It was also essential to estimate the range of amplitudes and frequencies over which a detectable amplitude and phase would appear in the pressure.

For the nickel specimen, an initial value of potential was chosen as E = -1650 mV vs. SCE (the negative sign denoting a cathodic charging) taken from Santos and Miranda (1997), who carried out a hydrogen permeation study on pure nickel. The response in current and hydrogen partial pressure was recorded over a period of several hours and then decrements of -100 mV were added to the initial value (-1650 mV) until a satisfactory response of hydrogen partial pressure was detected. Figures 3-10 to 3-13 show, respectively, the applied electrical potential at a value of E = -2000 mV vs. SCE applied as a square wave of period 21467 seconds along with the corresponding current (mA), and the corresponding hydrogen partial pressure (torr); the potential in Figure 3-10 was plotted as -E. Figure 3-13 shows too the minimum half period and acceptable amplitude for each sinusoidal cycle of the partial pressure that responds to the potential sinusoidal signal in order to be detected and recorded. The build-up transient of partial pressure, in Figure 3-13, corresponds to applying a constant potential and the decay part corresponds to stopping the hydrogen charging i.e. when there is no applied potential.

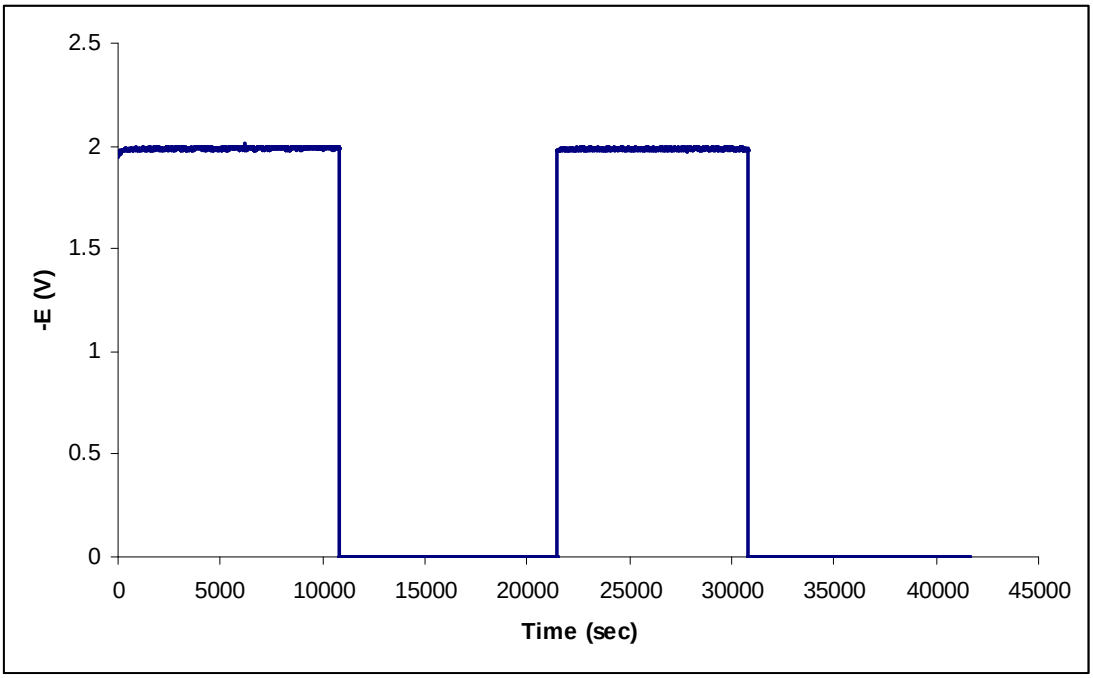

Figure 3-10: Electrical potential applied as a square wave.

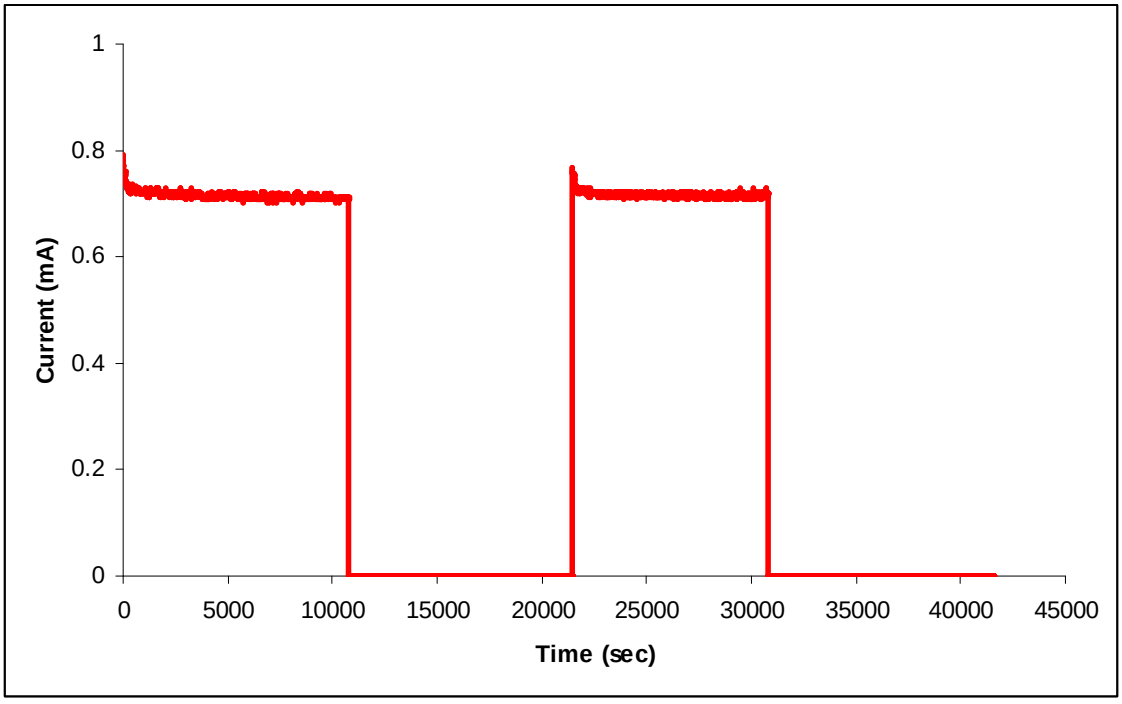

Figure 3-11: The corresponding current for the applied potential shown in Figure 3-10.

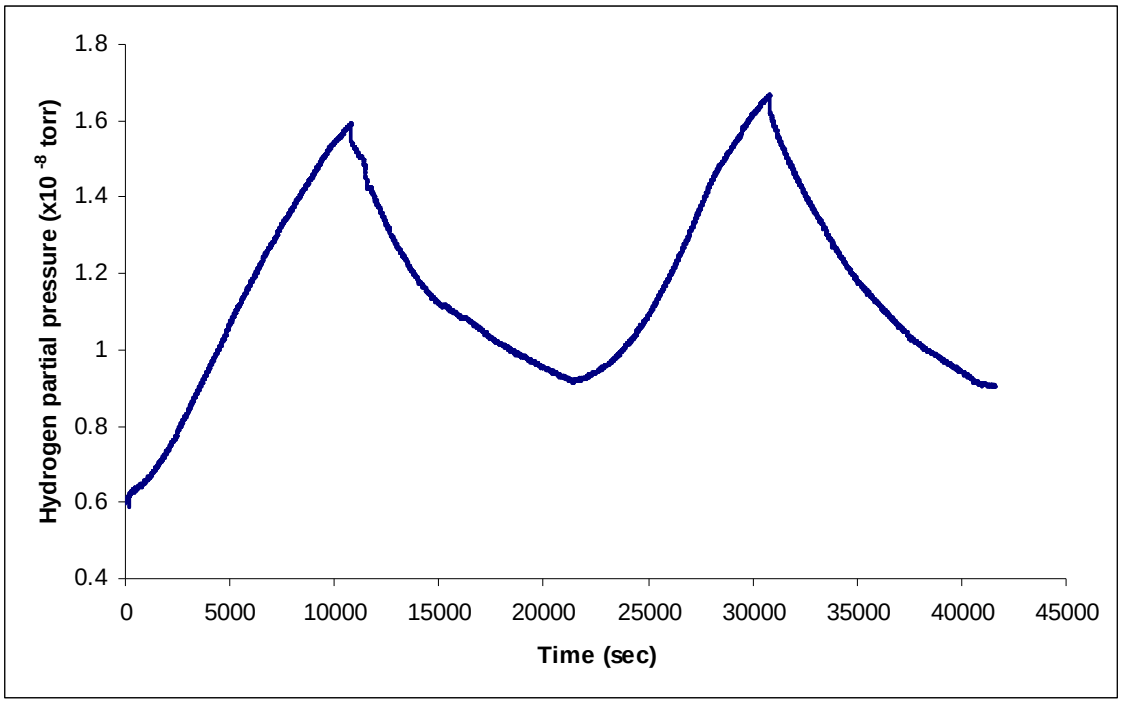

Figure 3-12: Hydrogen partial pressure as a response to the applied potential shown in Figure 3-10.

The graphs above showed a good response (in hydrogen partial pressure) and it was decided that the function for the potential oscillations to be used for the actual oscillatory permeation experiments for nickel would be:

$$E = 2000 + 1000\sin(2\pi\omega t) \tag{3-17}$$

where ω is the frequency (Hz) and t is time (sec).

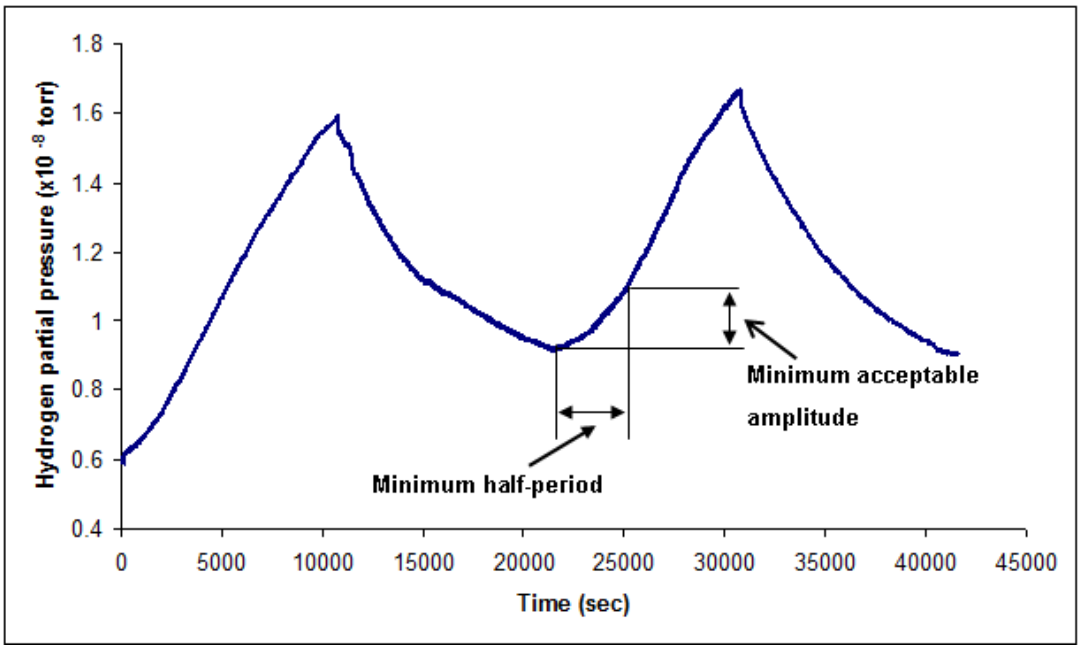

Figure 3-13: Hydrogen partial pressure from Figure 3-14 with the minimum amplitude and half period.

3.6 List of Experiments

The range of frequencies used for all permeation experiments was 1.3×10^{-5} up to 7×10^{-4} Hz (16 different frequencies were used). The readings of all variables (electrical potential, current and partial pressure of hydrogen) were recorded at a sampling rate of one reading per 10 seconds for at least 15 cycles at each frequency.

Material	Temperature	Potential (mV vs. SCE)
Nickel	22°C	$E = 2000 + 1000\sin(2\pi\omega t)$
Nickel	60°C	$E = 2000 + 1000\sin(2\pi\omega t)$
Annealed En24	22°C	$E = 1500 + 1000\sin(2\pi\omega t)$
Quenched En24	22°C	$E = 1500 + 1000\sin(2\pi\omega t)$
Quenched and tempered En24	22°C	$E = 2000 + 1000\sin(2\pi\omega t)$

Table 3-2: List of the materials used for the permeation experiments along with temperatures and potentials.

Table 3-2 summarises the target values of potential for each of the experiments. In the event, the actual values achieved in a given charging solution were not exactly as set, but differences were relatively small and could be taken into account in the ratios.

For a given experiment and at each applied frequency, the current and hydrogen partial pressure were measured and the phase lag and amplitude ratio were calculated; then those were plotted against the square root of the applied frequency to derive the relative permeation data such as the diffusion and solubility coefficients and other kinetic parameters.

Chapter 4

Data Analysis and Mathematical Model

The experiments consist of controlling and measuring the electrochemical potential, E, in a solution on one side of a metal membrane and measuring the response in the corrosion current, I, at the entry surface, and the flux of hydrogen, J, passing through the membrane.

The aim of this chapter is to set out the laws of diffusion, trapping and surface reaction in terms of their effect on the rate of permeation of hydrogen gas through a metal membrane into a pumped ultra high vacuum (UHV) chamber, as illustrated schematically in Figure 4-1, and to derive some analytical expressions for the relationship between the experimental measurements (current and pressure as a function of time) and the thermodynamic and kinetic parameters controlling permeation. These expressions are then used to analyse the data in order to extract the values of the parameters.

Accordingly, the differential equations describing the diffusion of hydrogen into the metal are identified and the solutions are presented. The effects of phenomena taking place on the surface and the bulk are modelled and the relevant differential equations solved. Two separate sections are devoted to showing graphically and mathematically, the influence of different surface and bulk parameters on the permeation process.

4.1 Controlling Differential Equations and Boundary Conditions

A general permeation system is described in Figure 4-1 consisting of three sections: an electrolyte from which hydrogen is produced, a membrane of the studied metal, and an output chamber consisting of an evacuated gas space. To describe the kinetics of this system, the membrane is considered to be a single solid phase of thickness l and uniform cross-section A in the plane perpendicular to the flow of the diffusing hydrogen.

Hydrogen enters this membrane at the input chamber, where the potential is subject to modulation at an angular frequency ω about a fixed central value E_S, and leaves the membrane to enter the output chamber, which has a volume V and is evacuated by a

pump operating at a constant speed *S*. Pressure in this chamber oscillates with the same angular frequency ω about a central value, p_{ss}, whose magnitude represents the balance between the hydrogen flow and any leakage and outgassing from the walls of the chamber Q_{og} , and pump rate.

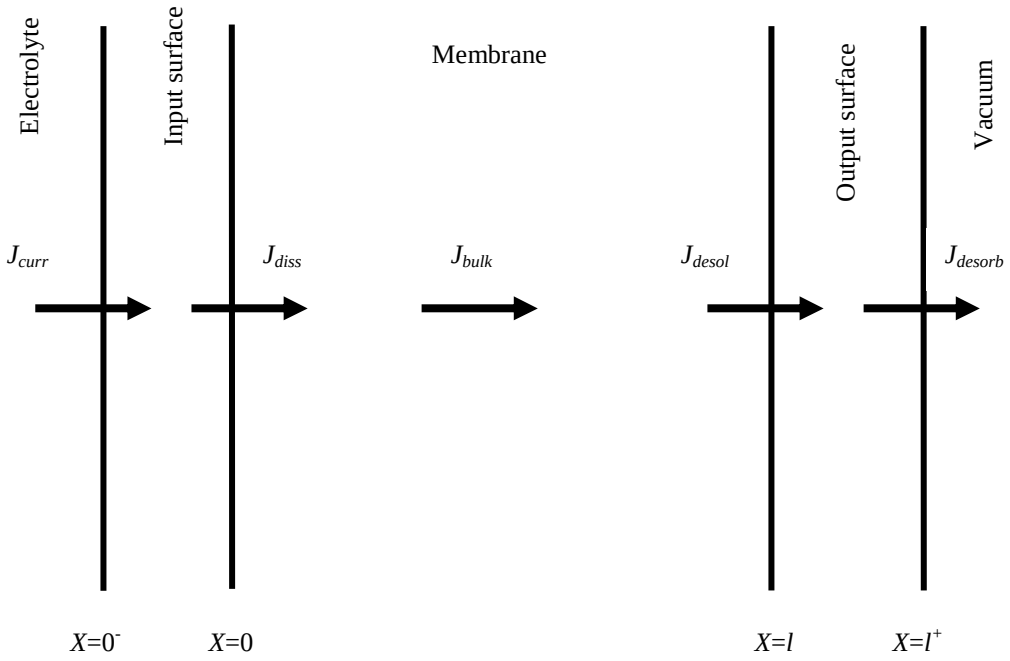

Figure 4-1: Kinetic description of permeation.

The permeation process starts by the accumulation of hydrogen produced by applying a cathodic potential to the membrane surface so a kinetic description of the hydrogen evolution/dissolution process is required. Once dissolved, hydrogen will flow down the chemical potential gradient by a process of diffusion which may or may not involve trapping. Once at the output surface, the dissolved hydrogen must recombine before leaving the surface as hydrogen gas. Therefore, three distinct sets of processes need to be taken into account, those occurring at or in; the input surface, the bulk metal, and the output surface.

4.1.1 Input and Output Surfaces

In the experiments, the hydrogen dissolution process is stimulated by changing the electrochemical potential in an electrolyte so the driving potential for dissolution can be

expressed as a hydrogen partial pressure using the Nernst Equation, (Bockris et al., 1965):

$$E = E_0 + \frac{RT}{F} pH - \frac{RT}{2F} \ln(P_{H_2}) \tag{4-1}$$

where E is the applied potential, and E_0 is the standard potential for the hydrogen dissolution reaction:

$$H^+ + e^- \Leftrightarrow \tfrac{1}{2} H_2 \tag{4-2}$$

Since the only kinetic effect occurring at the surface is that associated with the dissolution of hydrogen into the metal, the fluxes at the input surface can be described as follows:

$$J_{curr}(t) = \frac{i(t)}{F};\ J_{diss}(t) = k_3\theta(t) - k_4 C_0(t) \tag{4-3}$$

where $i(t)$ is the measured current density, θ is the surface coverage and C_0 is the input surface concentration.

The factors k_3 and k_4 are (unknown) kinetic parameters associated with the dissolution of the hydrogen, whereas any phase lag between the current and the potential will be indicative of a surface hold-up associated with the arrival of hydrogen at the surface.

At the output surface, the de-solution process does not involve an electrolyte so the surface processes can be described in simple de-sorption terms:

$$J_{desol}(t) = k'_4 C_l(t) - k'_3\theta'(t);\ J_{desorp}(t) = k'_2\theta'^2(t) - k'_1 p(t) \tag{4-4}$$

where k'_1, k'_2, k'_3 and k'_4 are kinetic parameters associated with the de-solution process, θ' and C'_l are the surface coverage and concentration, respectively, at the output surface.

4.1.2 Bulk Processes

One-dimensional diffusion of a single component can be treated by the use of Fick's first law, which indicates that the flux, *J*, of a diffusant down a concentration gradient is governed by the diffusion coefficient, *D*:

$$J = -D \frac{\partial C}{\partial x} \tag{4-5}$$

Fick's second law can be derived by considering an elemental slice of material of a thickness *dx*, and considering Fick's first law to apply to the fluxes into and out of this element, Figure 4-2:

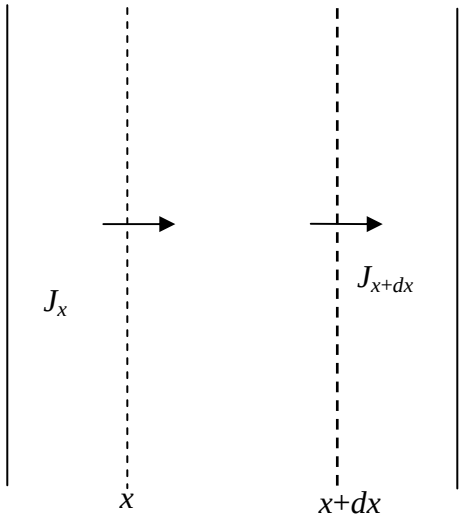

Figure 4-2: Application of Fick's first law to a material of an elementary thickness *dx*.

Provided that there are no sources or sinks within the element, any difference between inflow and outflow will give rise to a change in concentration with time in the element, i.e. Fick's second law:

$$\frac{\partial C}{\partial t} = D \frac{\partial^2 C}{\partial x^2} \tag{4-6}$$

A number of models exist for diffusion of hydrogen in metals involving trapping, and it is recognized that trapping plays an important part in the susceptibility of alloys to hydrogen damage.

An oscillatory technique is particularly valuable in examining trapping, because, in general, the time lags introduced by trapping will have a different frequency response to those introduced by bulk diffusion. In order to examine this, it was not considered so important to choose between the various trapping models, but to have a tool (preferably with a small number of parameters) for assessing the magnitude of the trapping effect. For this reason, the McNabb-Foster trapping model (McNabb and Foster, 1963) was selected, in which reversible trapping is characterized by two variables; *p*, the probability that an occupied trap will release a captive atom within one second and *k*, the probability of a diffusing atom becoming trapped.

By considering a hydrogen mass balance including both trapping and Fickian diffusion, McNabb and Foster described the transport of hydrogen by the simultaneous differential equations:

$$\frac{\partial C}{\partial t} + N\,\frac{\partial n}{\partial t} = div\,(DgradC\;) \tag{4-7}$$

$$\frac{\partial n}{\partial t} = kC(1-n) - pn \tag{4-8}$$

where *N* is the number of traps per number of all diffusion and traps sites in the material (dimensionless), and *n* is the fraction of the traps which are occupied.

In order to make the problem more tractable, it is assumed that *n* and *C* are small, so that the term *(C×n)* can be neglected, and the coupled differential equations above can now be written as a single equation, expressed in one dimension as:

$$-D\frac{\partial^3 C}{\partial t \partial x^2} + \frac{\partial^2 C}{\partial t^2} - pD\frac{\partial^2 C}{\partial x^2} + \left(p + kN\right)\frac{\partial C}{\partial t} = 0 \tag{4-9}$$

4.2 Solutions to the Differential Equations

In this section, solutions to Fick's second law are presented for cases where there are oscillatory boundary conditions with and without surface hold-up. A solution is also presented for the McNabb and Foster trapping equation (4-9) with oscillatory boundary conditions.

4.2.1 Surface Equilibrium and Steady-State

Under steady state conditions, $\left(\frac{\partial C}{dt}\right) = 0$ and, for one-dimensional diffusion, C is a function of x only, which simplifies the solution to Fick's second law considerably:

$$\frac{\partial C}{\partial t} = 0 = D\frac{\partial^2 C}{\partial x^2} \tag{4-10}$$

which is easily integrated to give the steady-state flux:

$$J_s = \int_{C_0}^{C_L} D\frac{\partial^2 C}{\partial x^2}\,dx = \left[\frac{dC}{dx}\right]_{C_0}^{C_L} \tag{4-11}$$

If, further, the surface concentrations are assumed to be in equilibrium with the respective partial pressures of a diatomic gas (hydrogen here):

$$C = K(p)^{0.5} \tag{4-12}$$

where K is the Sievert's solubility coefficient, then the steady-state flux of diffusant is given by:

$$J_s = \frac{D(C_0 - C_l)}{l} = \frac{DK[(p_0)^{1/2} - (p_l)^{1/2}]}{l} \tag{4-13}$$

where C_0, C_l, p_0 and p_l are subsurface concentration and partial pressure at the input and output surfaces, respectively.

The effective equilibrium hydrogen partial pressure at the input surface can be obtained from the electrochemical reaction:

$$H^+(aq) = \frac{1}{2} H_2(g) \tag{4-14}$$

for which the potential is given by the Nernst Equation, (4-1), mentioned earlier.

This permits control of the equilibrium input partial pressure through the potential in an electrolyte of known hydrogen ion concentration (pH). The output surface can be supposed to be in equilibrium with the UHV side through Sievert's law. When the output chamber is pumped, the pressure is given by a balance between gas entering the system (outgassing, leakage and flux) and the pump rate:

$$\frac{\partial p_{out}}{\partial t} = \frac{JART}{V} - \beta(p_{out} - p_u) \tag{4-15}$$

where P_u is the pressure achieved when no flux enters the chamber, β (1/s) is a rate constant related to the continuous chamber pumping and A and V are the membrane area and chamber volume respectively. At the steady state $\frac{\partial p_{out}}{\partial t} = 0$ so that the steady state pressure and permeation flux are linearly related through a number of measurable parameters.

4.2.2 The Quasi-Stationary State with Surface Equilibrium

A number of approaches exist to solve Fick's second law with variable surface concentrations (Crank, 1975).

Cummings et al (1984) showed that, for the relatively simple case where an oscillatory input:

$$p_0(t) = p_{ss} + \hat{p}e^{iwt} \tag{4-16}$$

giving a surface concentration (assuming equilibrium) of:

$$C_0(t) = K\sqrt{p_{ss} + \hat{p}e^{i\omega t}} \cong K\sqrt{p_{ss}} + \frac{K\hat{p}}{2\sqrt{p_{ss}}}e^{i\omega t} \tag{4-17}$$

has been allowed to come to a quasi-stationary state (i.e. the output is allowed to settle to an oscillatory function with constant mean value), the concentration as a function of *x* and *t* (general solution of Fick's second law) can be written as:

$$C(x,t) = C_{ss} + [Ae^{a(x-l)} + Be^{a(l-x)}]e^{i\omega t} \tag{4-18}$$

where *A* and *B* are arbitrary complex constants and *a* is also a complex number, $C_{ss} = K\sqrt{p_{ss}}$, $a = (1+i)k$, $k = \sqrt{\frac{\omega}{2D}}$, ω is the frequency (Hz) and *D* is the hydrogen diffusion coefficient (m^2/s); thus, the parameter *kl* is introduced as a dimensionless frequency parameter which will be used throughout the text to show the variations of the phase lag and the amplitude ratio between the input parameter (current) and the output one (pressure).

Using $C_0(t)$ as above and $C_l(t) = 0$ as the two boundary conditions, the arbitrary constants *A* and *B* can be found as follows:

$$x = 0 \Rightarrow C_0(t) = K\sqrt{p_{ss}} + \frac{K\hat{p}}{2\sqrt{p_{ss}}}e^{i\omega t} = C_{ss} + [Ae^{-al} + Be^{al}]e^{i\omega t} \Rightarrow \tag{4-19}$$

$$\frac{K\hat{p}}{2\sqrt{p_{ss}}} = Ae^{-al} + Be^{al} \tag{4-20}$$

$$x = l \Rightarrow C_l(t) = 0 = C_{ss} + (A+B)e^{i\omega t} \Rightarrow A = -B \tag{4-21}$$

From (4-20) and (4-21):

$$\frac{K\hat{p}}{2\sqrt{p_{ss}}} = -Be^{-al} + Be^{al} \tag{4-22}$$

then *A* and *B* can be given as:

$$B = \frac{K\hat{p}}{2\sqrt{p_{ss}}(e^{al} - e^{-al})} \tag{4-23}$$

$$A = \frac{-K\hat{p}}{2\sqrt{p_{ss}}(e^{al} - e^{-al})} \tag{4-24}$$

Substituting *A* and *B* into the general solution (4-18):

$$C(x,t) = C_{ss} + \frac{K\hat{p}}{2\sqrt{p_{ss}}(e^{al} - e^{-al})}[e^{a(l-x)} - e^{a(x-l)}]e^{i\omega t} \tag{4-25}$$

Differentiating equation (4-25) gives the flux as follows:

$$J = -D\frac{\partial C}{\partial x} = -\frac{DK\hat{p}}{2\sqrt{p_{ss}}(e^{al} - e^{-al})}[-ae^{a(l-x)} - ae^{a(x-l)}]e^{i\omega t} \tag{4-26}$$

Setting $x = l$, the harmonic part of the output flux J_{desol} can be obtained as a complex number as follows:

$$J_{x=l} = \frac{D(1+i)kK\hat{p}}{\sqrt{p_{ss}}(e^{(1+i)kl} - e^{-(1+i)kl})} \tag{4-27}$$

$$J_{desol} = \frac{DkK\hat{p}}{\sqrt{p_{ss}}(e^{kl}e^{ikl} - e^{-kl}e^{-ikl})}(1+i) \tag{4-28}$$

$$J_{desol} = \frac{DkK\hat{p}}{\sqrt{p_{ss}}[e^{kl}(\cos(kl)+i\sin(kl))-e^{-kl}(\cos(kl)-i\sin(kl))]}(1+i) \tag{4-29}$$

$$J_{desol} = \frac{DkK\hat{p}}{\sqrt{p_{ss}}[(e^{kl}\cos(kl)-e^{-kl}\cos(kl))+i(e^{kl}\sin(kl)+e^{-kl}\sin(kl))]}(1+i) \tag{4-30}$$

$$J_{desol} = \frac{DkK\hat{p}(1+i)[(e^{kl}\cos(kl)-e^{-kl}\cos(kl))-i(e^{kl}\sin(kl)+e^{-kl}\sin(kl))]}{\sqrt{p_{ss}}[(e^{kl}\cos(kl)-e^{-kl}\cos(kl))^2+(e^{kl}\sin(kl)+e^{-kl}\sin(kl))^2]} \tag{4-31}$$

Knowing that:

$$\sinh(kl)=\frac{e^{kl}-e^{-kl}}{2},\ \cosh(kl)=\frac{e^{kl}+e^{-kl}}{2},\tanh(kl)=\sinh(kl)/\cosh(kl),$$
$$\cosh^2(kl)-\sinh^2(kl)=1$$

The final formula for the flux is:

$$J_{desol} = \frac{DkK\hat{p}\cos(kl)\cosh(kl)}{2\sqrt{p_{ss}}(\sin^2(kl)+\sinh^2(kl))}[(\tan(kl)+\tanh(kl))+i(\tanh(kl)-\tan(kl))] \tag{4-32}$$

Taking the real and imaginary parts of (4-32), the amplitude and phase of this number are then given, respectively, as:

$$\left|J_{desol}\right| = \sqrt{J_{\mathrm{Re}}^2+J_{\mathrm{Im}}^2} = \frac{K\hat{p}}{2\sqrt{p_{ss}}}\frac{\sqrt{2}Dk}{\sqrt{\sinh^2(kl)+\sin^2(kl)}} \tag{4-33}$$

$$\angle J_{desol} = \arctan\left(\frac{J_{\mathrm{Im}}}{J_{\mathrm{Re}}}\right) = \arctan\left[\frac{\tanh kl-\tan kl}{\tan kl+\tanh kl}\right] \tag{4-34}$$

Equations (4-33) and (4-34) can be regarded as the amplitude ratio and the phase lag, respectively, between the input flux (as measured by the input partial pressure of hydrogen) and the output flux (as measured by the output partial pressure of hydrogen).

For brevity, the phase lag will be referred to as φ and the amplitude ratio as Λ.

Solving the pumping differential equation:

$$\frac{\partial \hat{p}_{out}}{\partial t} = \frac{\hat{J}_{desol} ART}{V} - \beta(\hat{p}_{out} - p_u) \tag{4-35}$$

A harmonic output flux boundary condition gives the amplitude ratio between the output flux and the output partial pressure of hydrogen as:

$$\left|\hat{p}_{out}\right| = \left|\hat{J}_{desol}\right| \frac{ART}{V\sqrt{\omega^2 + \beta^2}} \tag{4-36}$$

and the phase lag between the pressure in the vacuum system and the output flux:

$$\xi = \arctan \frac{\omega}{\beta} \tag{4-37}$$

The phase lag given in equation (4-37) is subtracted from the one given in equation (4-34) to give the real (effective) phase lag between the pressure in the vacuum chamber (output) and the electrical potential (input).

Figure 4-3 and Figure 4-4 show, respectively, the calculated variations of the phase lag and the amplitude ratio with the square root of frequency.

For Figure 4-3, the values of the diffusion coefficient, (2.22×10^{-14}, 5×10^{-14}, and 1.125×10^{-13} m^2/s) have been chosen from Robertson (1973) at three different temperatures (281, 295, and 310 K, respectively) with a specimen thickness of 0.25 mm for a range of frequencies between 1.3×10^{-5} and 7×10^{-4} Hz.

For Figure 4-4, the diffusion coefficient and solubility values have been chosen from the same study (K values are 0.009, 0.01266, and 0.0165 (mol $H_2/m^3.mbar^{0.5}$) at temperatures 281, 295 and 310 K, respectively), (Robertson, 1973).

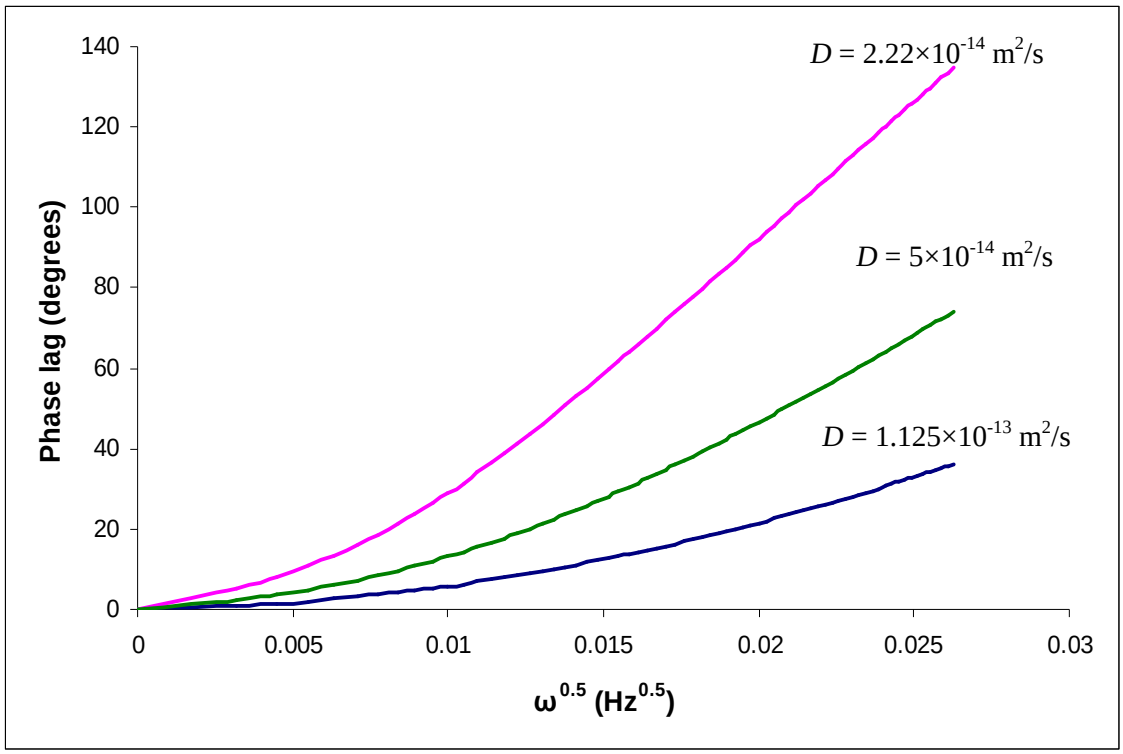

Figure 4-3: Calculated variation of the phase lag φ with the square root of frequency for equilibrium conditions using diffusion coefficients from Robertson (1973).

Figure 4-3 has a characteristic shape in that, at higher frequencies, it tends to become linear. This provides a very rapid means of determining the diffusion coefficient akin to the time-lag analysis approach. However, in this work, the whole curve will be fitted using a least-squares algorithm. Figure 4-4 exhibits a characteristic where the amplitude is relatively constant at lower frequencies, but tends to drop off rapidly as frequency increases before levelling out towards zero at the highest frequencies. The range of frequency chosen for any experiment is a trade-off between obtaining a measurable phase lag (low frequency limit) and a measurable amplitude ratio (high frequency limit) and this may require an adjustment of the pumping rate by choking the UHV valve.

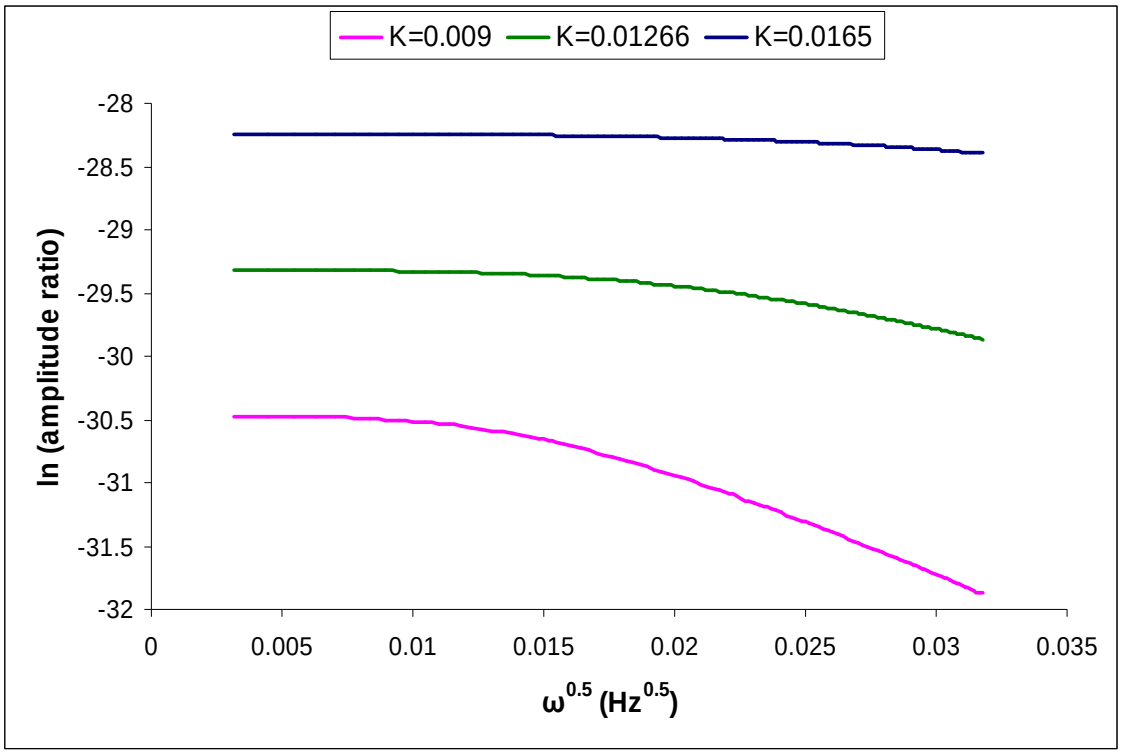

Figure 4-4: Calculated variation of the amplitude ratio Λ with the square root of frequency using solubility coefficients, K (mol $H_2/m^3.mbar^{0.5}$), from Robertson (1973).

In the absence of any trapping, surface or pumping effects, results from the experiments can be fitted to equations (4-33) and (4-34) to determine the diffusion coefficient D and the solubility coefficient K, separately.

4.2.3 Surface Effects

The assumption of surface equilibrium in the previous section implies that the fluxes J_{curr} and J_{diss} and, similarly, the fluxes J_{desol} and J_{desorb} are each in phase, Figure 4-1.

In the experiments of this work, the output surface is clean relative to the input surface so the assumption of output surface equilibrium is reasonable and so the focus here will be on modelling the hold-up at the input surface.

For the steady-state component of the solution, we can still write $J_s = \frac{D(C_0 - C_l)}{l}$ but C_0 is no longer simply related to the input partial pressure of hydrogen or the potential given by the Nernst Equation.

The flux approaching the surface J_{curr} is directly measured and it can be assumed that this is the rate of adsorption, although much of the adsorbed hydrogen will combine on the surface and be evolved as hydrogen gas.

Expressions for the rate of desorption (i.e. hydrogen evolution), absorption and desolution can be written, so that the steady state can be expressed in terms of the surface coverage, θ, as:

$$J_s = \frac{D(C_0 - C_l)}{l} = \frac{D\left[C_0 - K(p_l)^{1/2}\right]}{l} = J_{curr} - k_{ev}\theta^2 = k_{abs}\theta - k_{des}C_0 \tag{4-38}$$

This can be rearranged to give:

$$J_s\left(1 + \frac{D}{k_{des}l}\right) = \frac{Dk_{abs}}{k_{des}l}\sqrt{\frac{J_{curr} - J_s}{k_{ev}}} - \frac{DK(p_l)^{1/2}}{l} \tag{4-39}$$

Because both J_{curr} and J_s are measured, it is, in principle, possible to separate bulk and surface effects even in a steady-state experiment.

For the harmonic part of the solution, we can return to the general solution to Fick's second law for the harmonic component:

$$C(x,t) = [Ae^{a(x-l)} + Be^{a(l-x)}]e^{i\omega t} \tag{4-40}$$

Again, taking $C_l = 0$ gives $A = -B$.

The remaining boundary condition can be found by considering the harmonic flux across the input interface as follows:

$$J_{x=0} = k_{abs}\theta - k_{des}C_0 = -D(\frac{\partial C}{\partial x})_{x=0} \tag{4-41}$$

$$J_{x=0^-} = J_{curr} - \omega k_{ev}\theta^2 \tag{4-42}$$

and, since:

$$J_{x=0} - J_{x=0^-} = -\frac{\partial \theta}{\partial t} \tag{4-43}$$

an equation for the surface concentration (in terms of the current) can be written as:

$$J_{curr} = -\frac{D}{k_{abs}}\left(\frac{\partial C}{\partial x \partial t}\right)_{x=0} + \frac{k_{des}}{k_{abs}}\left(\frac{\partial C}{\partial t}\right)_{x=0} - (2k_{ev} - k_{abs})\frac{D}{k_{abs}}\left(\frac{\partial C}{\partial x}\right)_{x=0}$$

$$+ (2k_{ev}\theta\frac{k_{des}}{k_{abs}} - 2k_{des})C_0 \tag{4-44}$$

Substituting the appropriate derivatives of the general solution (4-40), with $A = -B$, into the above equation, gives:

$$\frac{J_{curr}}{e^{i\omega t}} = -\frac{D}{k_{abs}}[i\omega a A(e^{-al} + e^{al})] + \frac{k_{des}}{k_{abs}}[i\omega A(e^{-al} - e^{al})] - [2k_{ev} - k_{abs}]\frac{D}{k_{abs}}[aA(e^{-al} + e^{al})]$$

$$+ [2k_{ev}\theta\frac{k_{des}}{k_{abs}} - 2k_{des}][A(e^{-al} - e^{al})] \tag{4-45}$$

Simplifying this expression gives A as a complex number in the form:

$$A = \frac{J_{curr}}{f(m + in)e^{i\omega t}} \tag{4-46}$$

Substituting A back into the general solution gives:

$$C(x,t) = A[e^{a(x-l)} - e^{a(l-x)}]\frac{J_{curr}}{f(m+in)} \tag{4-47}$$

So, the flux at $x = l$ is given as follows:

$$J = -D\frac{\partial C}{\partial x} = -2Dak\frac{J_{curr}}{f(m+in)} \tag{4-48}$$

i.e.
$$\frac{J}{J_{curr}} = \frac{-2Dk}{f(m^2+n^2)}[(m+n)+i(m-n)] \tag{4-49}$$

From this, the amplitude ratio and the phase lag between J and J_{curr} are given as:

$$\left|\frac{J}{J_{curr}}\right| = \frac{2\sqrt{2}Dk}{f\sqrt{m^2+n^2}} \tag{4-50}$$

$$\angle\frac{J}{J_{curr}} = \arctan\frac{m-n}{m+n} \tag{4-51}$$

where

$$f = \frac{2\cos(kl)\cosh(kl)}{k_{abs}}$$
$$m = b + c + (b-c)\tan(kl)\tanh kl) + e\tanh(kl) + d\tan(kl)$$
$$n = c - b + (c+b)\tan(kl)\tanh(kl) + e\tan(kl) - d\tanh(kl)$$
$$b = Dk\omega$$
$$c = Dk(k_{abs} - 2k_{ev})$$
$$d = \omega k_{des}$$
$$e = 2k_{des}(k_{abs} - k_{ev}\theta)$$

where k_{des} is the rate of desorption (m/s), k_{ev} is the rate of evolution (s^{-1}), k_{abs} is the rate of absorption (s^{-1}) and θ is the surface coverage of hydrogen (dimensionless).

Parameters in equations (4-50) and (4-51) enable a precise distinction of the nature of the surface effect on the permeation. In the following figures, the effects of each parameter on either the phase lag or the amplitude ratio, or both, are illustrated.

Figure 4-5 shows the effect (on the phase lag with $D = 5\times10^{-14}$ m^2/s) of increasing the desorption rate keeping $k_{ev} = k_{abs} = \theta = 0$, i.e. inhibiting the dissolution of absorbed hydrogen.

When $k_{ev} = k_{abs} = \theta = 0$, $c = e = 0$ and:

$$
\begin{aligned}
m &= b + b\tan(kl)\tanh(kl) + d\tan(kl) \\
n &= -b + b\tan(kl)\tanh(kl) - d\tanh(kl) \\
m - n &= 2b + d(\tan(kl) + \tanh(kl)) \\
m + n &= 2b\tan(kl)\tanh(kl) + d(\tan(kl) - \tanh(kl))
\end{aligned}
$$

So:

$$
\varphi = \arctan\frac{2b + d(\tan(kl) + \tanh(kl))}{2b\tan(kl)\tanh(kl) + d(\tan(kl) - \tanh(kl))} \tag{4-52}
$$

when $k_{des} \to \infty, \varphi \to \dfrac{\tan(kl) + \tanh(kl)}{\tan(kl) - \tanh(kl)}$

and when $k_{des} \to 0, \varphi \to \dfrac{1}{\tan(kl)\tanh(kl)}$

The variations in k_{des} are expressed within the dimensionless parameter $k_{des}.l/D$ where l is the thickness of the specimen (taken as 0.25 mm here) shown in Figure 4-5. As can be seen, the effect of increasing k_{des} from zero is to move the curve towards surface equilibrium. Since the shape of the curve does not change substantially, this parameter could be expressed within an effective diffusion coefficient.

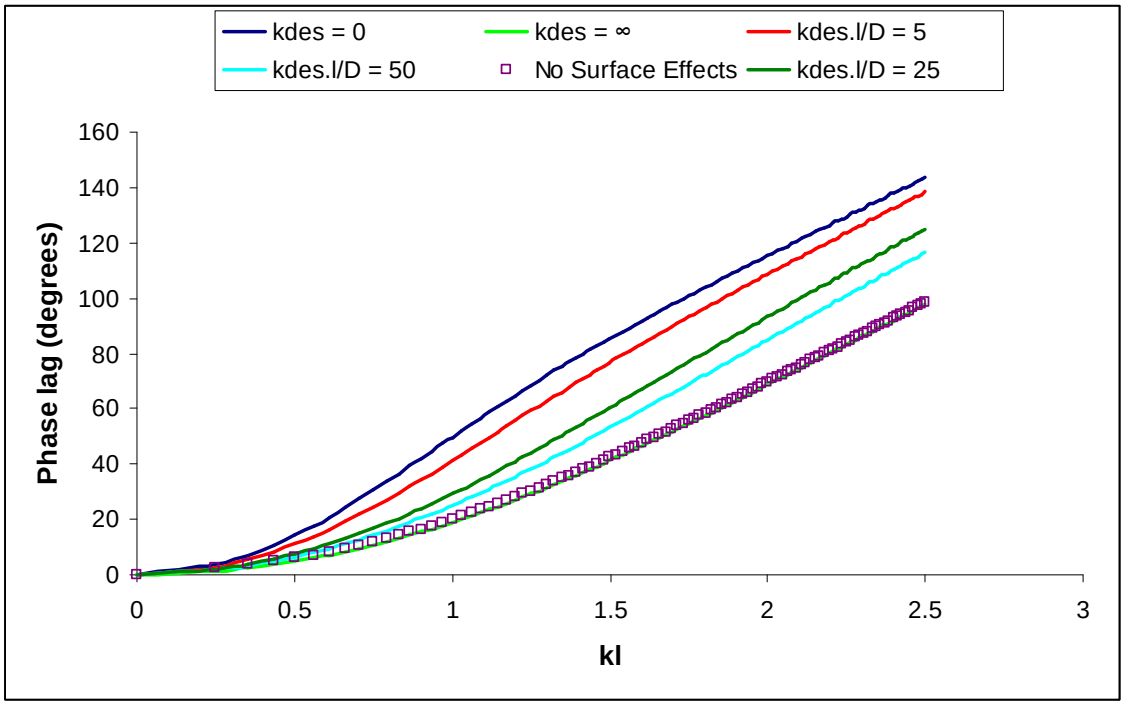

Figure 4-5: The effect of desorption on the phase lag φ and its variations with kl.

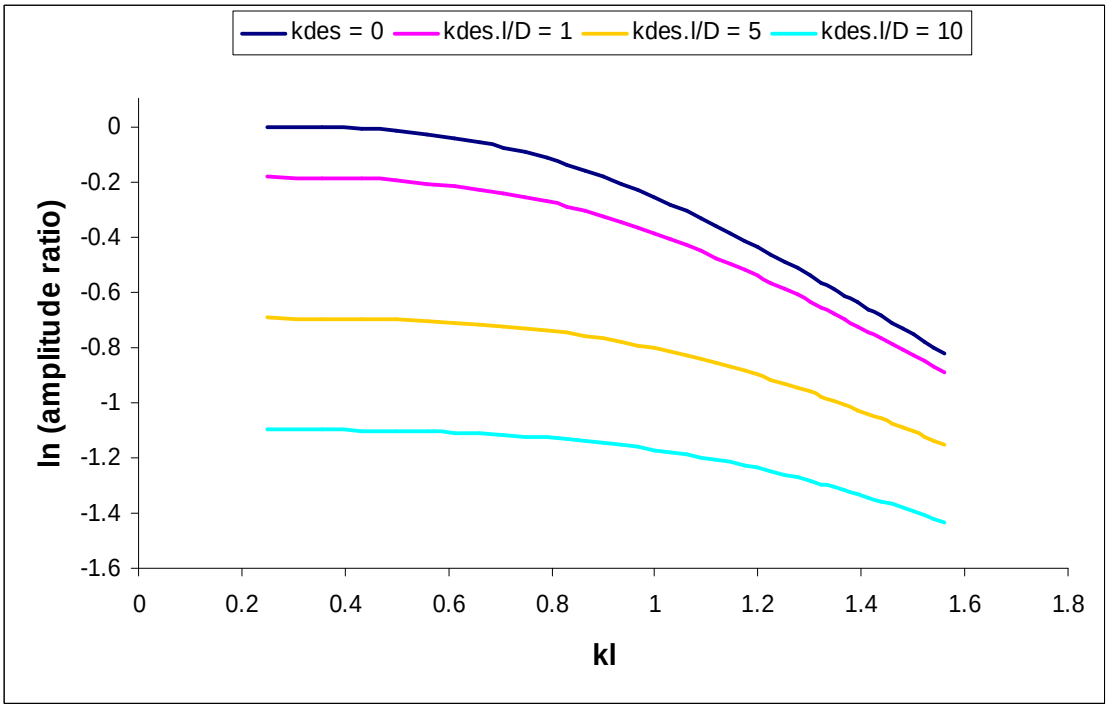

Figure 4-6: The effect of the desorption rate on the amplitude ratio Λ and its variations with kl.

As shown in Figure 4-6, the shape of the amplitude ratio curve does not change substantially either but it moves to higher values as k_{des} tends towards zero. For this figure, $k_{ev} = \theta = 0$ but $k_{abs} = 1\ s^{-1}$ (it is a requirement for the amplitude ratio calculations that k_{abs} is not zero, equation (4-50)). If $k_{abs} = 0$, the amplitude ratio becomes zero, equation (4-50), which means there is no amplitude for the hydrogen partial pressure signal and hence, there is no hydrogen permeated to the vacuum chamber.

Figure 4-7 shows how the relationship between the phase lag and the dimensionless frequency parameter kl changes with variations of k_{ev} while the other parameters k_{des}, k_{abs}, and θ are kept to zero.

When $k_{des} = k_{abs} = \theta = 0$, $d = e = 0$ and:

$$m = b + c + (b - c)\tan(kl)\tanh(kl)$$
$$n = c - b + (c + b)\tan(kl)\tanh(kl)$$
$$m - n = 2b - 2c\tan(kl)\tanh(kl)$$
$$m + n = 2c + 2b\tan(kl)\tanh(kl)$$

So:

$$\varphi = \arctan\frac{m-n}{m+n} = \frac{2b - 2c\tan(kl)\tanh(kl)}{2c + 2b\tan(kl)\tanh(kl)} \qquad (4\text{-}53)$$

when $k_{ev} \to 0$, $\varphi = \arctan\dfrac{1}{\tan kl \tanh kl}$

and when $k_{ev} \to \infty$, $\varphi = \arctan(-\tan kl \tanh kl)$

As shown in Figure 4-7, the phase lag curve changes its shape when k_{ev} increases from zero until it approaches infinity the effect being shown by the dimensionless parameter $k_{ev}.l^2/D$. Thus, it might be expected that this parameter could be detectable in the experimental data by changes in curvature of the phase plot. Figure 4-8 presents the variations of the amplitude ratio with kl when k_{ev} increases from zero to 100 (s^{-1}); it is clear that the shape of the curve does not change significantly but it tends to be lower

for higher values of k_{ev}, again not offering a variation which could be distinguished for solubility or diffusion coefficient.

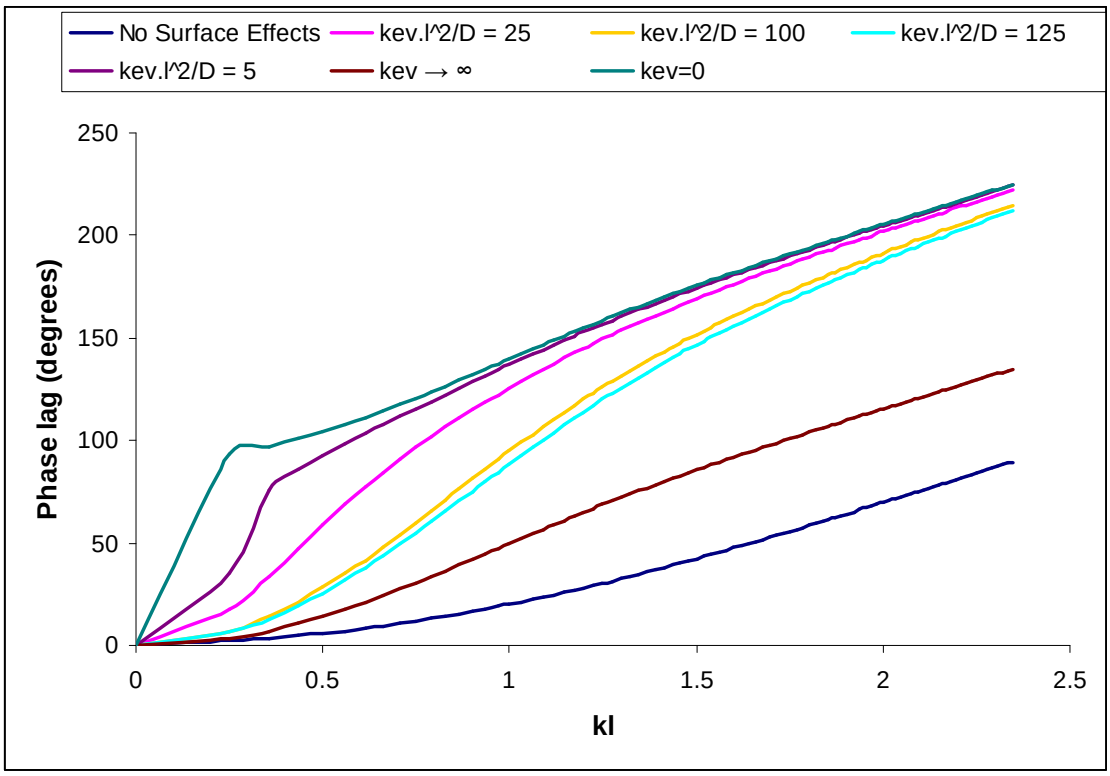

Figure 4-7: The effect of evolution on the phase lag φ and its variations with kl.

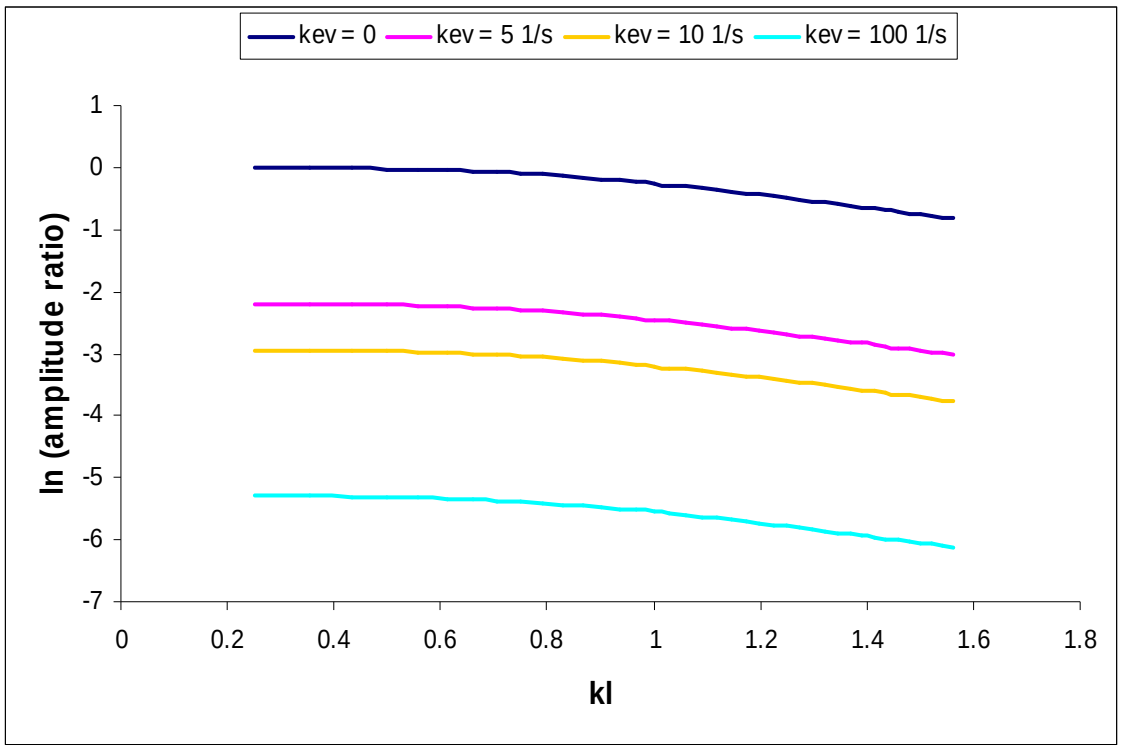

Figure 4-8: The effect of evolution on the amplitude ratio Λ and its variations with kl.

Using a similar analysis, the effect of the absorption rate, k_{abs}, on phase and amplitude is shown in Figures 4-9 and 4-10 respectively. Here the surface parameter affects the curvature of both the phase and amplitude plots suggesting a characteristic response which might be detectable in experimental data.

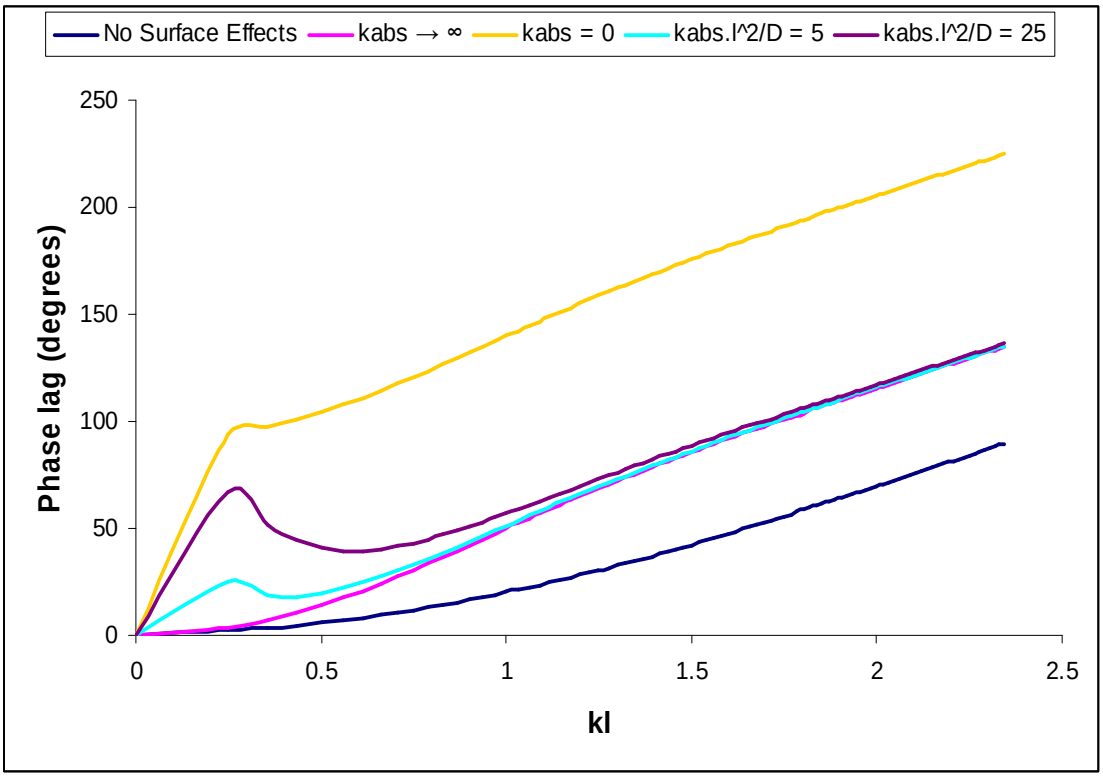

Figure 4-9: The effect of absorption rate on the phase lag φ and its variations with kl.

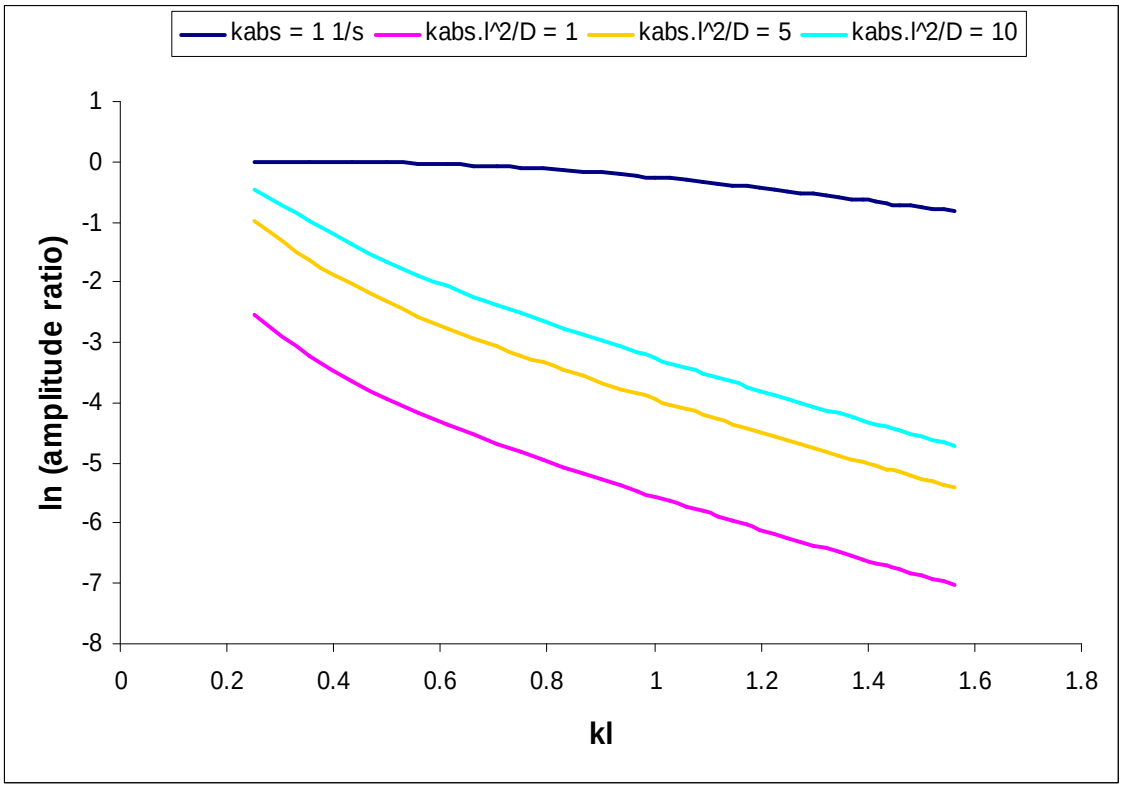

Figure 4-10: The effect of absorption rate on the amplitude ratio Λ and its variations with kl.

To assess the effect of changing the dimensionless surface coverage, θ, on the phase lag and amplitude ratio variations with kl, the parameters k_{ev} and k_{des} cannot both be zero as the effects of this parameter are always combined in the effects of both k_{ev} and k_{des}. Figure 4-11 (for the phase lag) and Figure 4-12 (for the amplitude ratio) show the effect of θ holding k_{ev} and k_{des} at unity. Again, a relatively mild effect is observed.

The foregoing analysis is somewhat artificial in that the surface kinetic parameters have each been isolated whereas, in a real case, a mixture of effects might be expected. What is evident is that surface kinetic parameters can change the shape of both the amplitude and phase plots so that distinctive evolutions of both with frequency might be expected in experimental data where a significant surface effect is present.

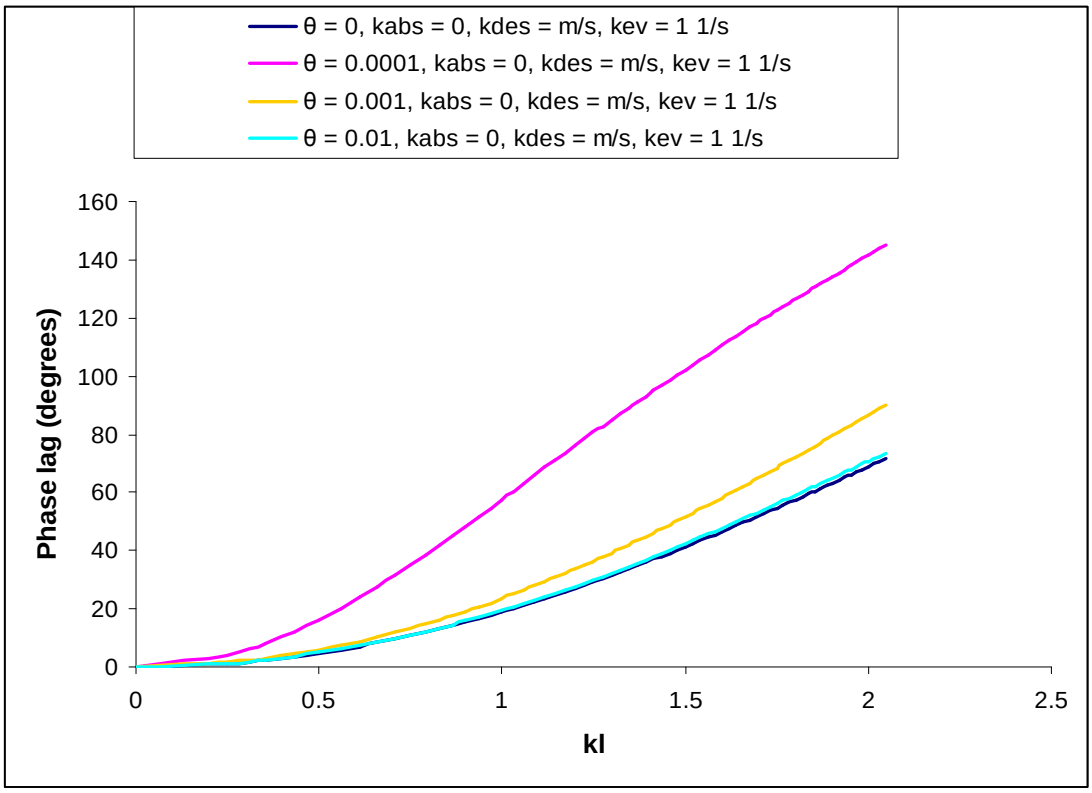

Figure 4-11: The effect of the surface coverage of hydrogen on the phase lag φ and its variations with kl.

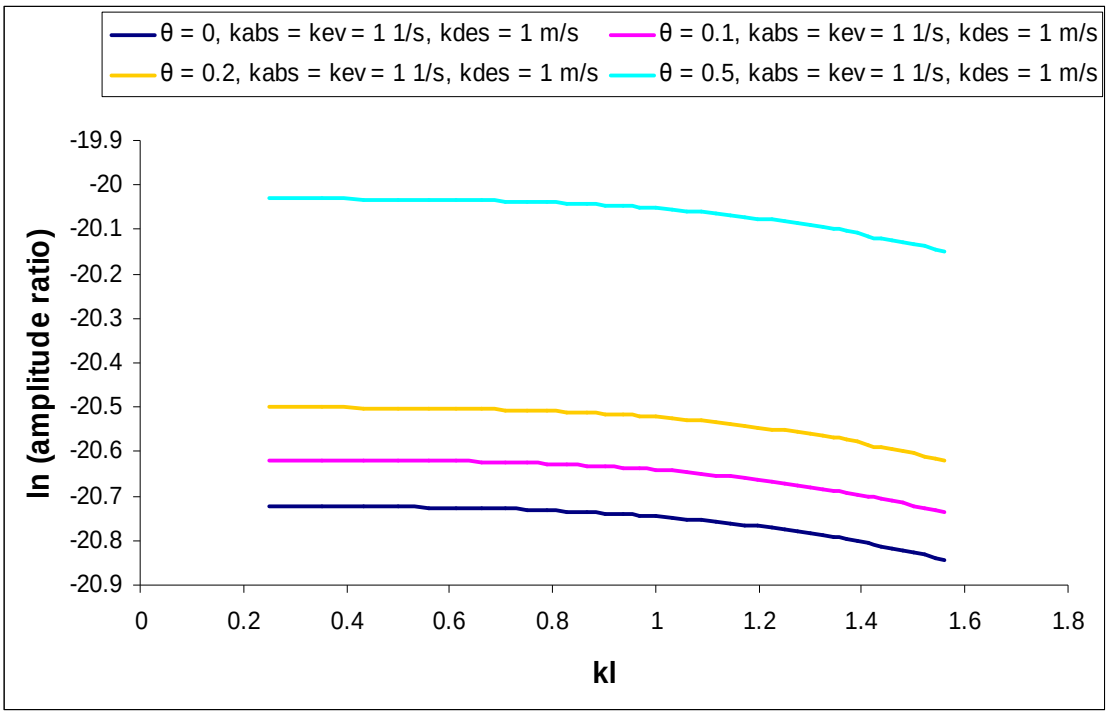

Figure 4-12: The effect of the surface coverage of hydrogen on the amplitude ratio Λ and its variations with kl.

4.2.4 Trapping

This analysis is based on obtaining a solution to the modified McNabb-Foster model (McNabb and Foster, 1963):

$$-D\frac{\partial^3 C}{\partial t \partial x^2}+\frac{\partial^2 C}{\partial t^2}-pD\frac{\partial^2 C}{\partial x^2}+(p+kN)\frac{\partial C}{\partial t}=0 \qquad (4\text{-}54)$$

where p,k, and N where defined earlier.

Assuming a solution made up of a steady-state and an oscillatory component:

$$C(x,t)=f(x)+F(x)e^{i\omega t} \qquad (4\text{-}55)$$

the third order differential equation can be rewritten as:

$$\frac{\partial^2 f}{\partial x^2} = 0 \tag{4-56}$$

$$(p + i\omega)D\frac{\partial^2 F}{\partial x^2} + [\omega^2 - (p + kN)i\omega]F = 0 \tag{4-57}$$

This gives the amplitude and phase of J_{desol} as:

$$\left|J_{desol}\right| = \frac{K\hat{p}}{2\sqrt{p_{ss}}}\frac{D\sqrt{u^2 + v^2}}{\sqrt{\sinh^2 ul + \sin^2 vl}} \tag{4-58}$$

$$\angle J_{desol} = \arctan\left[\frac{u\tanh vl - v\tan ul}{v\tan vl + u\tanh ul}\right] \tag{4-59}$$

where

$$u = B\cos\left(\tfrac{1}{2}\tan^{-1}\frac{b}{a}\right) \tag{4-60}$$

$$v = B\sin\left(\tfrac{1}{2}\tan^{-1}\frac{b}{a}\right) \tag{4-61}$$

$$B = \frac{\left(a^2 + b^2\right)^{1/4}}{\sqrt{D\left(p^2 + \omega^2\right)}} \tag{4-62}$$

$$a = kN\omega^2 \tag{4-63}$$

$$b = \omega^3 + p(p + kN)\omega \tag{4-64}$$

In the following graphs, the effect of the trapping parameters (N, k and p) on the phase lag φ and its variations with the dimensionless frequency parameter (kl) are displayed, Figure 4-13 to Figure 4-15. (It is important to mention here that k in the frequency

parameter is given as $k = \sqrt{\frac{\omega}{2D}}$ (1/m) while k in the trapping equations is the probability of a diffusing atom being trapped (s^{-1})).

When there is no trapping effect, i.e. $p, kN \to 0$, then:

$$b = \omega^3, a \to 0 \Rightarrow$$

$$B = \sqrt{\frac{\omega}{D}} \tag{4-65}$$

then

$$v = \sqrt{\frac{\omega}{D}} \sin\left(\frac{1}{2}\tan\infty\right) = \sqrt{\frac{\omega}{D}} \sin\frac{\pi}{4} \Rightarrow$$

$$v = \sqrt{\frac{\omega}{2D}} = k \tag{4-66}$$

and

$$u = \sqrt{\frac{\omega}{D}} \cos\left(\frac{1}{2}\tan\infty\right) = \sqrt{\frac{\omega}{D}} \cos\frac{\pi}{4} \Rightarrow$$

$$u = \sqrt{\frac{\omega}{2D}} = k \tag{4-67}$$

and equations (4-58) and (4-59) reduce to the conventional diffusion with surface equilibrium equations (4-33) and (4-34) for the amplitude ratio and the phase lag, respectively.

As can be seen from the relationships in equations (4-63) and (4-64), k and N always appear together as a product kN so their effects on the phase lag and the amplitude ratio

will be analysed by considering the effects of the product *kN*. Figures 4-13 to 4-16 show the effects of both *kN* and *p* on the phase lag and amplitude ratio and their variations with the square root of frequency. The value of the diffusion coefficient was chosen as 5.8×10^{-10} m^2/s from a study on iron, (Addach et al., 2005), and *l* was taken as 0.25 mm.

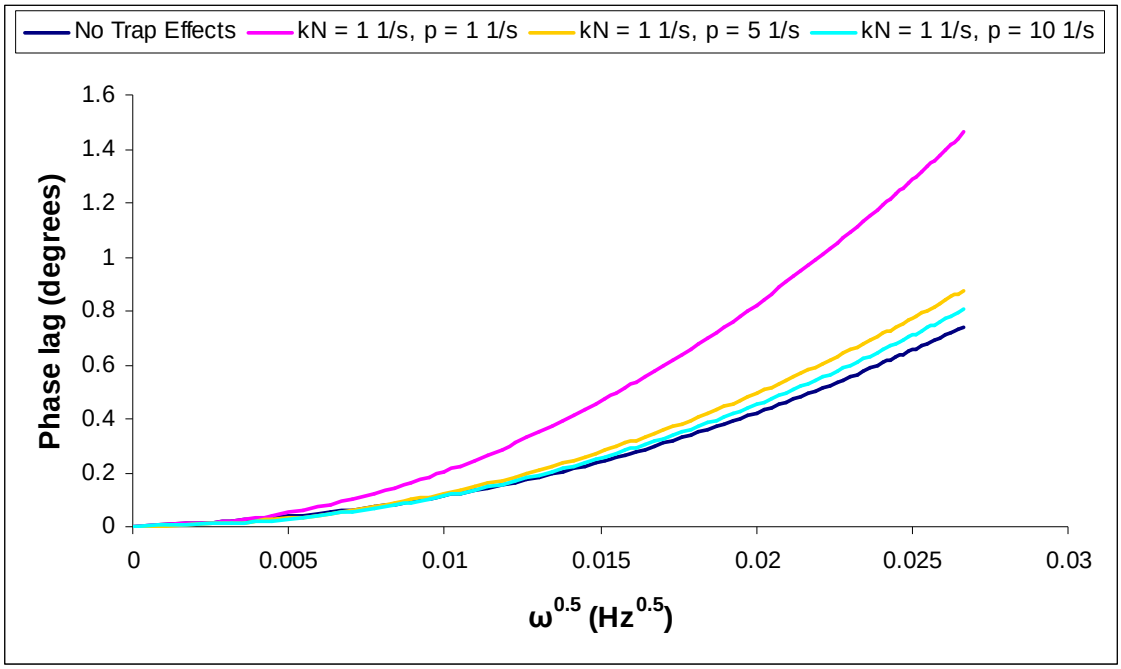

Figure 4-13: The effect of *p* (s^{-1}) on the phase lag φ with variations with the square root of frequency.

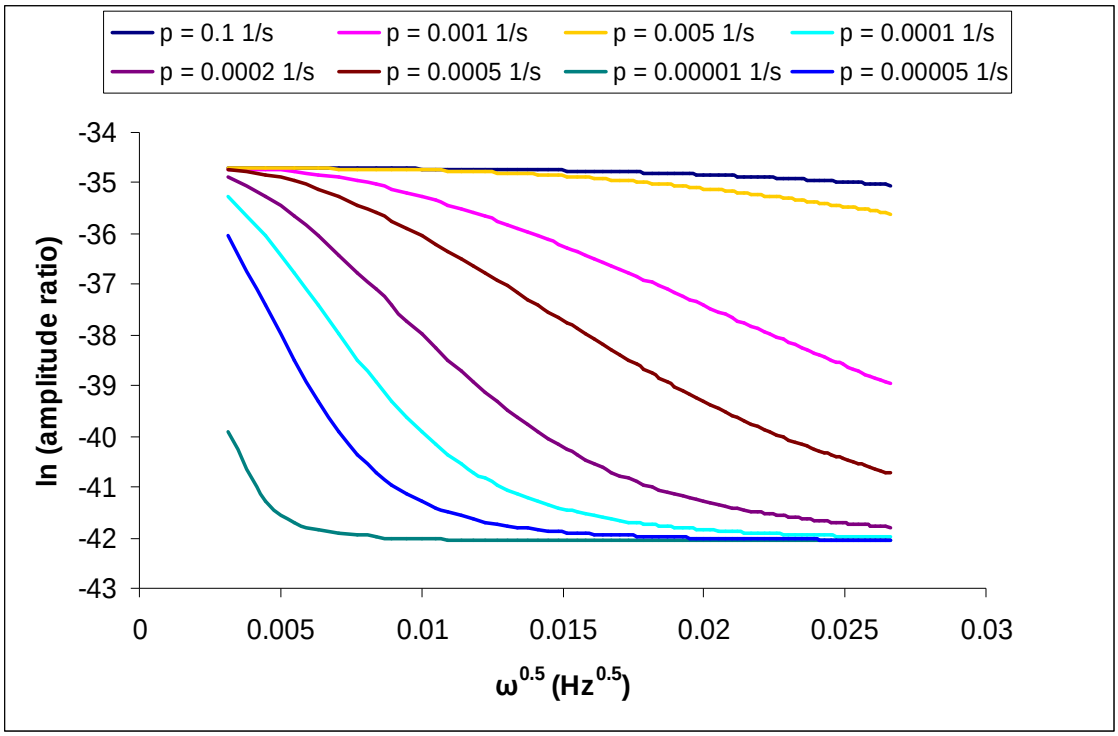

Figure 4-14: The effect of p (s^{-1}) on the amplitude ratio Λ with variations with the square root of frequency (kN = 1 s^{-1}).

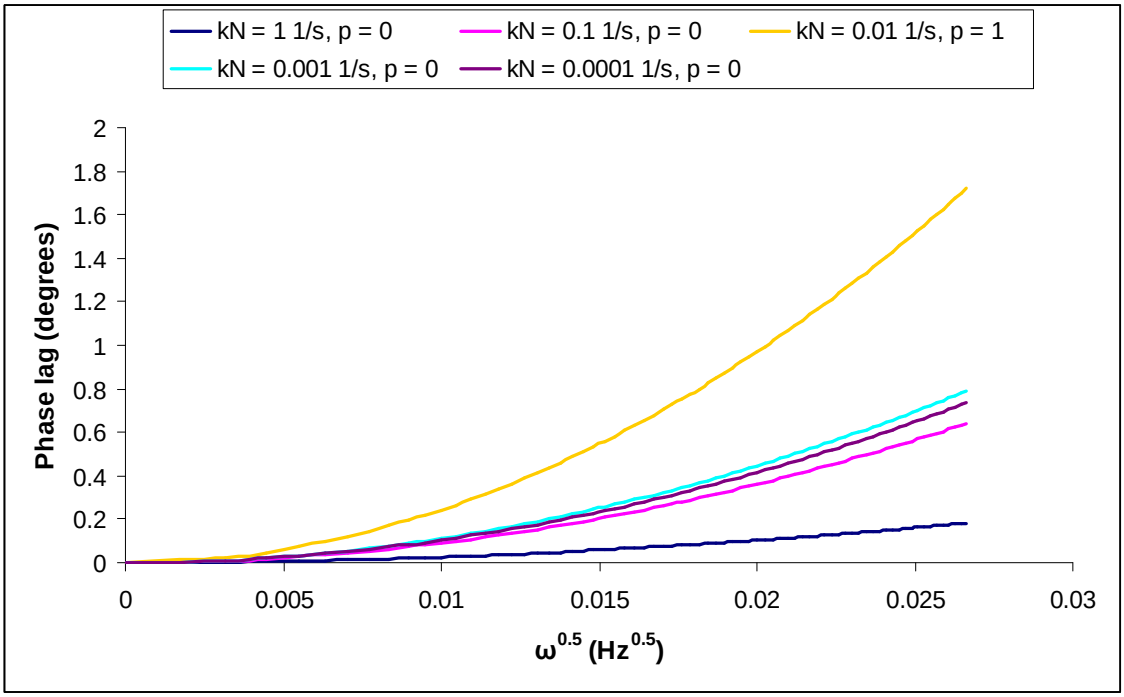

Figure 4-15: The effect of *kN* on the phase lag φ and its variations with the square root of frequency.

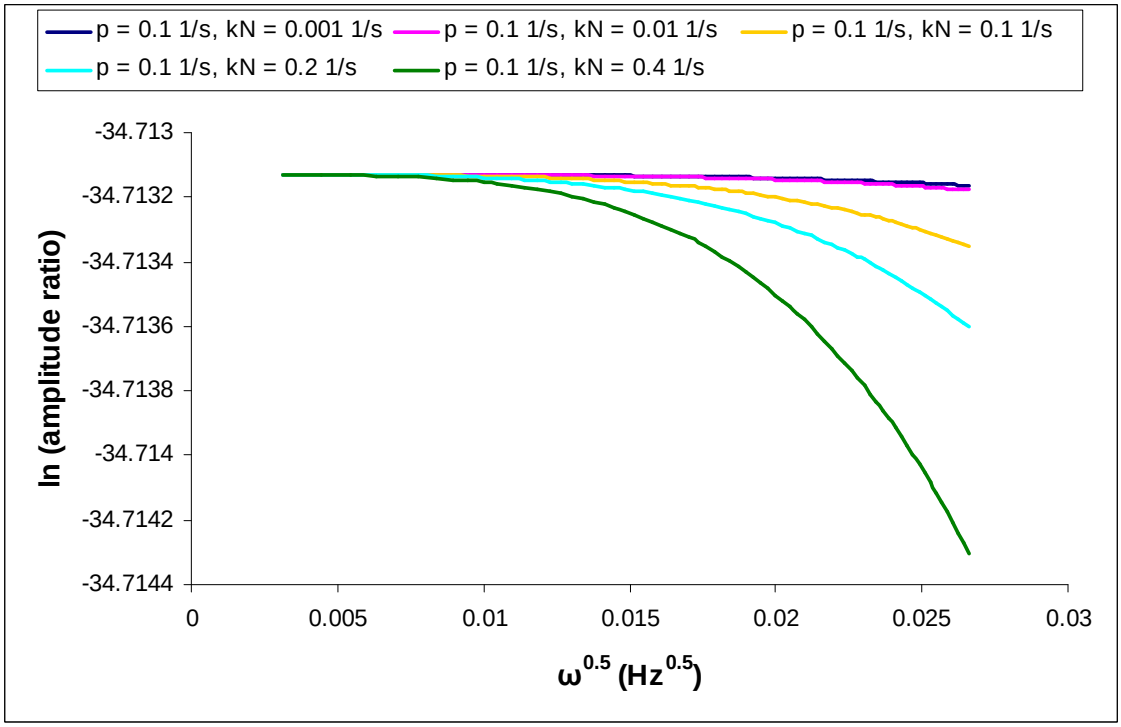

Figure 4-16: The effect of *kN* on the amplitude ratio Λ and its variations with the square root of frequency.

As can be seen, the trapping parameters do not introduce the types of curvature change expressed by the surface parameters. This opens up the possibility of discriminating between surface effects and trapping effects if the diffusion coefficient and solubility are known or if a multi-parameter fit is used.

Chapter 5

Results and Analysis (Nickel)

A commercial purity nickel (99% Ni) specimen, supplied by Goodfellow, was used for the calibration experiments because of its well-known and reproducible permeation characteristics and because nickel will not corrode when in contact with the alkaline environment used in this work (0.1N NaOH) so the specimen can be used as many times as needed without any concern about possible surface or bulk damage.

The cathodic potential was modulated between 1000 and 3000 mV vs. SCE at frequencies ranging from 1.3×10^{-5} up to 7×10^{-4} Hz. The potential, current and hydrogen partial pressure readings were recorded at a sampling rate of one reading per 10 seconds for at least 15 cycles for each frequency.

The nickel specimen, as mentioned earlier in chapter three, was a disc of 0.25 mm thickness and 83 mm diameter, and the effective area in contact with the chemical solution (the input surface) was 25.5 cm^2.

The validation experiments were done at two temperatures, 22ºC and 60ºC.

5.1 Permeation Experiments on Nickel at 22ºC

The potential was applied cathodically as a sine wave and was set to oscillate about a value of 2000 mV vs. SCE:

$$E = 2000 + 1000\sin(2\pi\omega t) \tag{5-1}$$

where ω is the applied frequency (Hz) and t is time (sec).

The following two sub-sections show the potential, current and hydrogen partial pressure results, as examples, when two different frequencies were applied; one of those frequencies is chosen in the range of 10^{-4} Hz (relatively high) and the other is in the range of 10^{-5} Hz (relatively low). For clarity, only a few cycles of the applied/measured parameters are shown.

5.1.1 *Potential, Current and Hydrogen Partial Pressure at 7×10^{-5} Hz*

Figures 5-1 to 5-3 show the applied electrical potential (V) vs. SCE and the corresponding electrical current (mA) and hydrogen partial pressure (torr) with an applied frequency of 7×10^{-5} Hz. As can be seen from the potential graph, the maximum value was a little less than 3 V vs. SCE but this is calibrated out in the analysis.

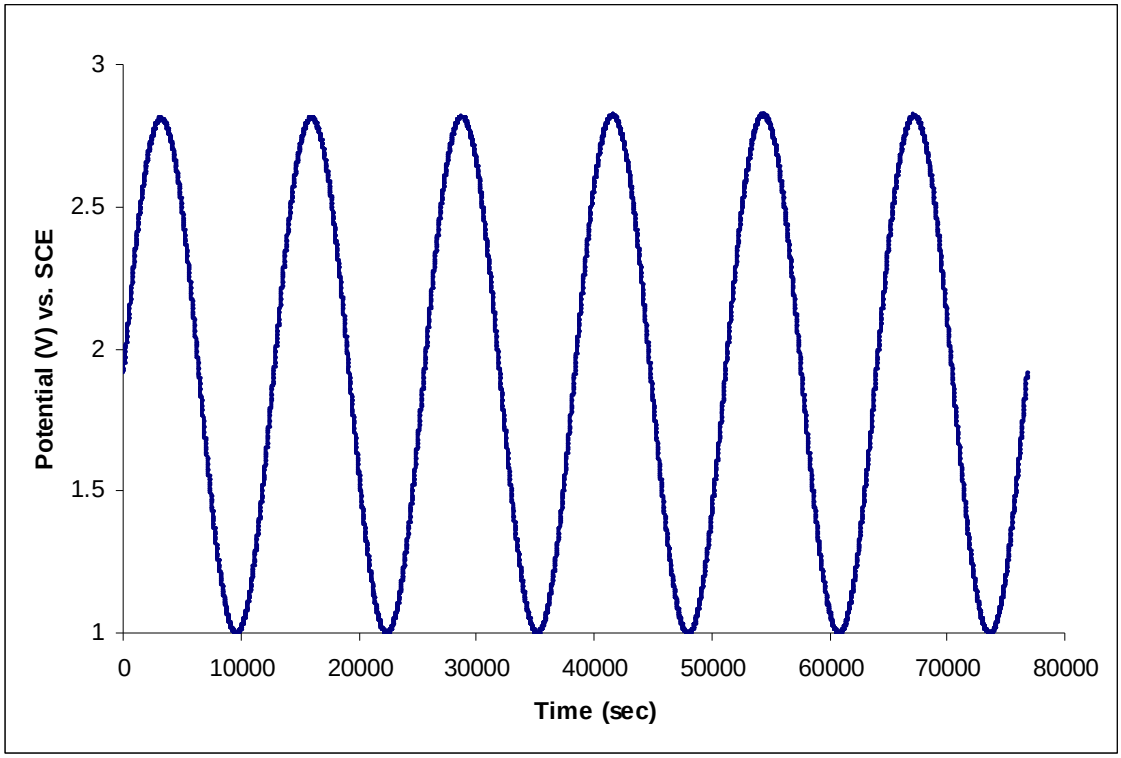

Figure 5-1: Electrical potential applied as a sine wave for nickel at 7×10^{-5} Hz and 22ºC.

The current (Figure 5-2) is not sinusoidal, due to the non-linear relationship between current and potential. However, it is clear, even by inspection, that the main frequency of oscillation will be the same as for the potential, and so the analysis can still be performed using the Fourier Coefficients of the first harmonic.

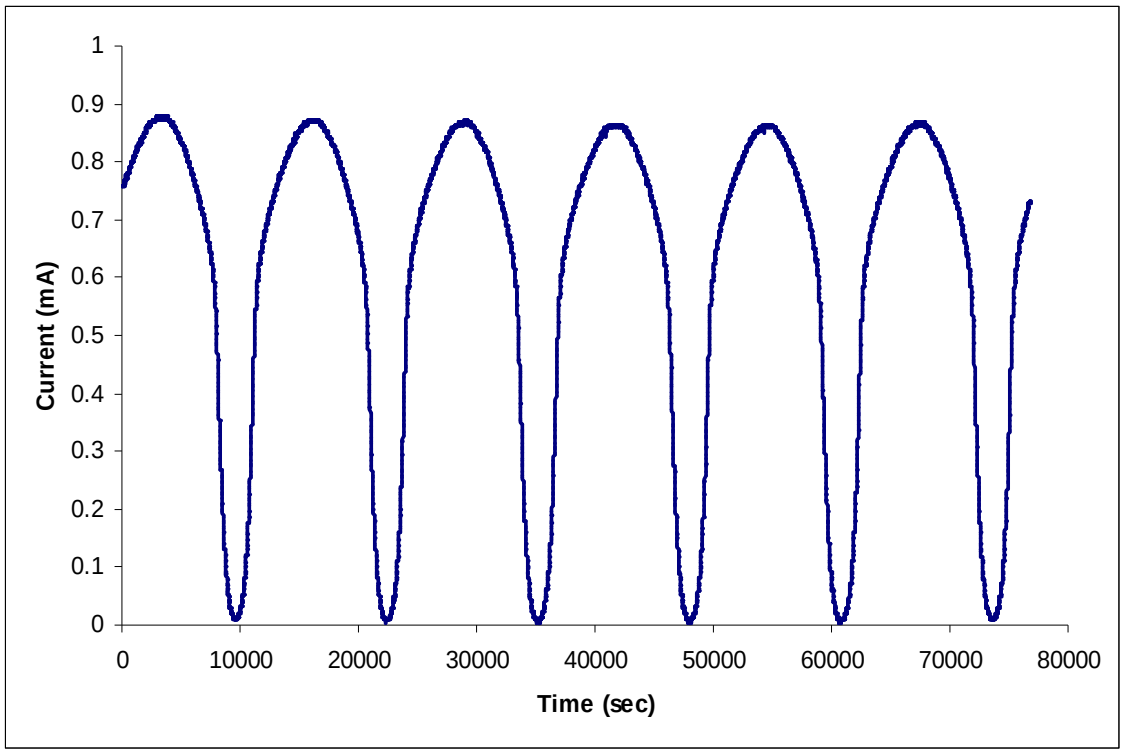

Figure 5-2: Current response to the potential shown in Figure 5-1.

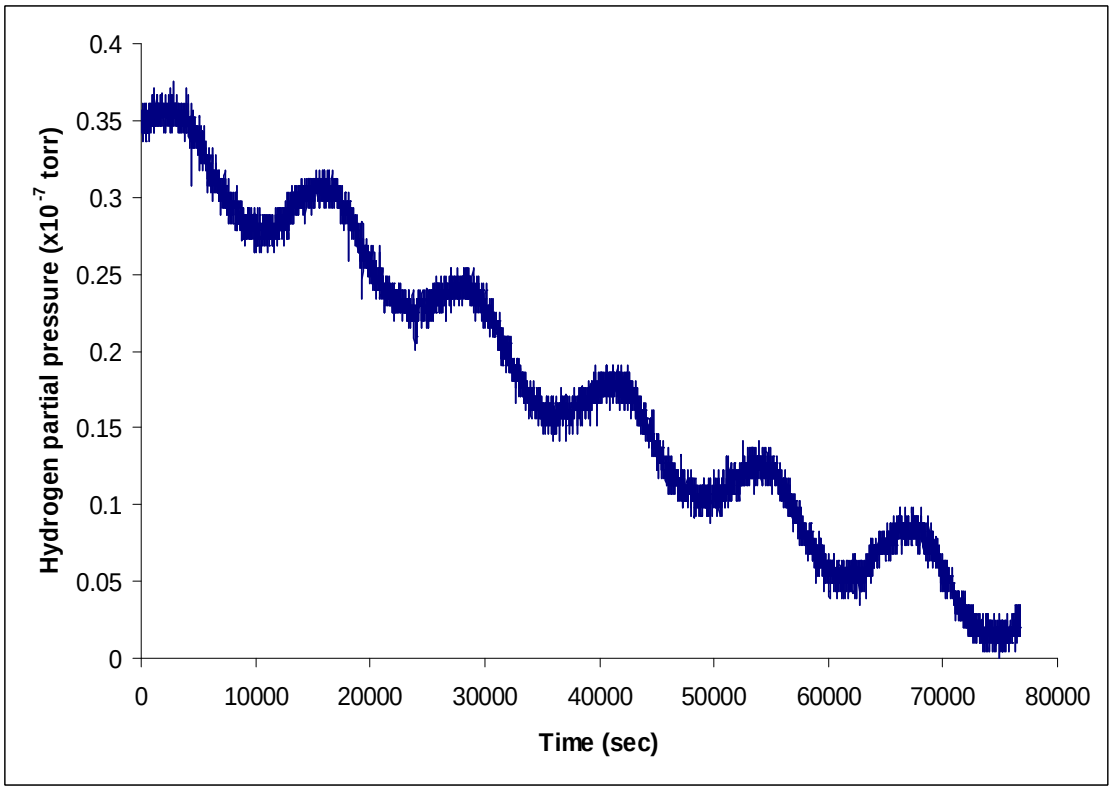

Figure 5-3: The response in hydrogen partial pressure for the potential shown in Figure 5-1.

As can be seen from Figure 5-3, whereas the pressure oscillations can clearly be seen, there is a general long-term downward drift in the mean hydrogen partial pressure. This drift could be attributed to hydrogen gas being absorbed (of diffusing) through the stainless steel walls of the chamber as the experiments ran for a considerable length of time. The drift generally disappeared eventually in cases where it existed and anyway can be removed prior to processing the partial pressure results of the permeated hydrogen into the vacuum system. Figure 5-4 shows how this drift was removed using a linear regression to obtain a fit to the pressure data and subtracting the fitted line from each experimental value. The drift-free values of the pressure are shown in Figure 5-5. Figures 5-6 to 5-8 show, respectively, the signal averaged, time modulated data for the potential, current and partial pressure, from which the Fourier Coefficients were derived.

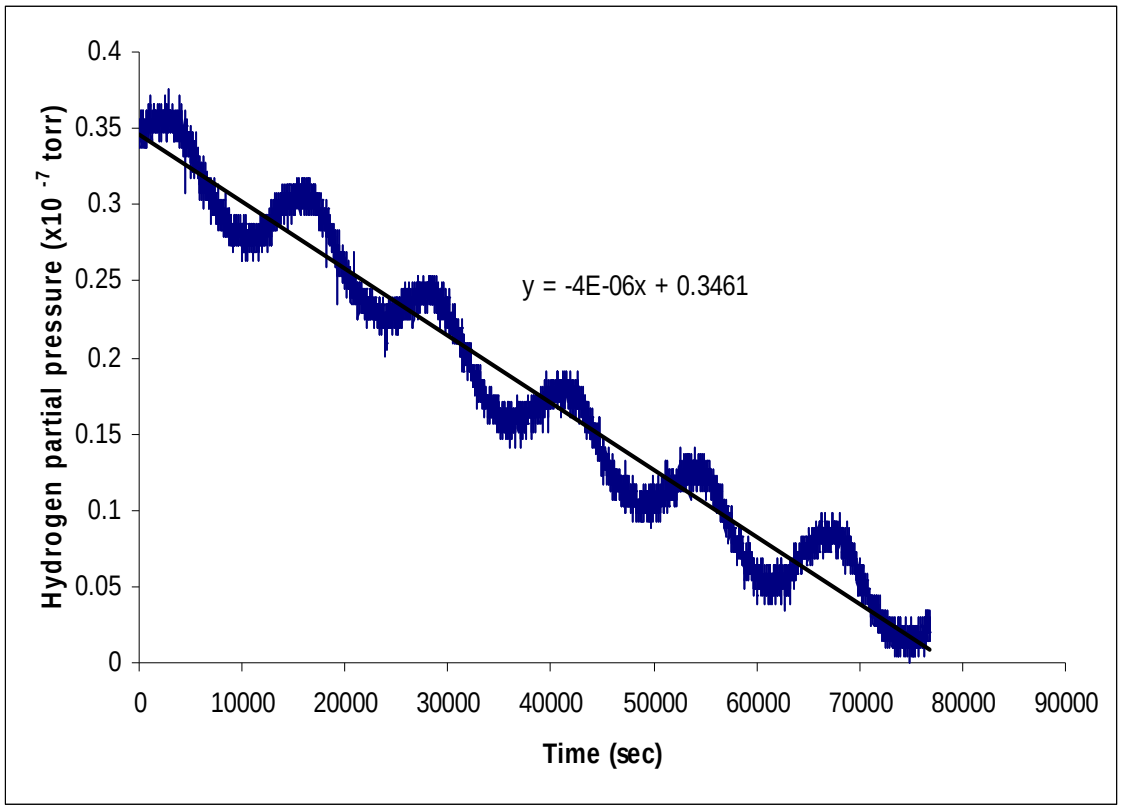

Figure 5-4: Removing the drift from the hydrogen partial pressure readings.

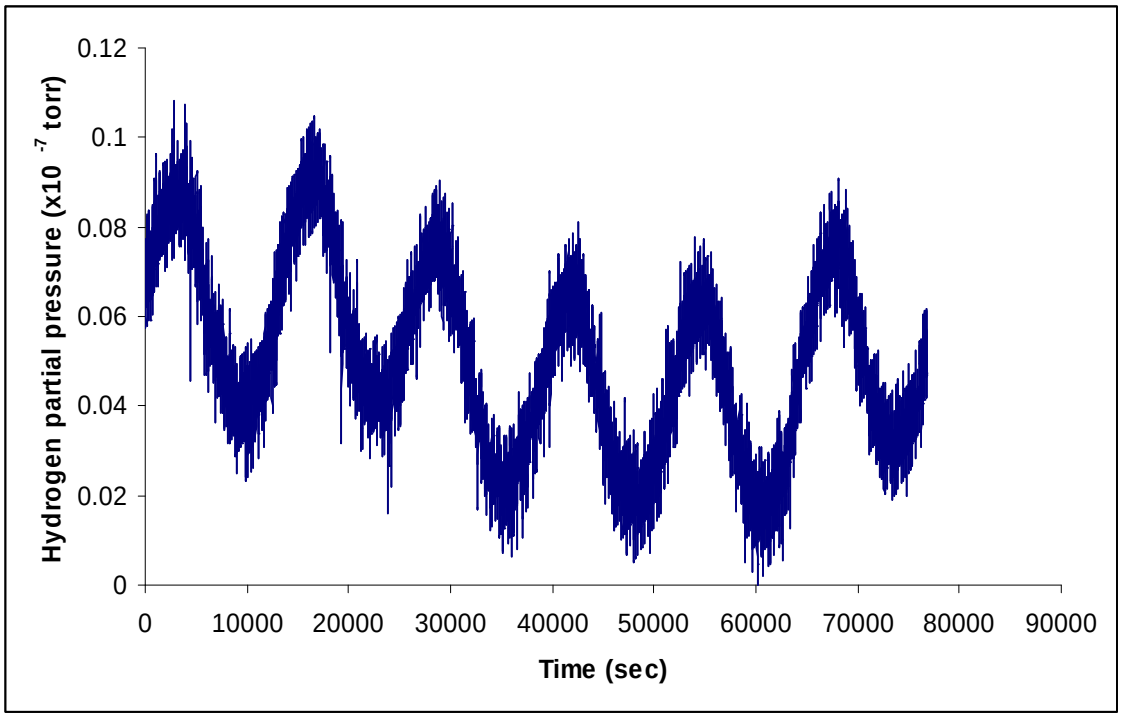

Figure 5-5: Hydrogen partial pressure readings shown in Figure 5-3 free of drift and ready for signal averaging.

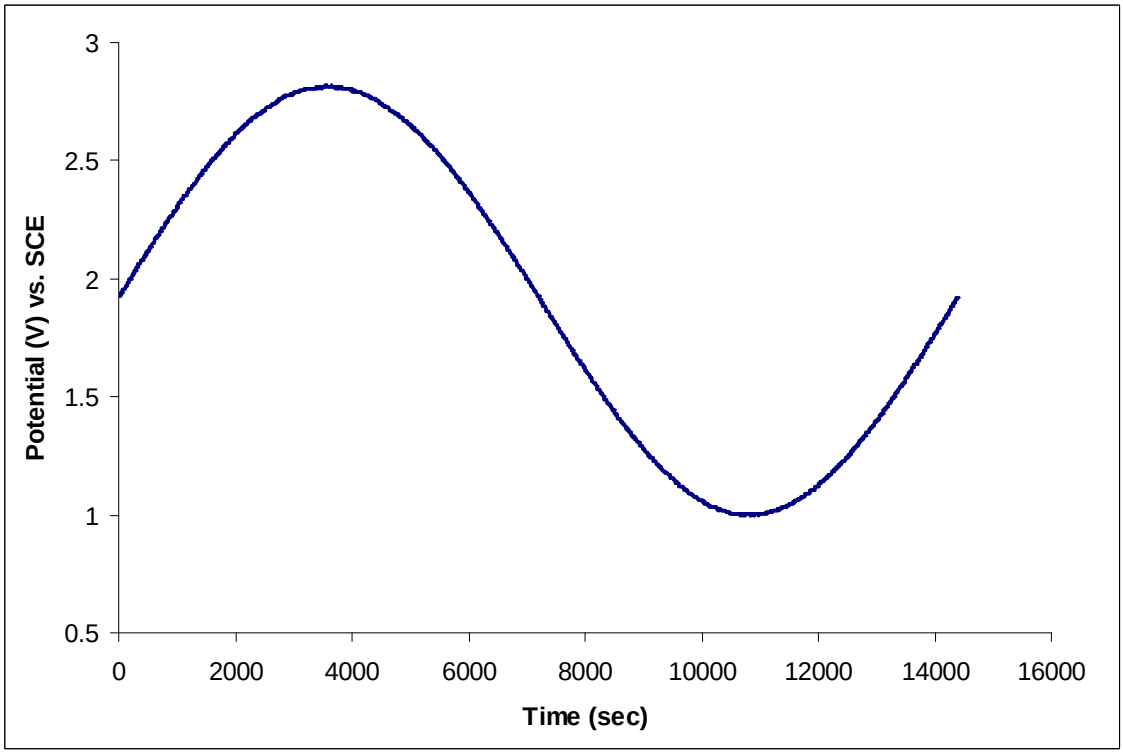

Figure 5-6: Signal-averaged potential from Figure 5-1.

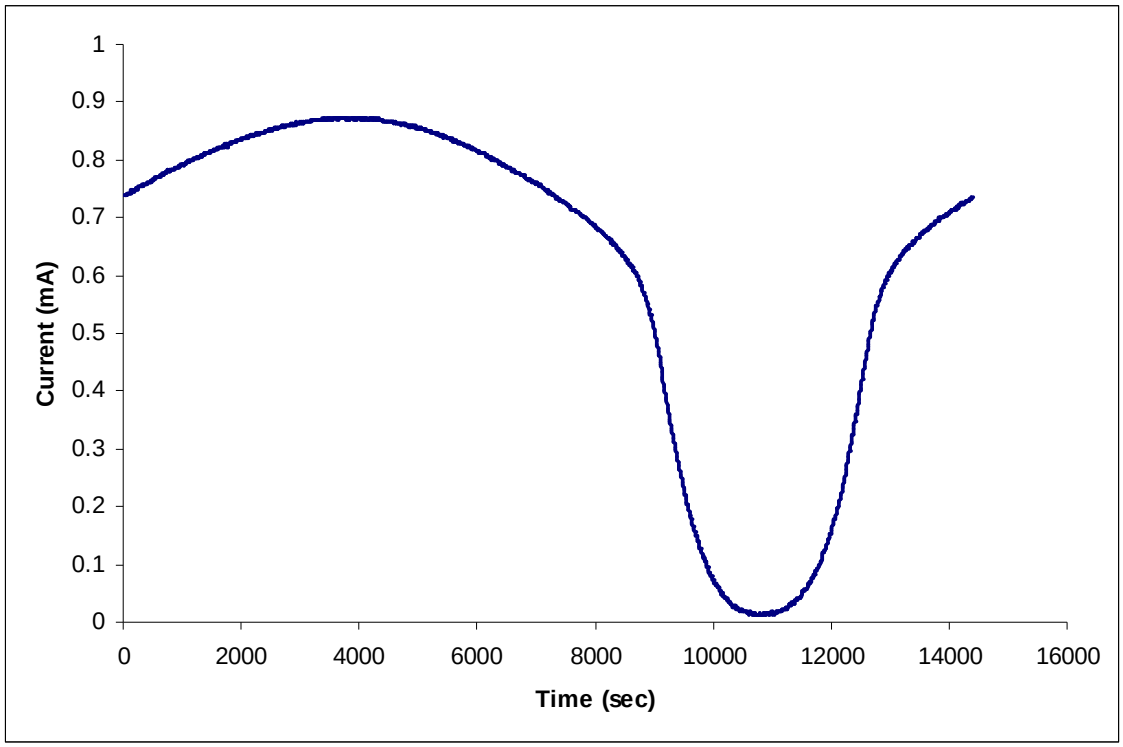

Figure 5-7: Signal-averaged current from Figure 5-2.

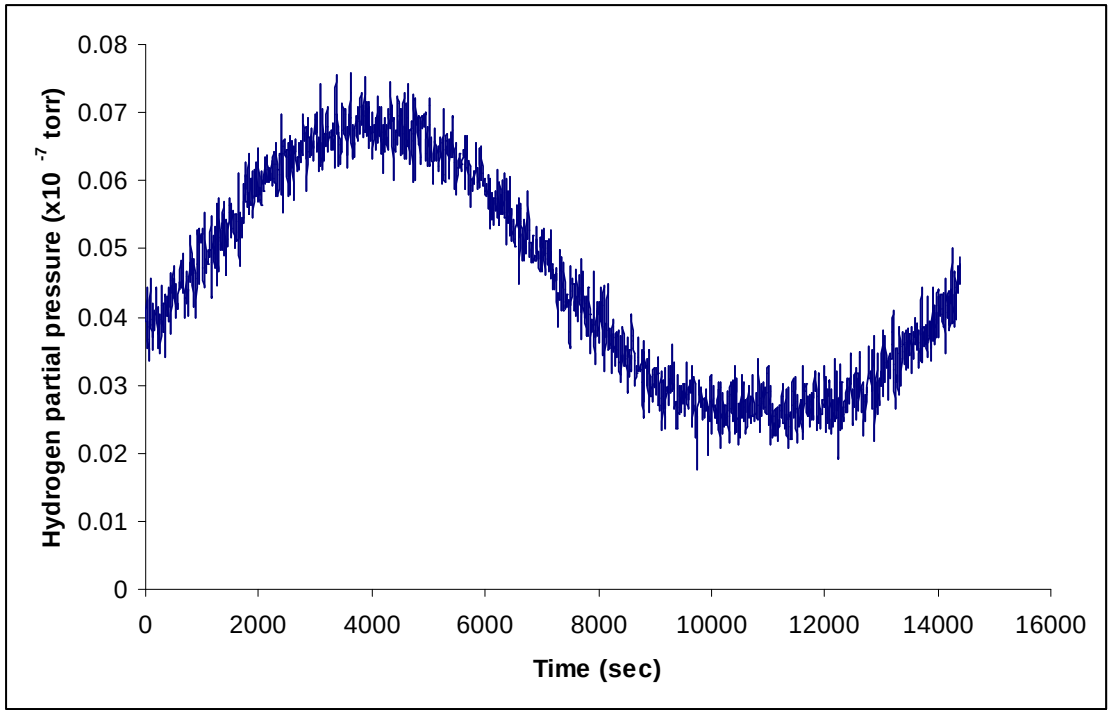

Figure 5-8: Signal-averaged partial pressure from Figure 5-5.

5.1.2 *Potential, Current and Hydrogen Partial Pressure at 1×10^{-4} Hz*

Figures 5-9 to 5-16 show the equivalent results to Figures 5-1 to 5-8, for the frequency of 1×10^{-4} Hz. Apart from the slightly higher frequency, it can be seen that the results are of similar quality to these obtained at 7×10^{-5} Hz with a sinusoidal response still being clearly observed in the output pressure.

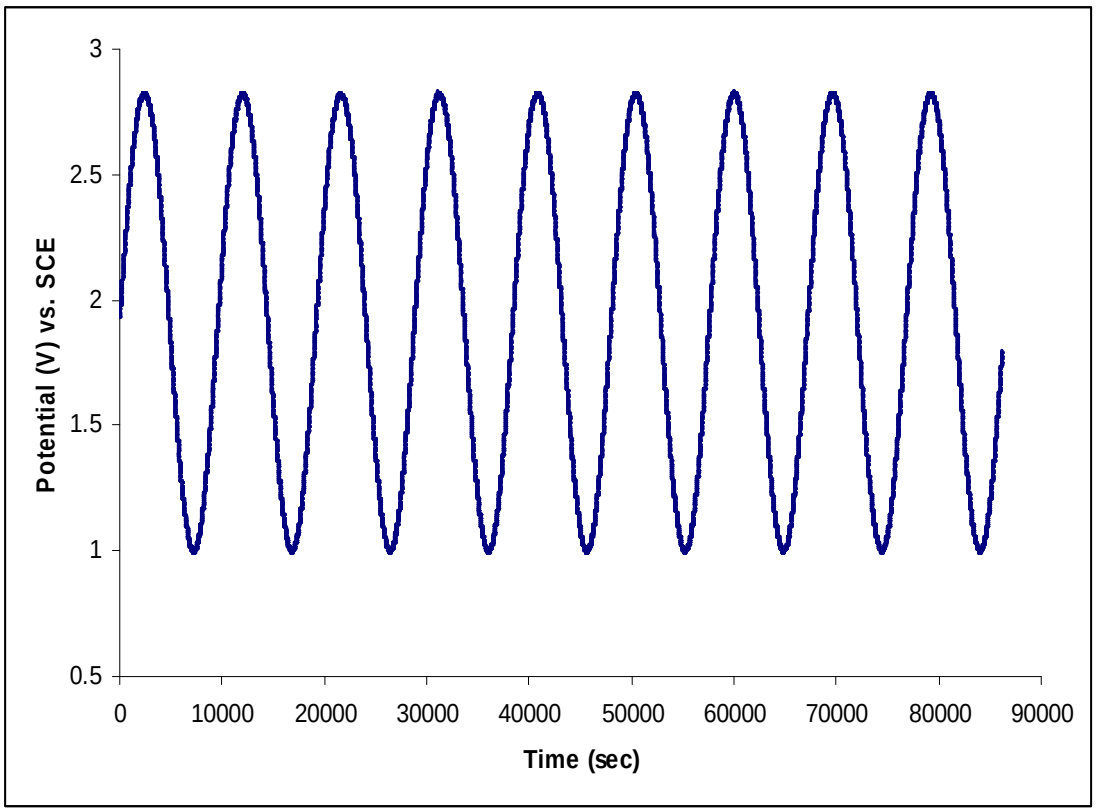

Figure 5-9: Electrical potential applied as a sine wave for nickel at 1×10^{-4} Hz and 22ºC.

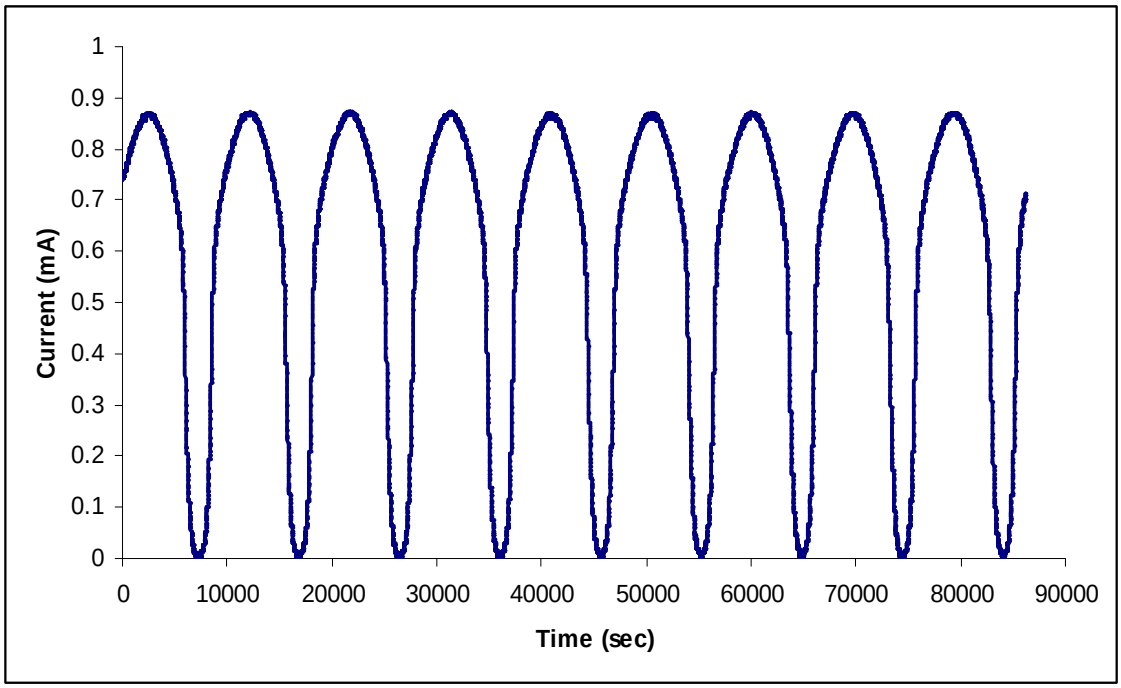

Figure 5-10: Corresponding current for the potential shown in Figure 5-9.

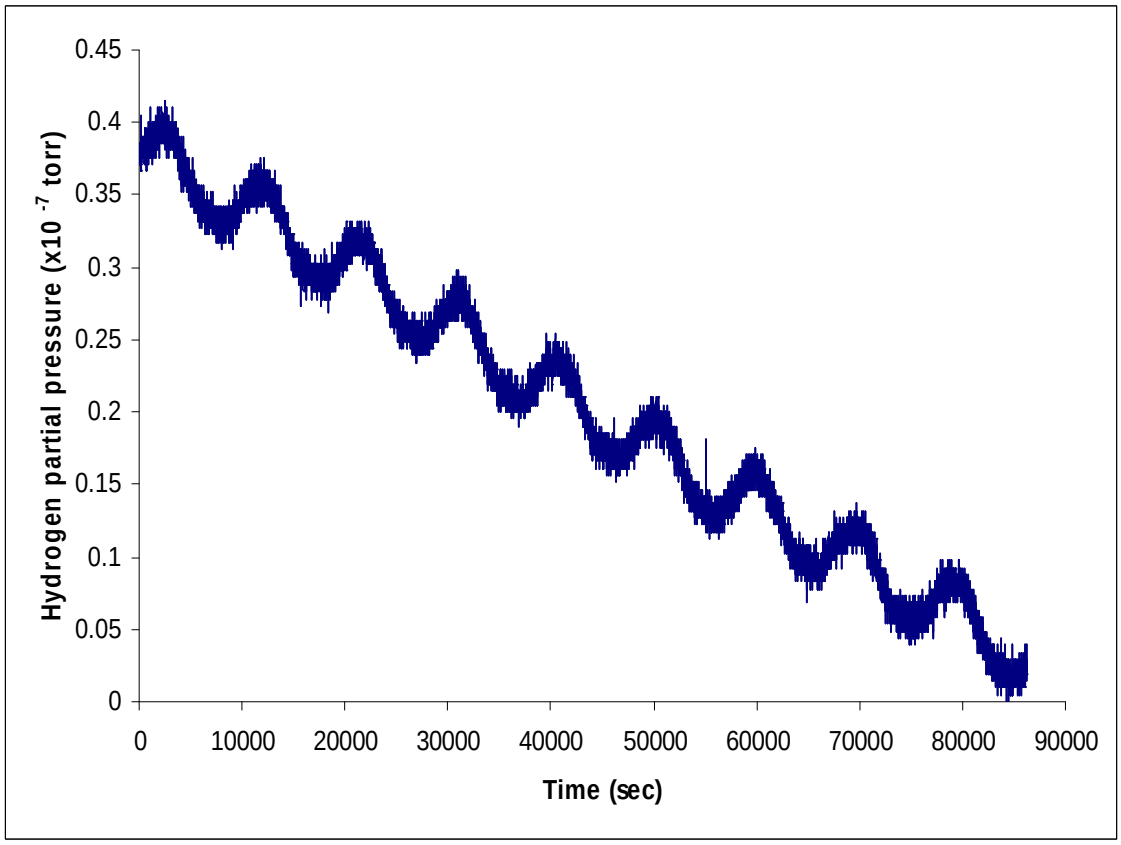

Figure 5-11: The response in hydrogen partial pressure for the potential shown in Figure 5-9.

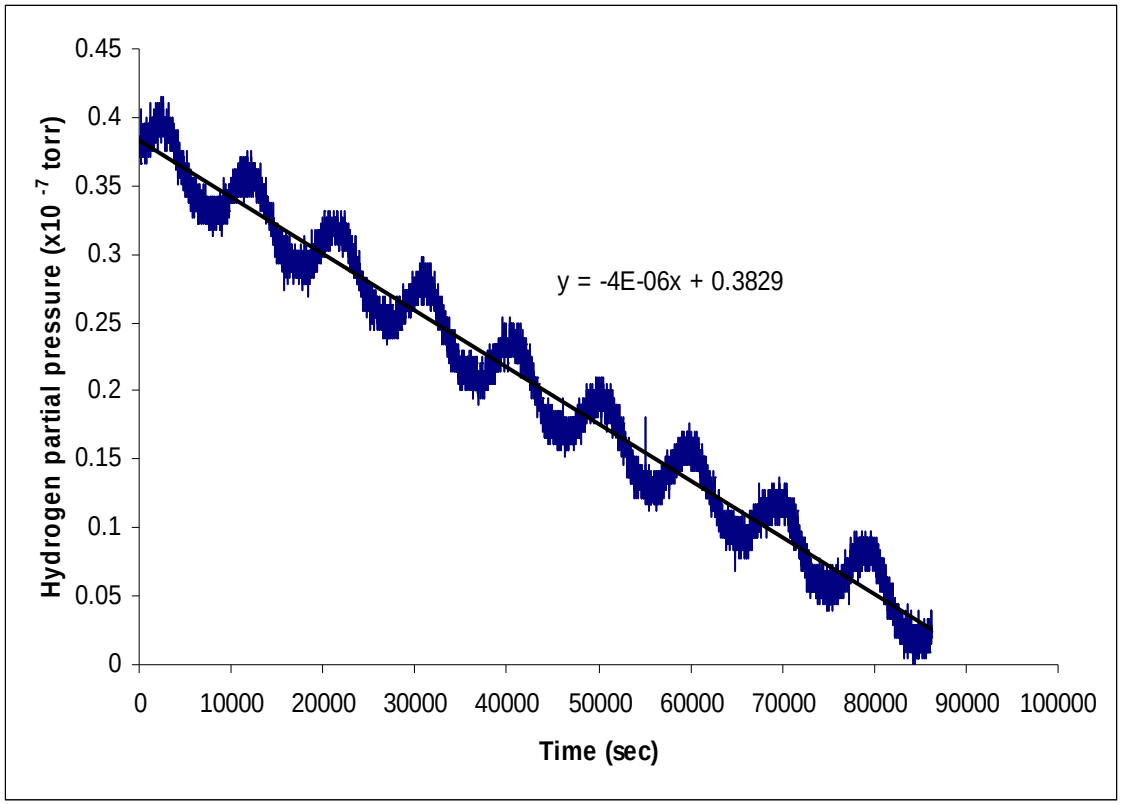

Figure 5-12: Removing the drift from the partial pressure data.

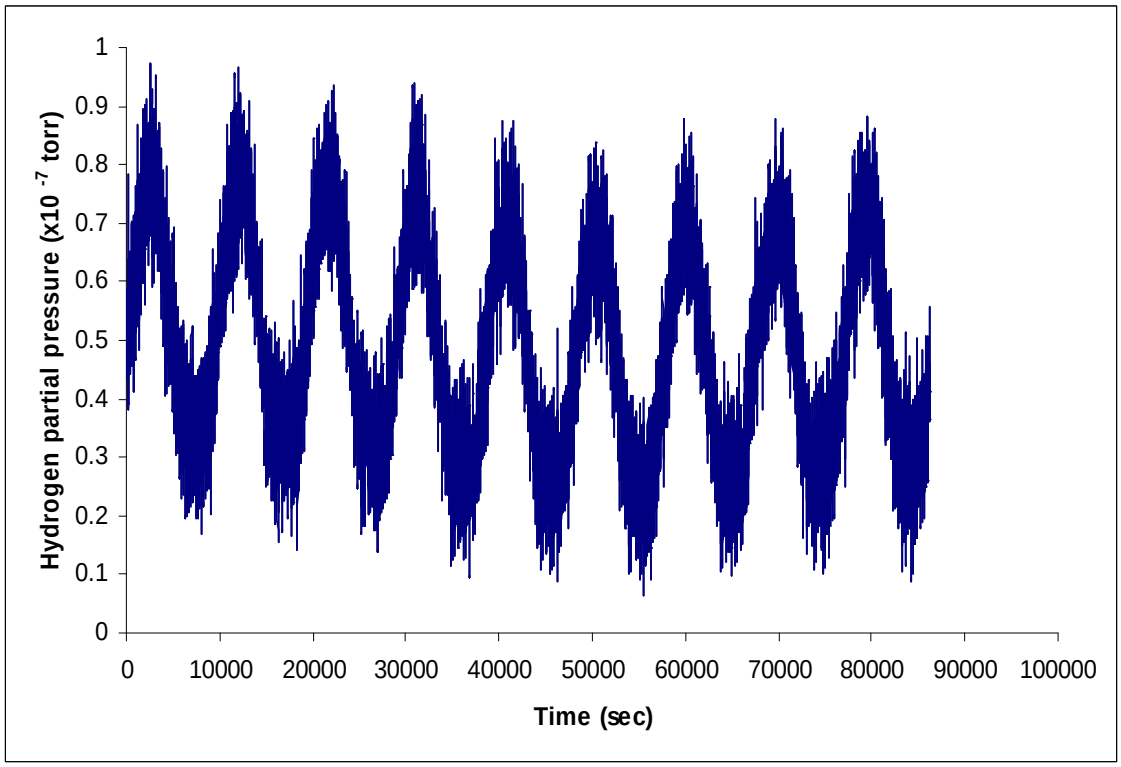

Figure 5-13: Hydrogen partial pressure readings shown in Figure 5-11 free of drift and ready for signal averaging.

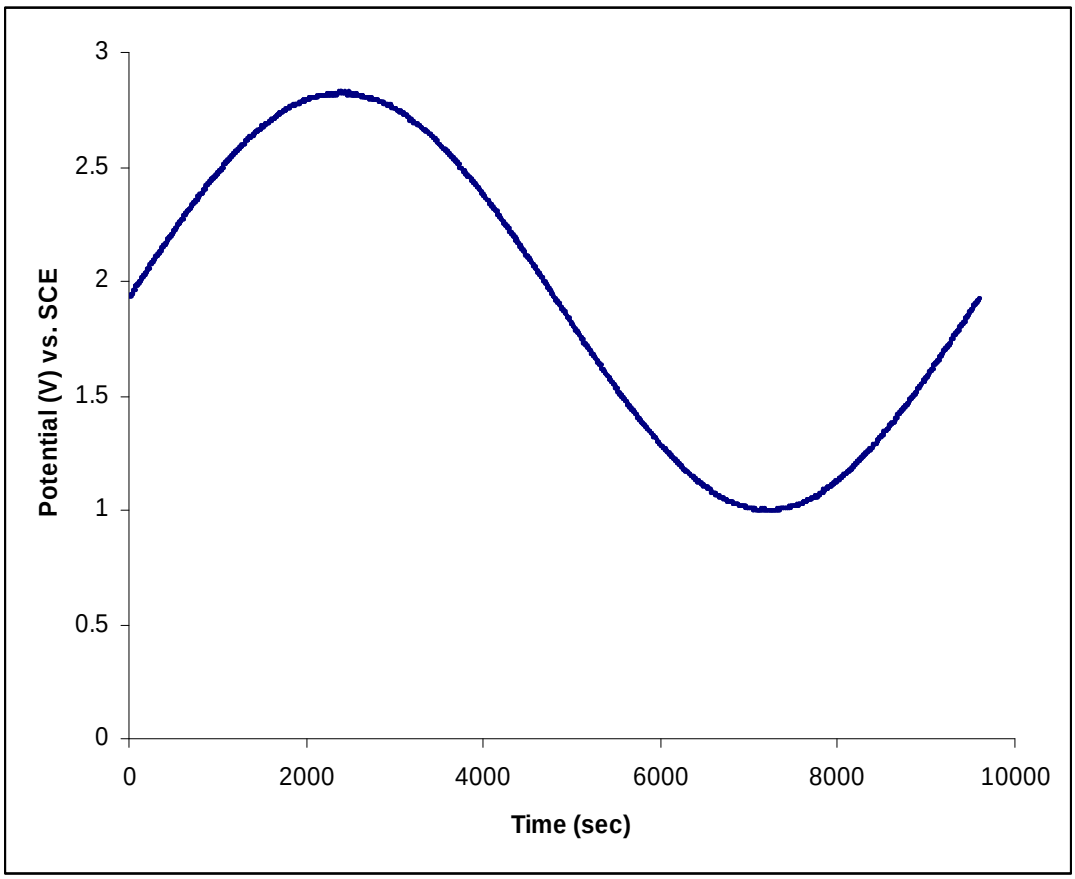

Figure 5-14: Signal-averaged potential from Figure 5-9.

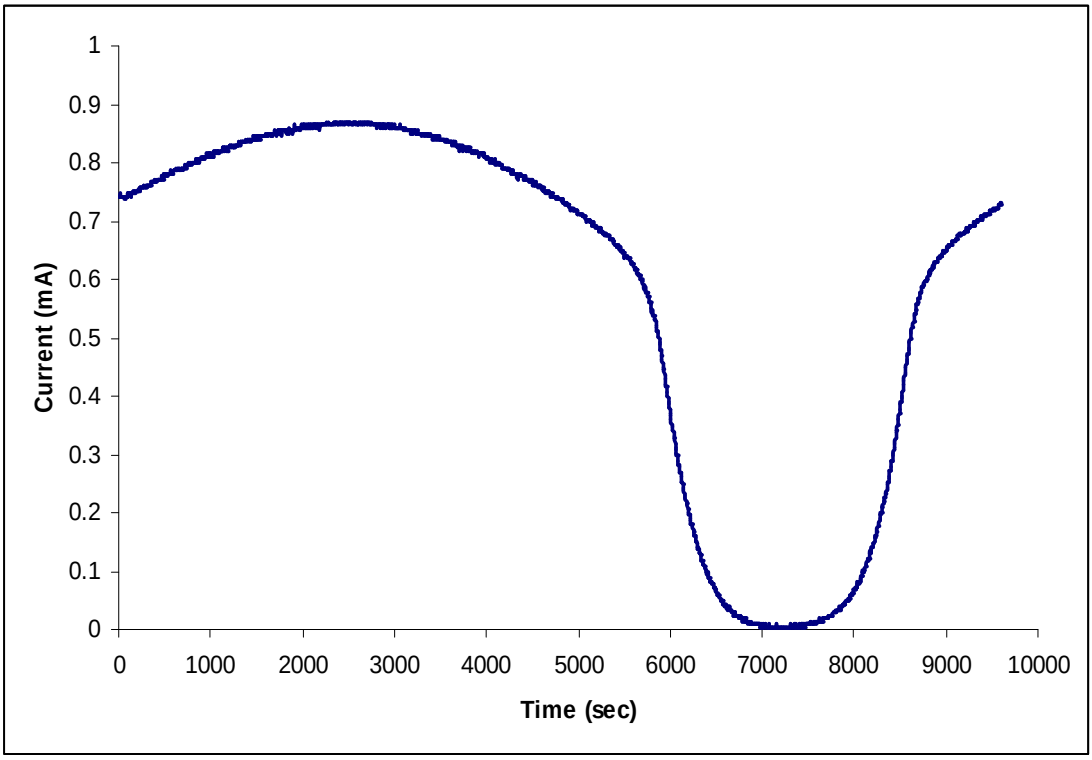

Figure 5-15: Signal-averaged current from Figure 5-10.

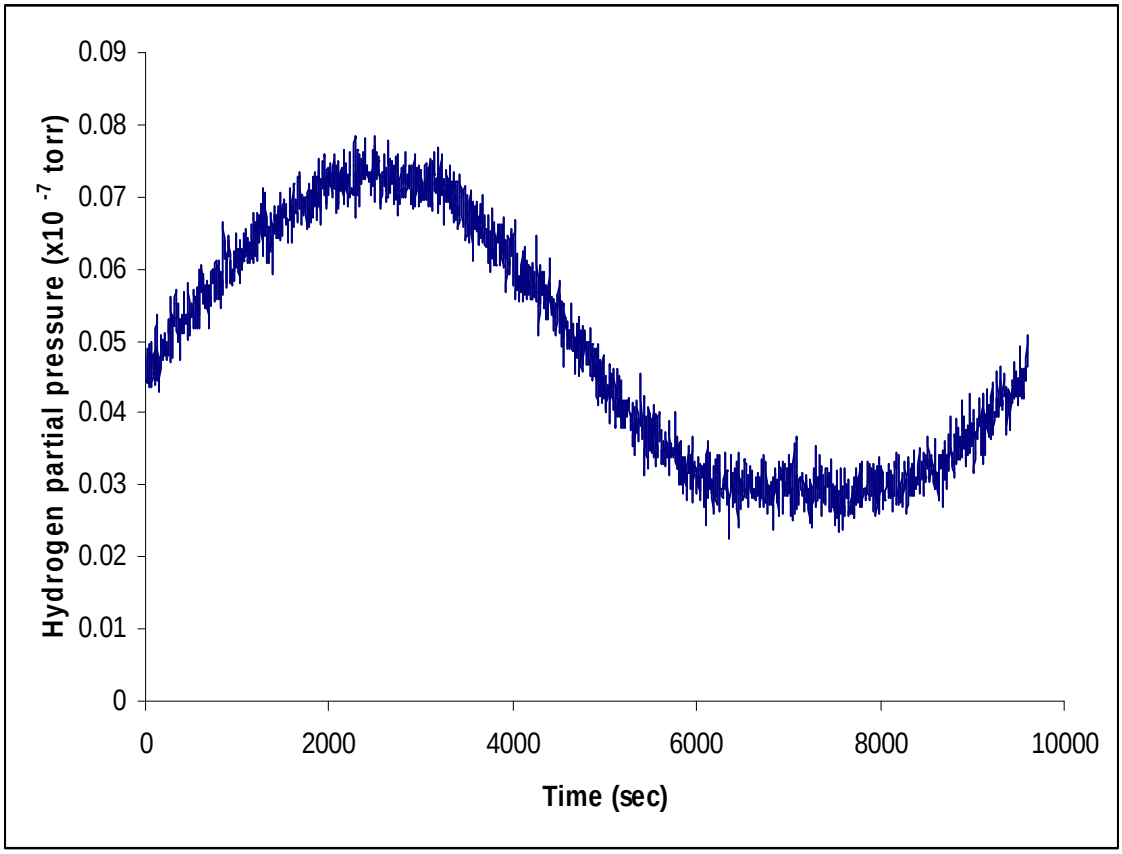

Figure 5-16: Signal-averaged partial pressure from Figure 5-13.

5.1.3 Phase Lag Calculations

The phase lag results after removal of the pumping phase lag (as explained in chapter four, equation 4-37)) are plotted against the applied frequency ω as shown below in Figure 5-17.

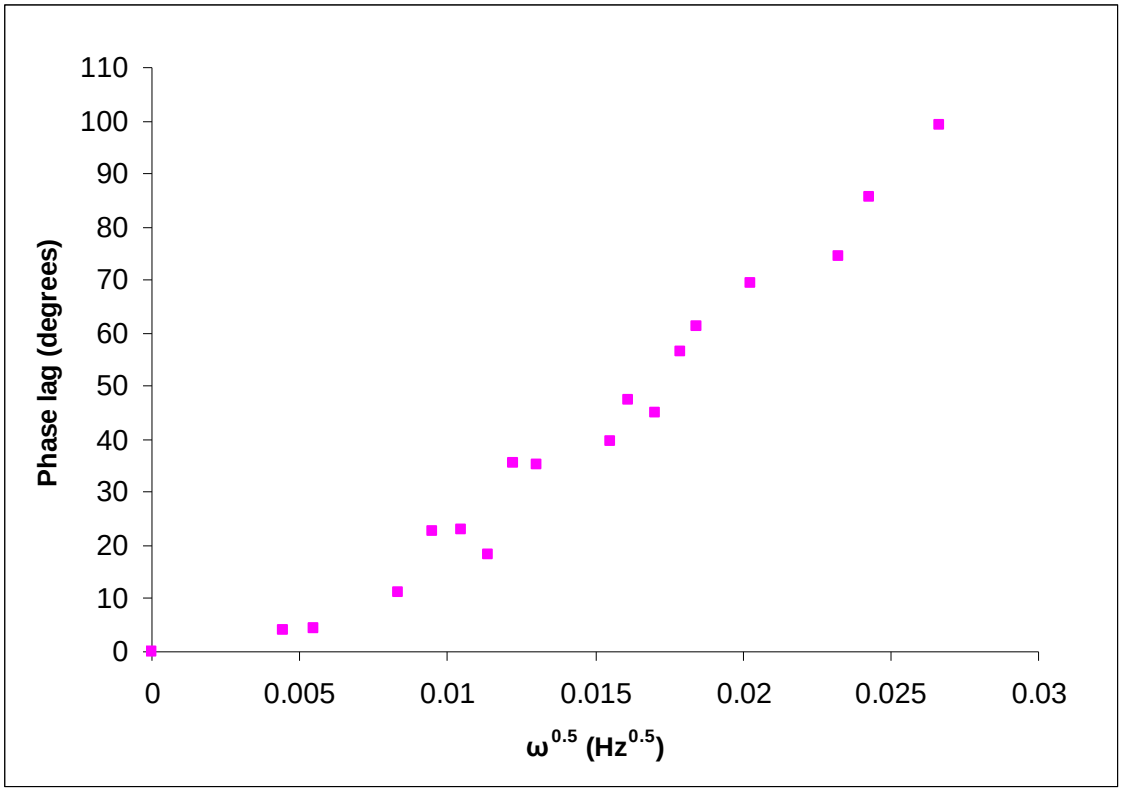

Figure 5-17: Phase lag results from the experiments on 99% Ni at 22ºC.

The phase lag was fitted to the following equation, derived and presented in chapter four, which shows the functional relationship between the phase lag between the input (potential) and the output (hydrogen partial pressure) and frequency. The fit involved using a least-squares algorithm to obtain the best value of the diffusion coefficient D (m^2/s).

$$\varphi = \arctan\left[\frac{\tanh kl - \tan kl}{\tanh kl + \tan kl}\right] \tag{5-2}$$

where k is given by: $k = \sqrt{\frac{\omega}{2D}}$, ω is the applied frequency (Hz) and l is the thickness of the specimen (m).

Figure 5-18 shows the results of the phase lag fitted into equation (5-2) from which the diffusion coefficient was determined as $D = (3.3 \pm 0.55)\times10^{-14}$ m^2/s.

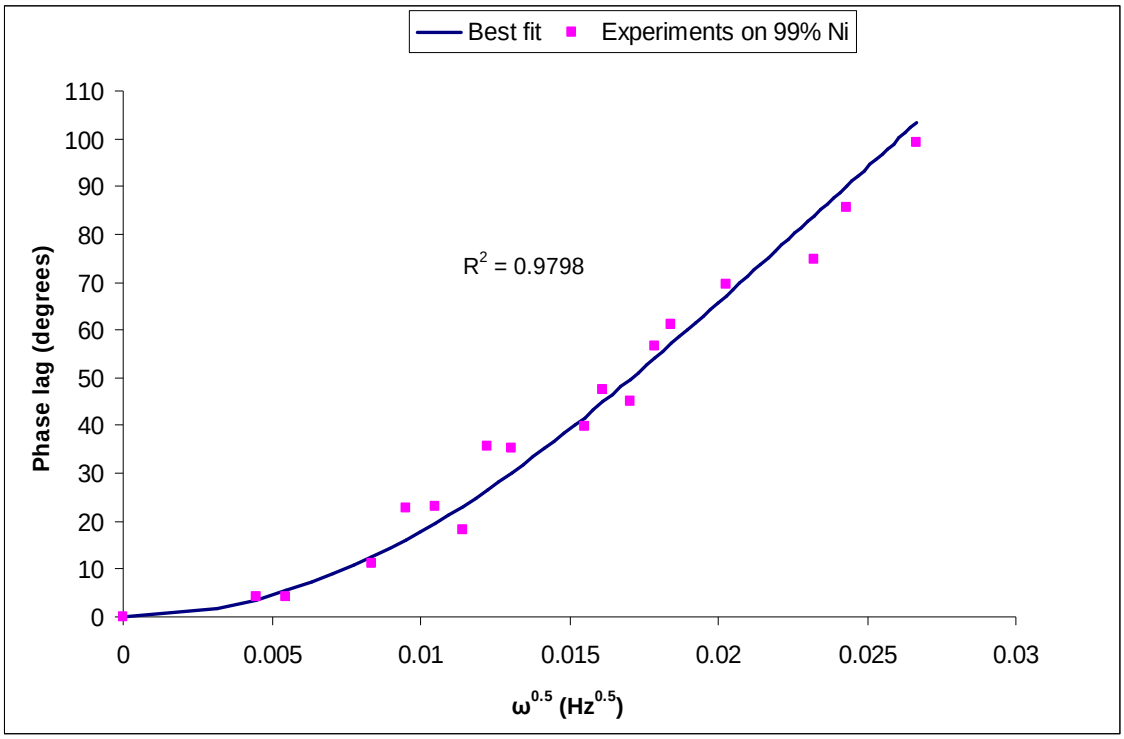

Figure 5-18: The phase lag results fitted to equation (5-2).

5.1.4 Amplitude Ratio Calculations

Values of amplitude ratio (the current to the hydrogen partial pressure) are shown in Figure 5-19.

Equation (5-3), which is a combination of equations (4-34) and (4-36) as explained in detail in chapter four, gives the relationship between the amplitude ratio (ratio of input and output pressures) and frequency where the variable parameters are the hydrogen solubility coefficient, K (mol H_2/m^3 mbar$^{0.5}$) and the diffusion coefficient D (m^2/sec). The frequency is contained in the parameter kl defined earlier; all parameters in equation (5-3) have been defined earlier.

$$\Lambda = \frac{K}{2\sqrt{p_{ss}}} \frac{ART}{V\sqrt{\omega^2+\beta^2}} \frac{\sqrt{2}Dk}{\sqrt{\sinh^2 kl + \sin^2 kl}} \tag{5-3}$$

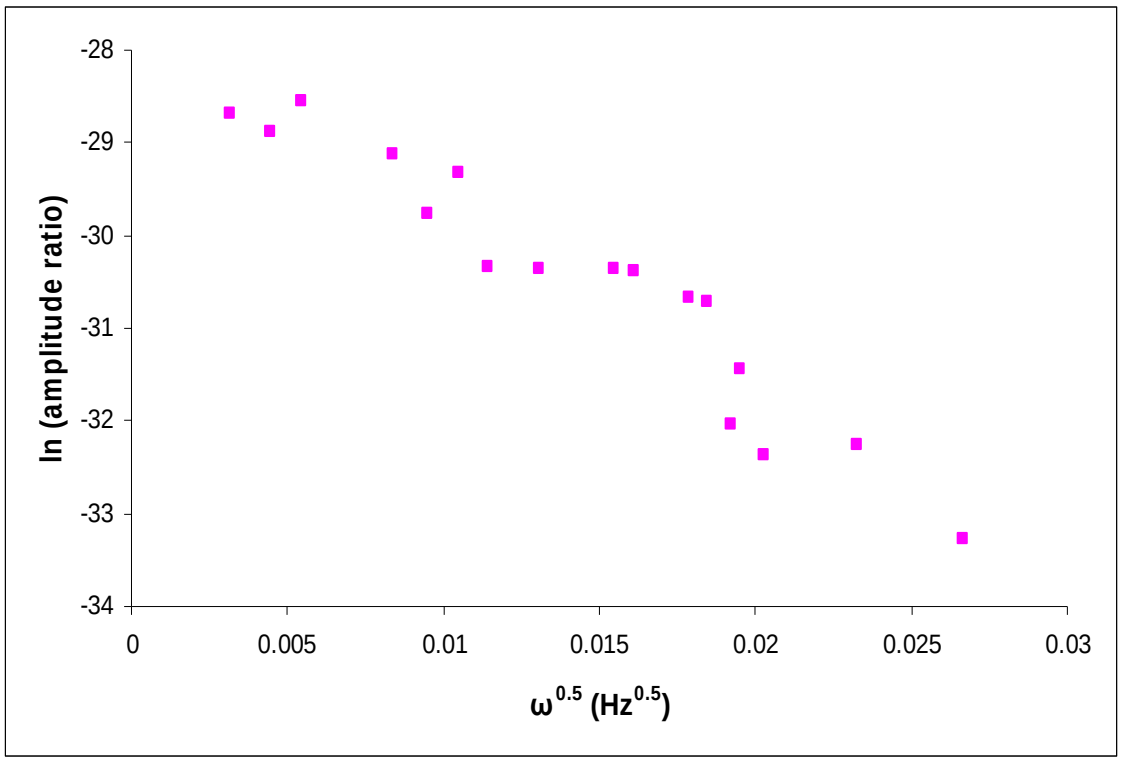

Figure 5-19: Amplitude ratio results from the experiments on 99% Ni at 22°C.

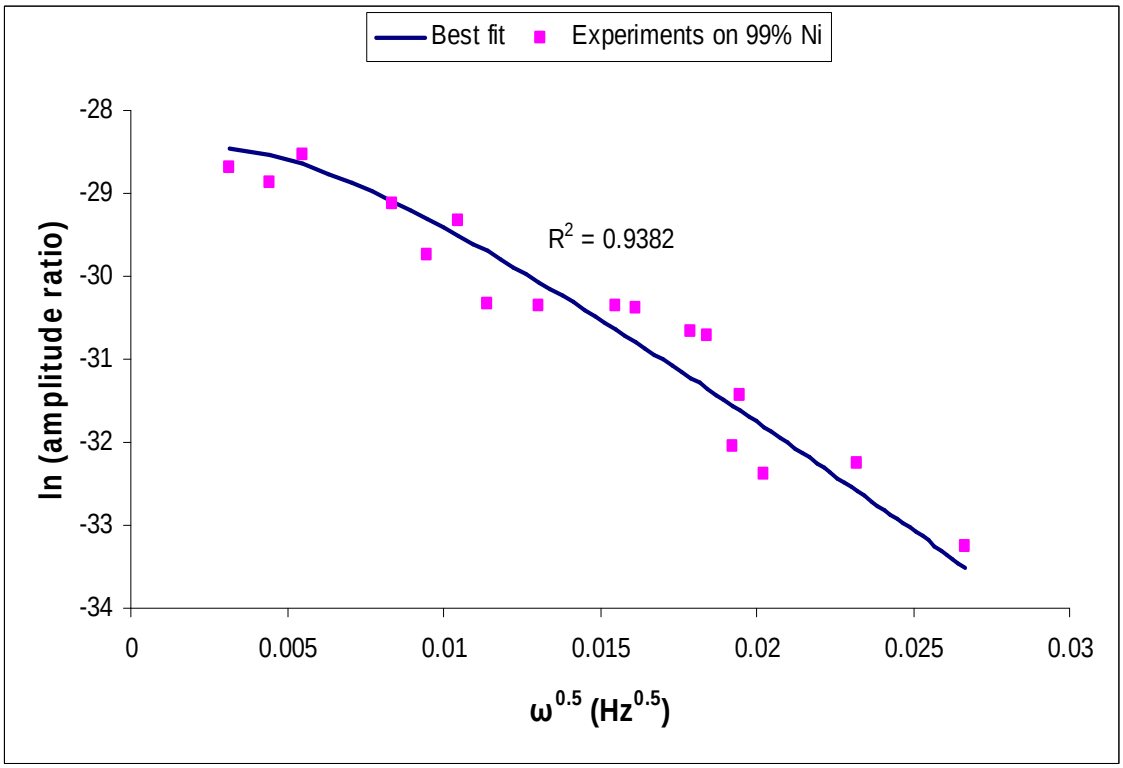

Figure 5-20: Amplitude ratio results fitted into amplitude ratio equations.

Independently fitting for K and D results in a value of $(2.07\pm0.1)\times10^{-2}$ (mol H_2/m^3 $mbar^{0.5}$) for K, the hydrogen solubility coefficient, and a value of $(3.9\pm0.45)\times10^{-14}$ m^2/s for D, the diffusion coefficient with $R^2 = 0.9382$. When using the value of D derived from the phase lag plot to fit for K only (using equation (5-3)), the value of K was $(2.16\pm0.08)\times10^{-2}$ (mol H_2/m^3 $mbar^{0.5}$) with $R^2 = 0.9516$.

The diffusion coefficient value derived from fitting the amplitude ratio results shows a high consistency with the one calculated from the phase lag results shown in the previous subsection.

5.2 Permeation Experiments on Nickel at 60ºC

Another set of experiments was done on nickel at 60ºC to give further information on the precision of the oscillatory method in finding the diffusion and solubility coefficients of hydrogen in metals.

The cathodic potential was applied in a similar way to the previous experiments and the readings of the controlled potential, measured current and hydrogen partial pressure were recorded and analysed accordingly.

Figure 5-21 shows the variations of the phase lag with the square root of applied frequency at both 60ºC and 22ºC. The best fit for the results at 60ºC gave a value of $(1.1\pm0.3)\times10^{-13}$ m^2/sec for the diffusion coefficient, D. It is clear from this graph that the diffusion coefficient in nickel increases with temperature.

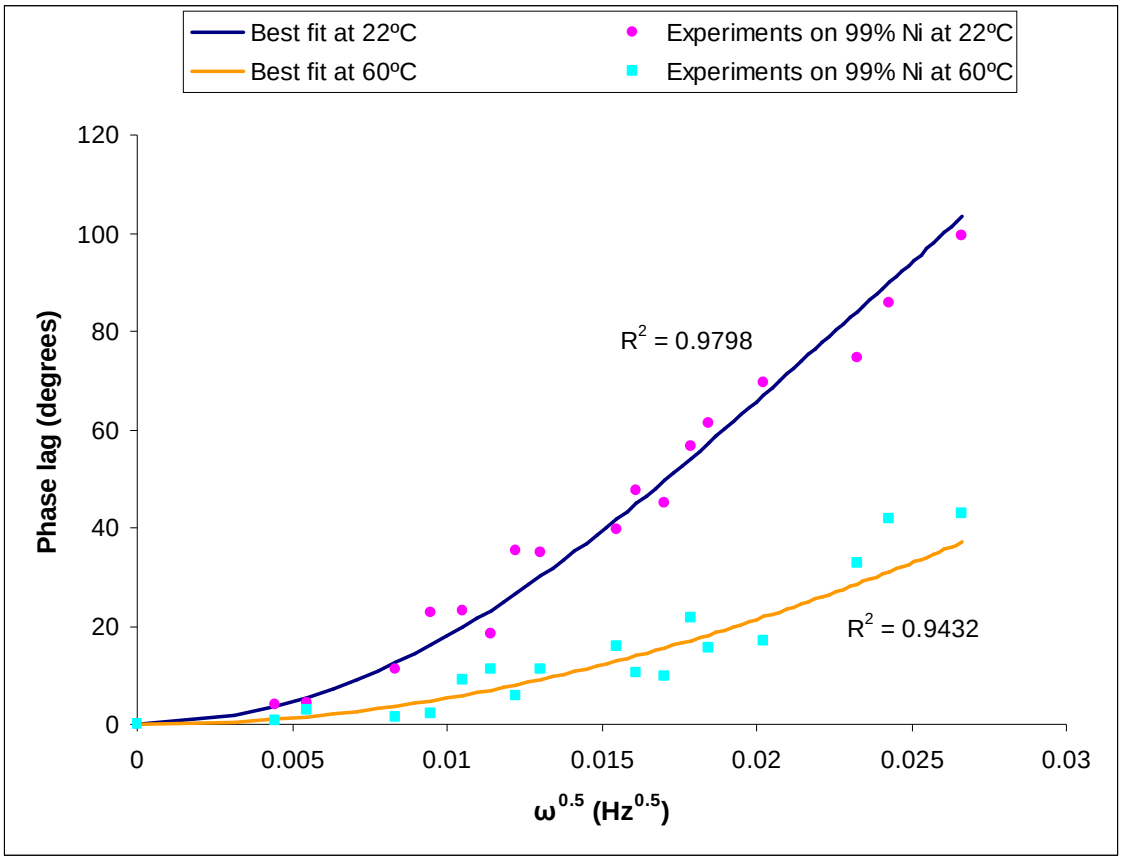

Figure 5-21: Phase lag results at 60ºC compared with the results at 22ºC.

Fitting the results of amplitude ratio into the amplitude ratio vs. frequency relationship, gives a value of $(3.05\pm0.25)\times10^{-2}$ (mol H_2/m^3 $mbar^{0.5}$) for the hydrogen solubility, K, and a value of $(2.5\pm0.28)\times10^{-13}$ m^2/s for the diffusion coefficient, D with $R^2 = 0.9208$. Again, by using the value of D derived from the phase lag plot, K was found, by the fit to equation (5-3), to be $(3.34\pm0.12)\times10^{-2}$ (mol H_2/m^3 $mbar^{0.5}$) with $R^2 = 0.9476$.

Figure 5-22 shows that the amplitude ratio increases with temperature.

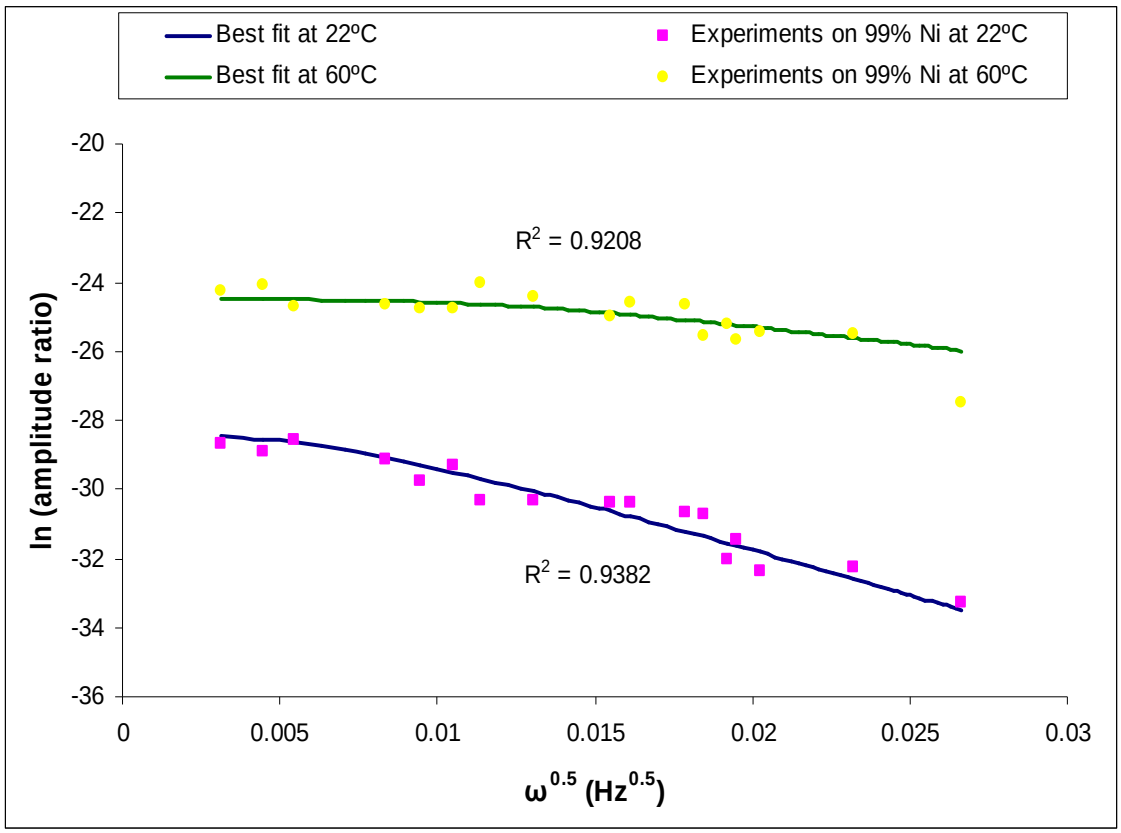

Figure 5-22: Amplitude ratio results at 60ºC compared with the results at 22ºC.

Knowing the uncertainty in the diffusion coefficient values from the above fitting at both 22ºC and 60ºC enables an assessment of the uncertainty in the activation energy by plotting the logarithm of diffusion coefficient against the reciprocal of temperature and assuming that the Arrhenius equation describes correctly the variation with temperature:

$$D = D_0 \exp\left(-\frac{Q}{RT}\right) \tag{5-4}$$

where D_0 is the pre-exponential diffusion coefficient factor (m^2/s) and Q is the activation energy (J/mol), R is the universal gas constant (8.314 J/mol.K) and T is the absolute temperature (K).

Figures 5-23 and 5-24 show Arrhenius plots for the diffusion coefficients derived from the phase and amplitude plots along with their respective uncertainties, and illustrate how the maximum and minimum activation energies were determined.

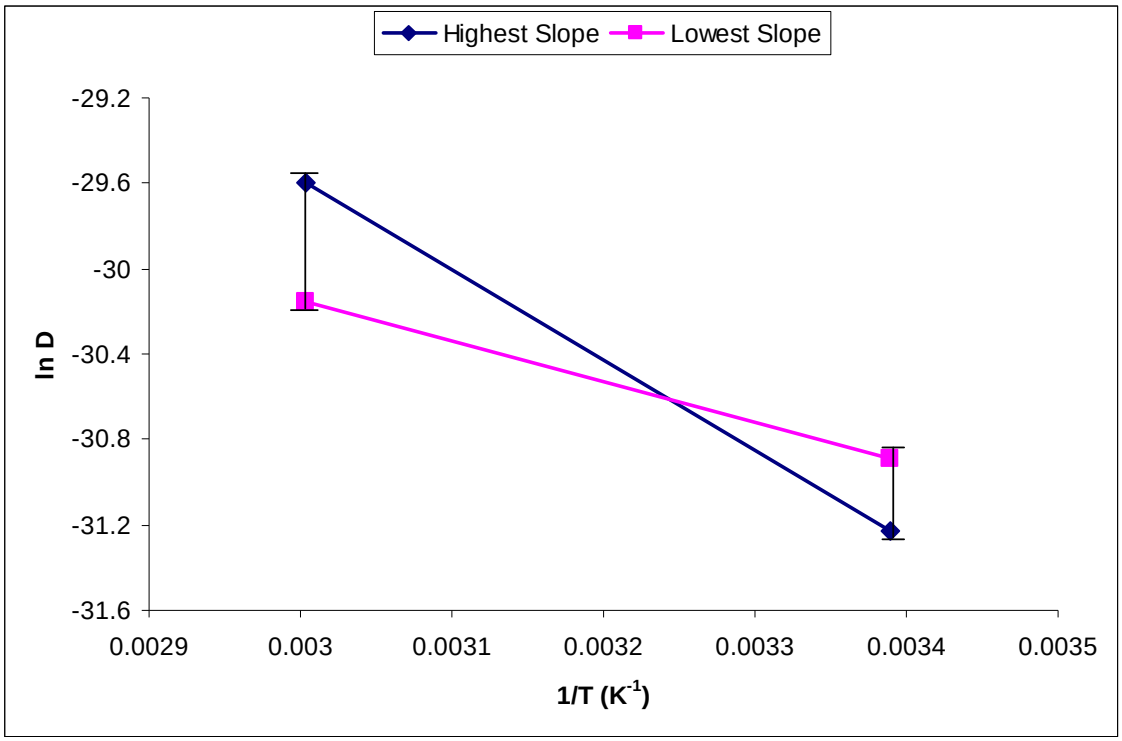

Figure 5-23: Arrhenius plot for (ln *D*) vs. reciprocal of temperature for nickel data at 22ºC and 60ºC (highest and lowest slopes shown); *D* values derived from phase lag fit.

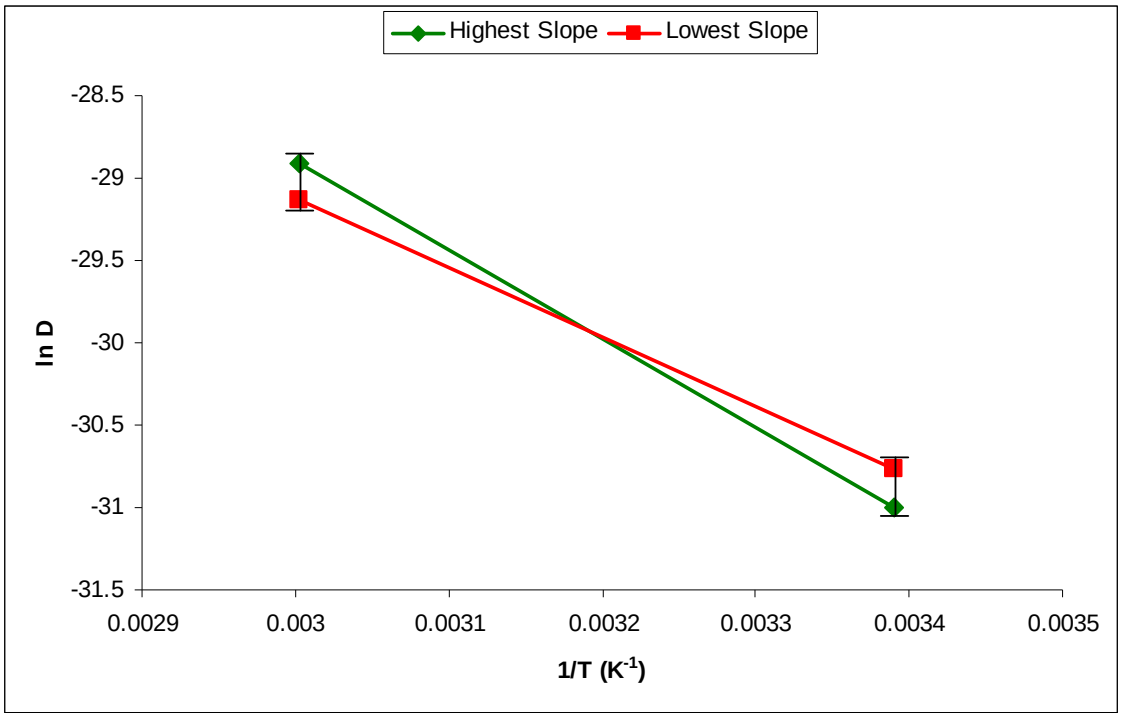

Figure 5-24: Arrhenius plot for (ln *D*) vs. reciprocal of temperature for nickel data at 22ºC and 60ºC (highest and lowest slopes shown); *D* values derived from amplitude ratio fit.

***D* derived from**	***D* (m^2/s), 22ºC**	***D* (m^2/s), 60ºC**	***D_0* (m^2/s)**	***Q* (J/mol)**
Phase lag fit	$(3.3\pm0.55)\times10^{-14}$	$(1.1\pm0.30)\times10^{-13}$	Max. 4.3×10^{-8} Min. 2.3×10^{-11}	Max. 34980 Min. 15720
Amplitude ratio fit	$(3.9\pm0.45)\times10^{-14}$	$(2.5\pm0.28)\times10^{-13}$	Max. 3×10^{-6} Min. 7×10^{-8}	Max. 44850 Min. 35030

Table 5-1: Activation energy and pre-exponential diffusion coefficient factor for nickel from the experiments at 22ºC and 60ºC for values of *D* derived from fitting to both phase lag and amplitude ratio plots.

The same calculations as above were carried out for values of solubility coefficient at both 22ºC and 60ºC derived from the fitting to the amplitude ratio plot in the case where *D* and *K* were derived independently and when *K* was derived alone using the value of

D found from the phase lag plots. As before, a fit to an Arrhenius equation was done to derive Q_K and K_0:

$$K = K_0 \exp\left(-\frac{Q_K}{RT}\right) \tag{5-5}$$

where K_0 is the pre-exponential solubility coefficient factor (mol H_2/m^3 $mbar^{0.5}$) and Q_K is the activation energy (J/mol), and *R* and *T* were identified before.

***K* derived**	***K* (mol $H_2/m^3 mbar^{0.5}$), 22ºC**	***K* (mol $H_2/m^3 mbar^{0.5}$), 60ºC**	**K_0 (mol $H_2/m^3 mbar^{0.5}$)**	**Q_K (J/mol)**
Independently	$(2.07\pm0.10)\times10^{-2}$	$(3.05\pm0.25)\times10^{-2}$	Max. 1.58 Min. 0.17	Max. 10760 Min. 5090
Using *D* derived from phase lag plot	$(2.16\pm0.08)\times10^{-2}$	$(3.34\pm0.12)\times10^{-2}$	Max. 1.79 Min. 0.53	Max. 10940 Min. 7800

Table 5-2: Activation energy and pre-exponential solubility coefficient factor for nickel from the experiments at 22ºC and 60ºC.

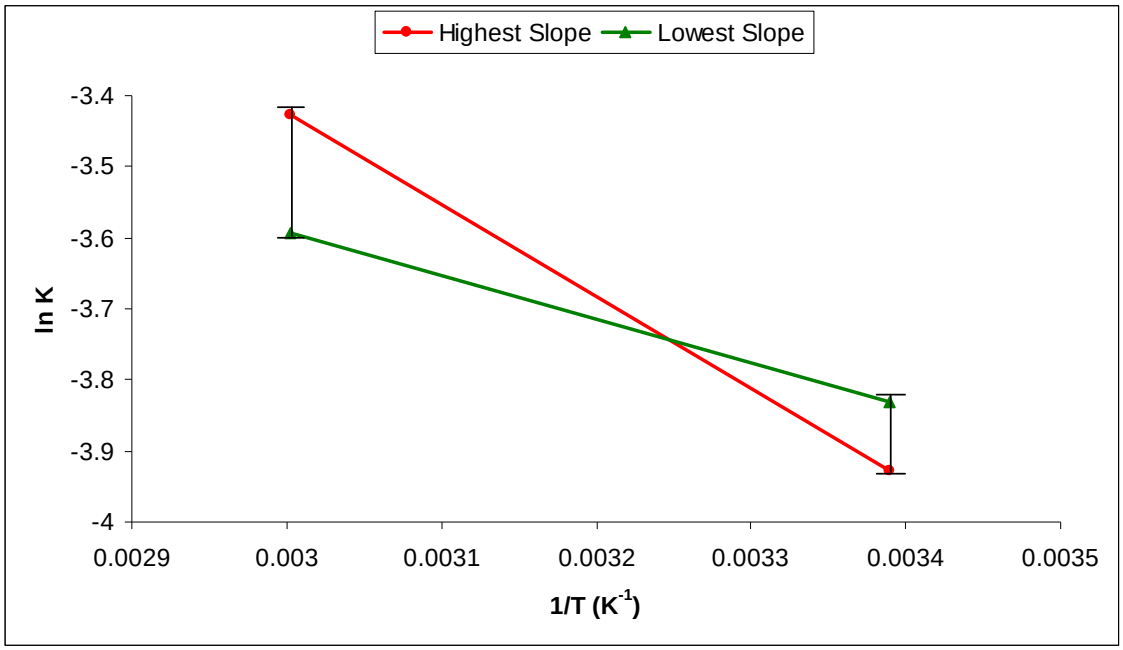

Figure 5-25: Arrhenius plot for (ln *K*) vs. reciprocal of temperature for nickel data at 22ºC and 60ºC (highest and lowest slopes shown); *K* values derived independently.

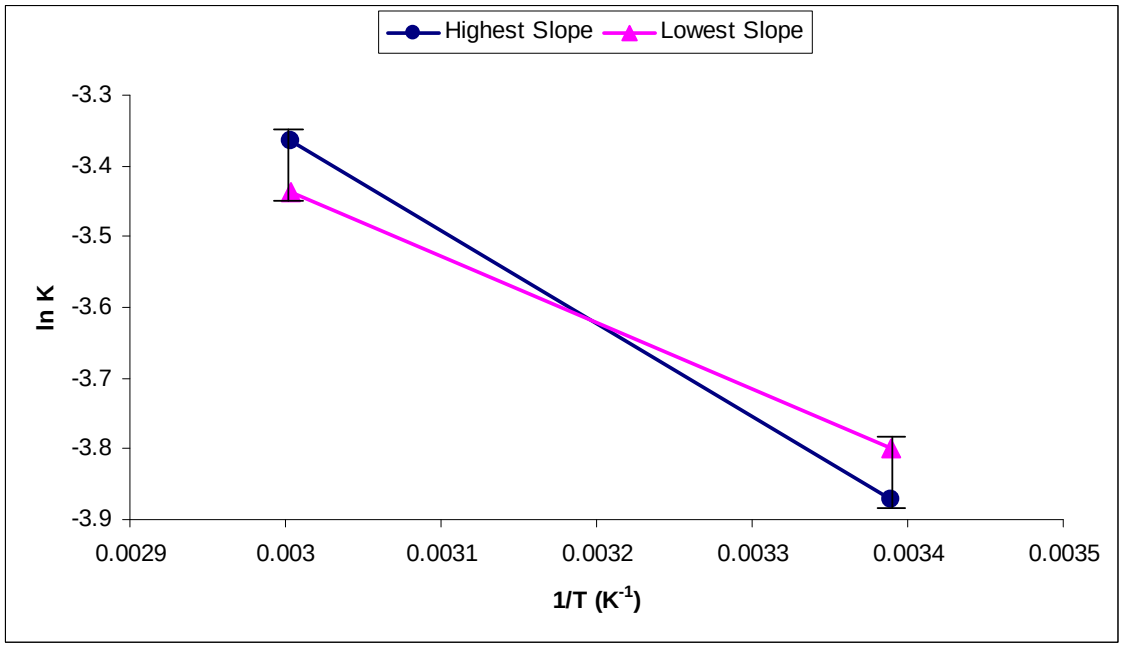

Figure 5-26: Arrhenius plot for (ln *K*) vs. reciprocal of temperature for nickel data at 22ºC and 60ºC (highest and lowest slopes shown); *K* values derived using *D* value derived from phase lag plot.

Chapter 6

Results and Analysis (Low Alloy Steels)

In this chapter, experiments on the heat treatable low alloy steel En24 (equivalent to BS 970 817M40 and approximately equivalent to AISI 4340) are analysed and the results are presented. These experiments were done on specimens in three different heat treatment conditions; annealed, quenched, and quenched followed by tempering at 500°C. The specimens were prepared from a single block of stock material so the chemical composition and inclusion content should be identical. Since the specimens were prepared individually by cutting and grinding of a heat-treated block, the thicknesses varied.

In a similar method to the one shown in the previous chapter, a cathodic potential was applied to the cell containing 0.1N NaOH (sodium hydroxide) and the corresponding electrical current and hydrogen partial pressure were recorded and then analysed.

6.1 Annealed En24

This specimen was a disc of 0.25 mm uniform thickness and 83 mm diameter and, as before, the effective area in contact with the chemical solution was 25.5 cm^2. The Vickers hardness for this specimen was 260±2 HV. The cathodic potential was modulated (with sine wave oscillations) for a set-point between 500 and 2500 mV vs. SCE. As shown in Figure 6-1, the highest peak was a little less than 2500 mV but this is dealt with by using amplitude ratios. The frequencies ranged between 1.3×10^{-5} and 7×10^{-4} Hz, similar to the ones used for the nickel specimen. As before, the potential, current and hydrogen partial pressure readings were recorded at a sampling rate of one reading per 10 seconds for at least 15 cycles for each frequency.

An example of the potential, electrical current and hydrogen partial pressure readings at an applied frequency of 3.47×10^{-5} Hz is given below, Figures 6-1 to 6-3. Signal averaged potential, current and partial pressure curves are shown in Figures 6-4 to 6-6, respectively.

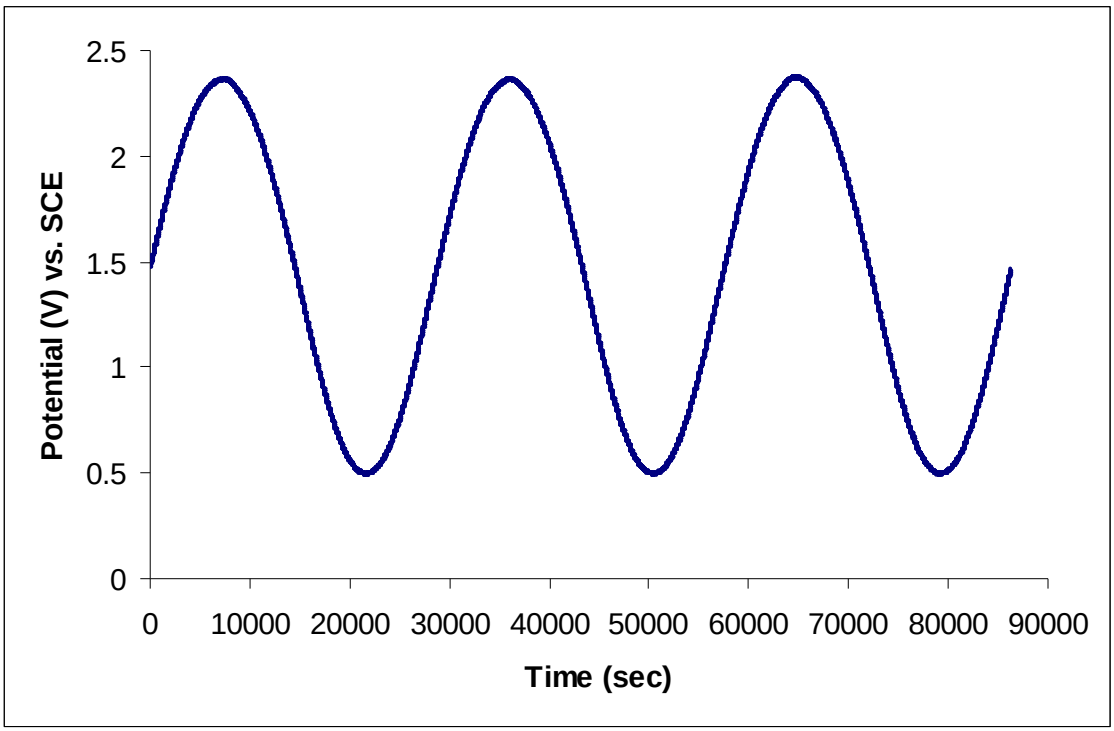

Figure 6-1: Electrical potential applied as a sine wave for annealed En24 at 3.47×10^{-5} Hz and 22ºC.

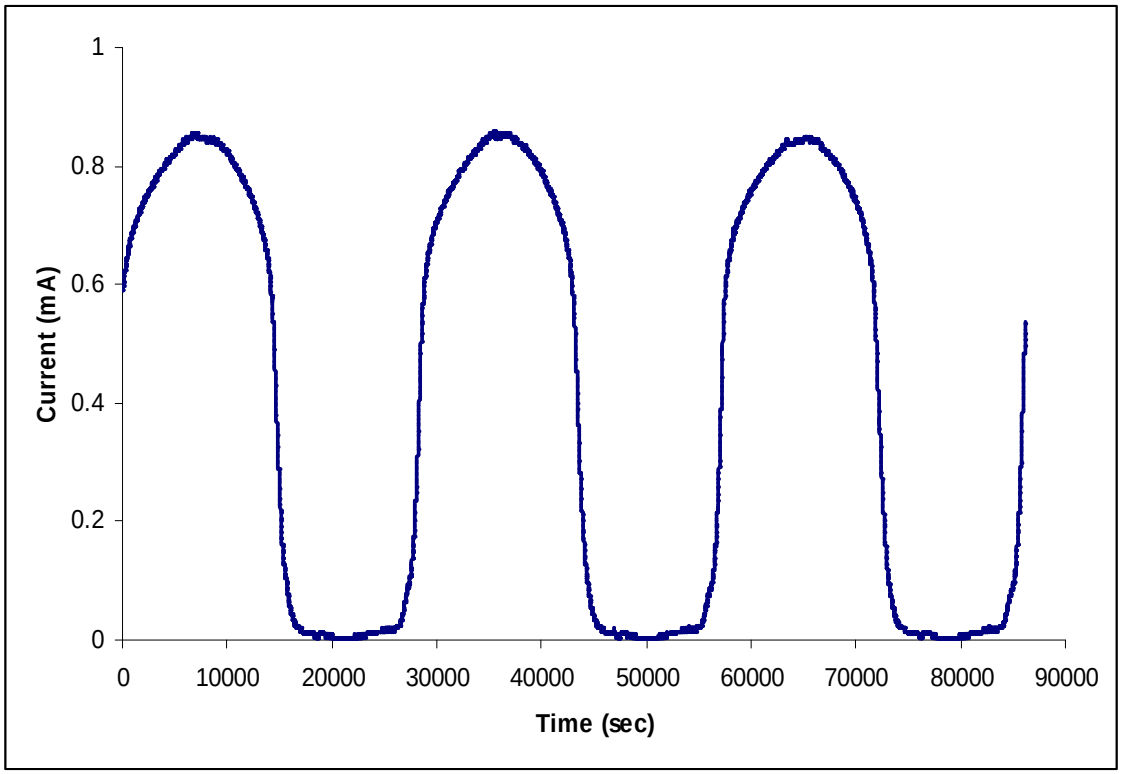

Figure 6-2: Current response to the potential shown in Figure 6-1.

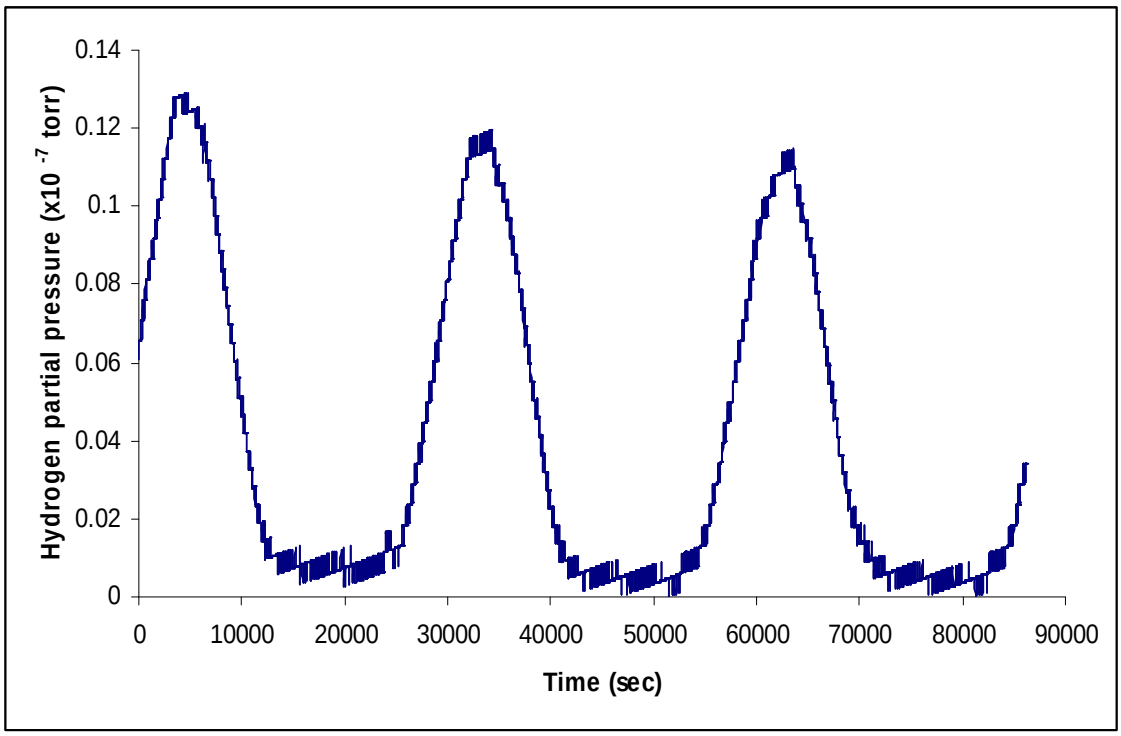

Figure 6-3: The response in hydrogen partial pressure for the potential shown in Figure 6-1.

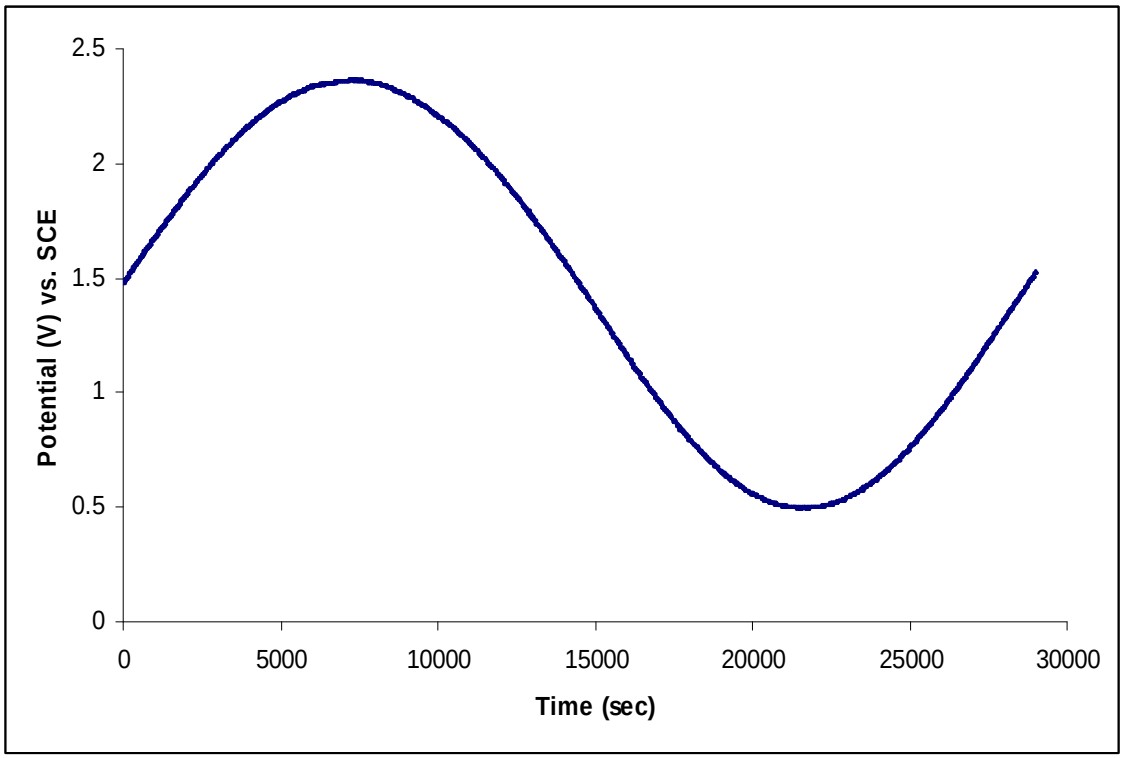

Figure 6-4: Signal-averaged potential from Figure 6-1.

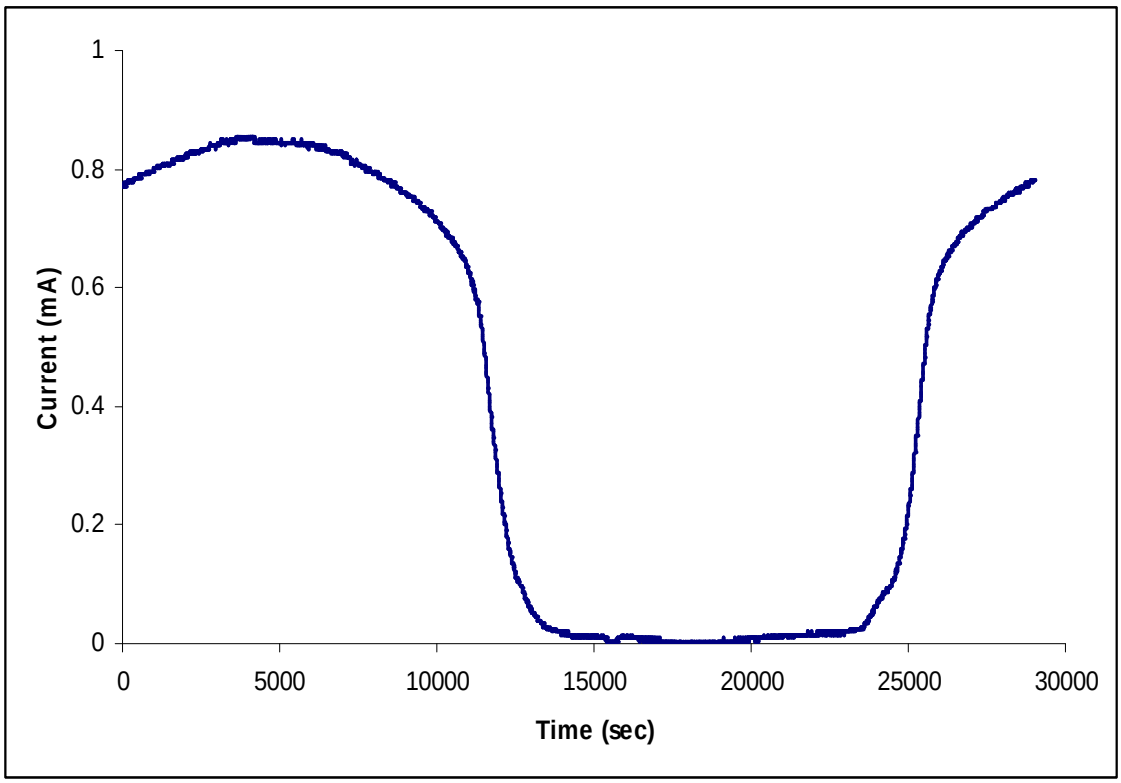

Figure 6-5: Signal-averaged current from Figure 6-2.

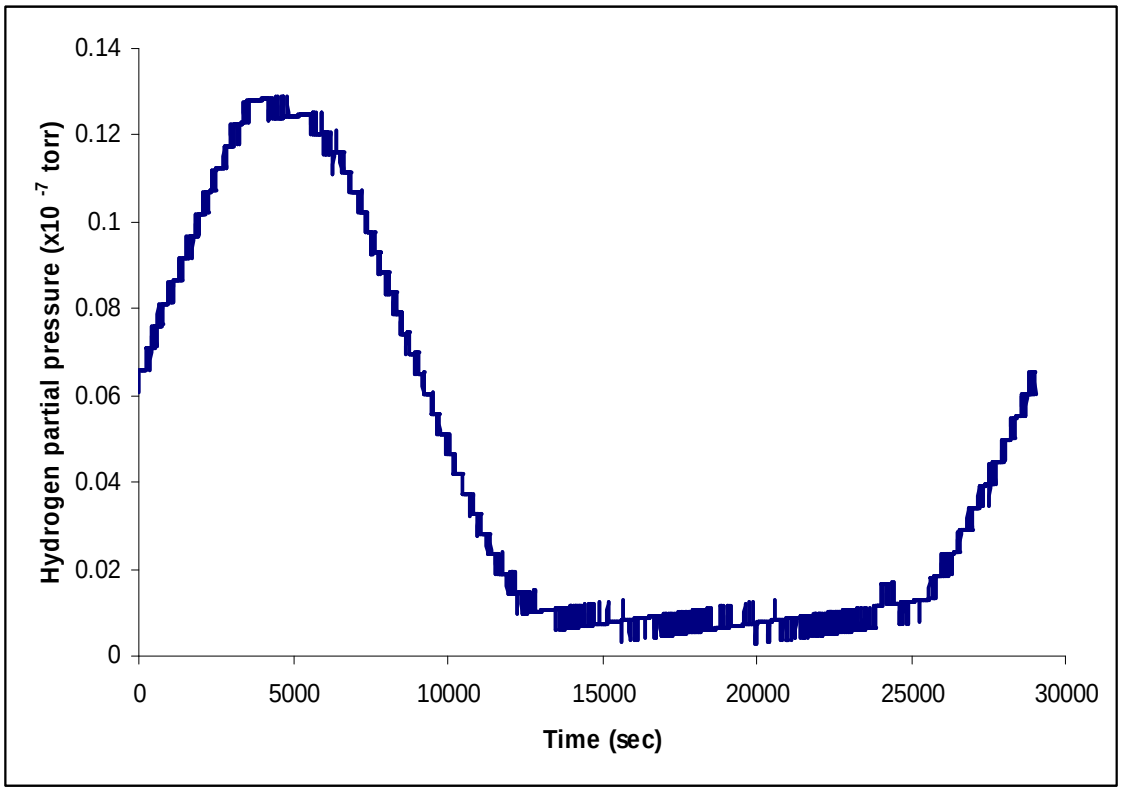

Figure 6-6: Signal-averaged partial pressure from Figure 6-3.

In common with the nickel specimen, the current curve is not perfectly sinusoidal, although, this time, the oscillations are flat-troughed (as opposed to flat-peaked). As before, this is attributed to a non-linear relationship between current and potential and, as before, the distortion is removed by the use of the Fourier Coefficients of the first harmonic.

The following graphs show the results of the phase lag (after removal of the pumping phase lag) and amplitude ratio between the current and the hydrogen partial pressure and the fitting of these results to the equations already derived in chapter four. The data were fitted to the equations for surface equilibrium as well as those including surface and trapping effects, respectively, in order to assess whether any such effects were present.

Equation (6-1) describes surface equilibrium for the phase lag and equation (6-2) describes amplitude ratio. As for the nickel specimen, data from the experiments on En24 were fitted to both of them to derive effective diffusion and solubility coefficients, which assume no trapping or surface hold-up.

$$\varphi = \arctan\left[\frac{\tanh kl - \tan kl}{\tan kl + \tanh kl}\right] \tag{6-1}$$

$$\Lambda = \frac{K}{2\sqrt{p_{ss}}} \frac{ART}{V\sqrt{\omega^2 + \beta^2}} \frac{\sqrt{2}Dk}{\sqrt{\sinh^2 kl + \sin^2 kl}} \tag{6-2}$$

To examine for possible surface effects, the same data were fitted to equation (6-3) describing the amplitude ratio and to equation (6-4) describing the phase lag between J and J_{curr}:

$$\left|\frac{J}{J_{curr}}\right| = \frac{2\sqrt{2}Dk}{f\sqrt{m^2 + n^2}} \tag{6-3}$$

$$\angle \frac{J}{J_{curr}} = \arctan \frac{m-n}{m+n} \tag{6-4}$$

where

$$f = \frac{2\cos(kl)\cosh(kl)}{k_{abs}}$$
$$m = b + c + (b-c)\tan(kl)\tanh kl) + e\tanh(kl) + d\tan(kl)$$
$$n = c - b + (c+b)\tan(kl)\tanh(kl) + e\tan(kl) - d\tanh(kl)$$
$$b = Dk\omega$$
$$c = Dk(k_{abs} - 2k_{ev})$$
$$d = \omega k_{des}$$
$$e = 2k_{des}(k_{abs} - k_{ev}\theta)$$

where k_{des} is the rate of desorption (m/s), k_{ev} is the rate of evolution (s^{-1}), k_{abs} is the rate of absorption (s^{-1}) and θ is the surface coverage of hydrogen (dimensionless).

To examine for trapping effects, equation (6-5) for the amplitude ratio and equation (6-6) for the phase lag, were used:

$$\Lambda = \frac{K}{2\sqrt{p_{ss}}} \frac{ART}{V\sqrt{\omega^2 + \beta^2}} \frac{D\sqrt{u^2 + v^2}}{\sqrt{\sinh^2 ul + \sin^2 vl}} \tag{6-5}$$

$$\varphi = \arctan\left[\frac{u\tanh vl - v\tan ul}{v\tan vl + u\tanh ul}\right] \tag{6-6}$$

where

$u = B\cos\left(\frac{1}{2}\tan^{-1}\frac{b}{a}\right), v = B\sin\left(\frac{1}{2}\tan^{-1}\frac{b}{a}\right), B = \frac{\left(a^2+b^2\right)^{1/4}}{\sqrt{D\left(p^2+\omega^2\right)}}, a = kN\omega^2,$
$b = \omega^3 + p(p+kN)\omega$, ω is the applied frequency (Hz), k the probability of a diffusing atom becoming trapped per second (s^{-1}), p is the probability that an occupied trap will release a captive atom within one second (s^{-1}), N is the density of the traps

(dimensionless), *D* is the hydrogen diffusion coefficient (m^2/s) and *K* is the hydrogen solubility coefficient (mol $H_2/m^3.mbar^{0.5}$).

The results of these fits are illustrated in Figures 6-7 to 6-13.

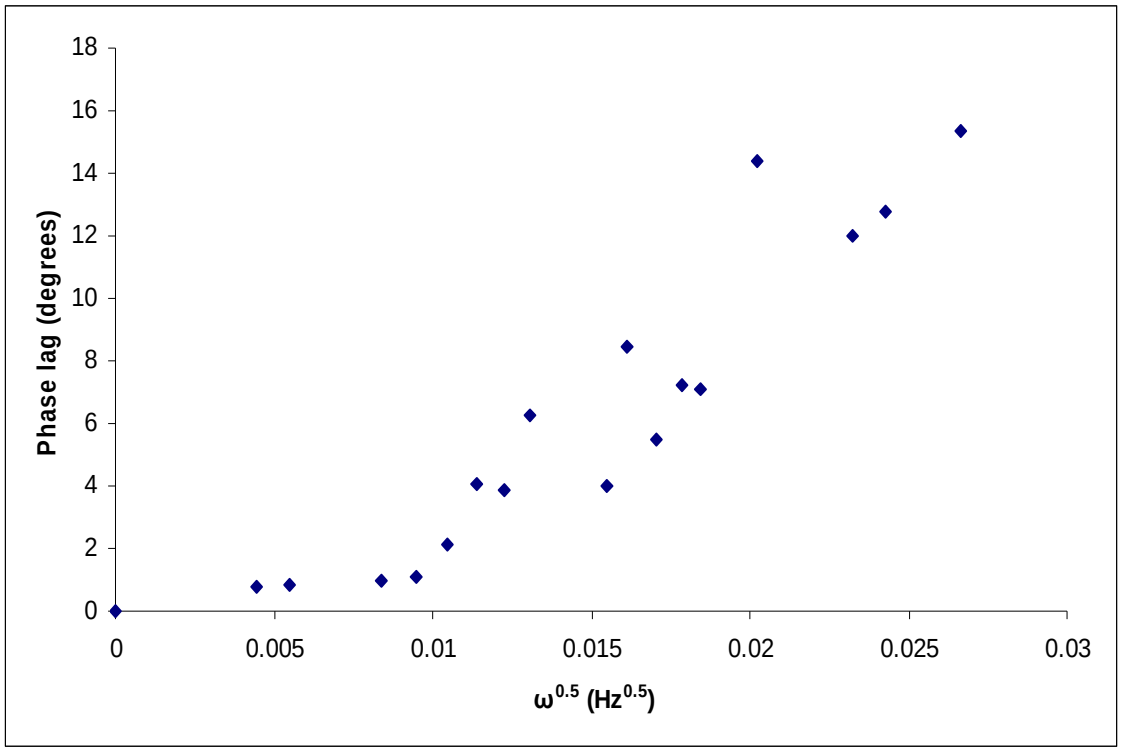

Figure 6-7: Phase lag results from the experiments on annealed En24.

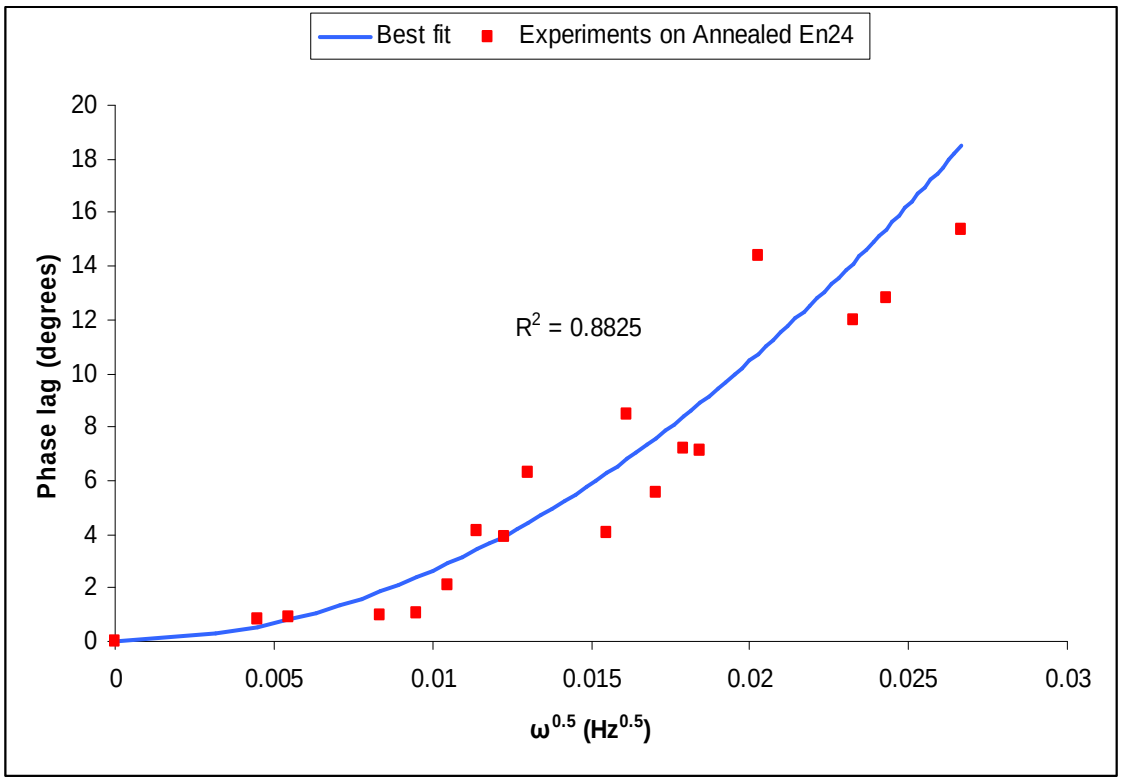

Figure 6-8: Phase lag results for annealed En24 fitted to surface equilibrium phase lag equation.

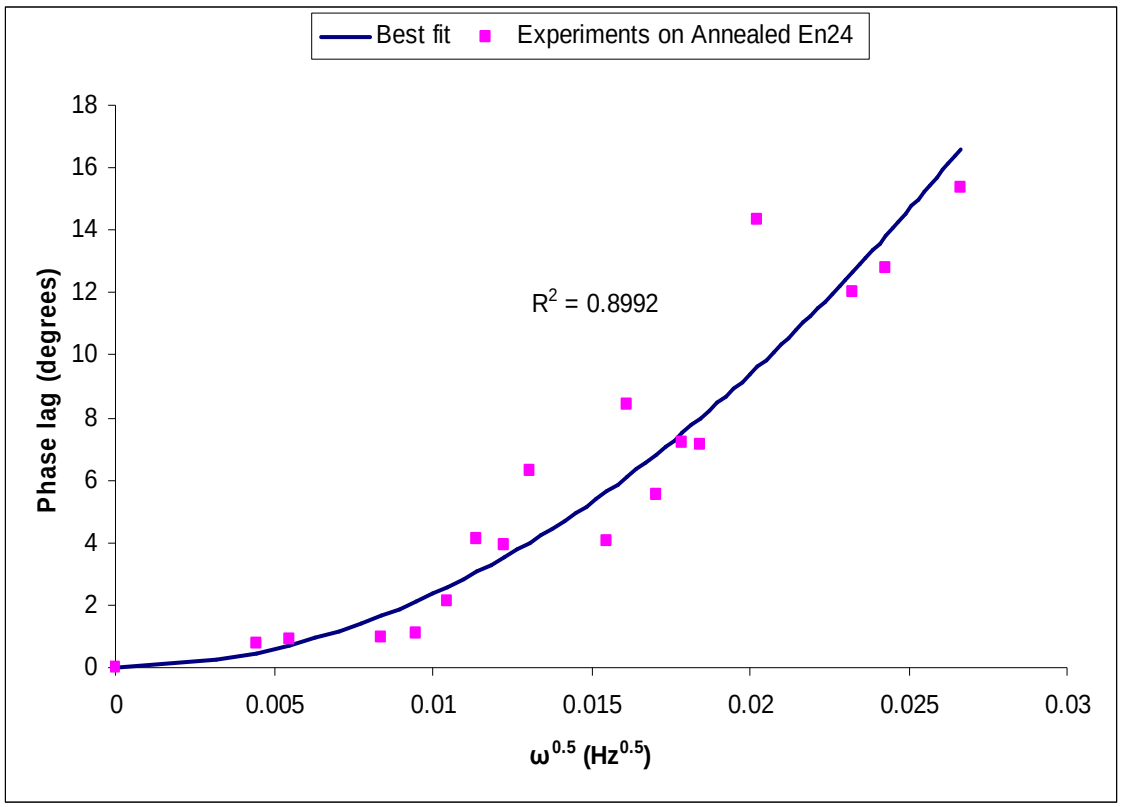

Figure 6-9: Phase lag results for annealed En24 fitted to trapping effects phase lag equation.

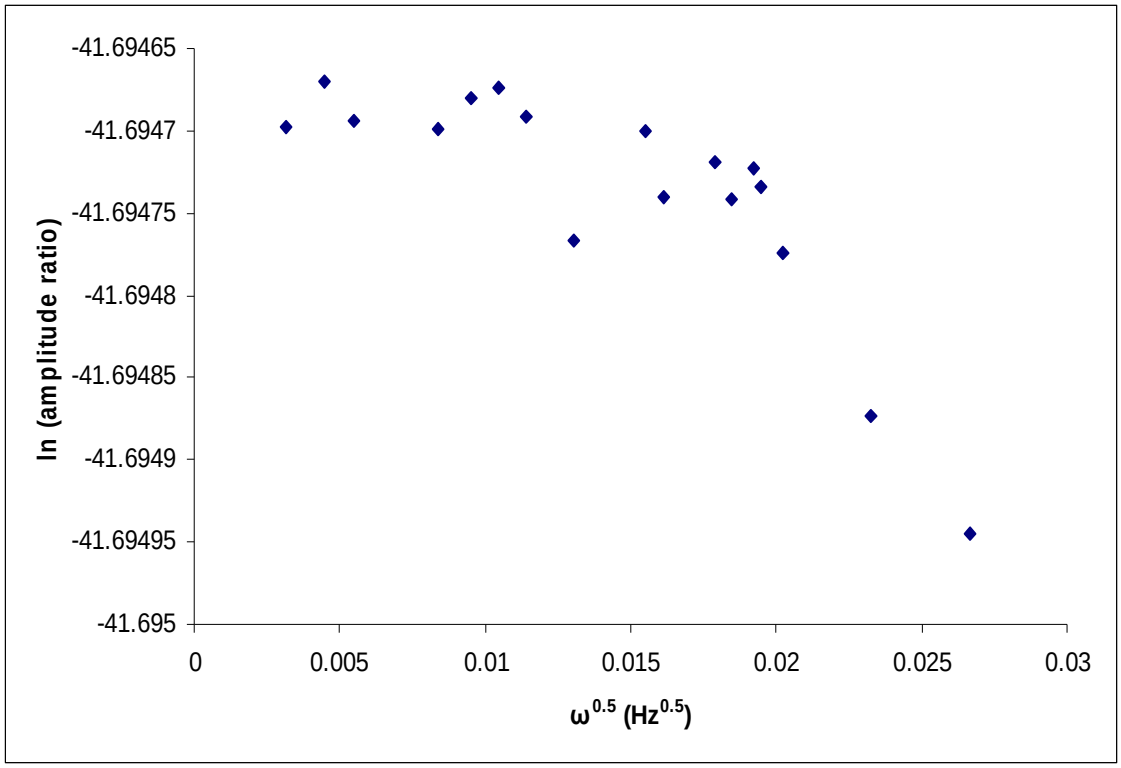

Figure 6-10: Amplitude ratio results from the experiments on annealed En24.

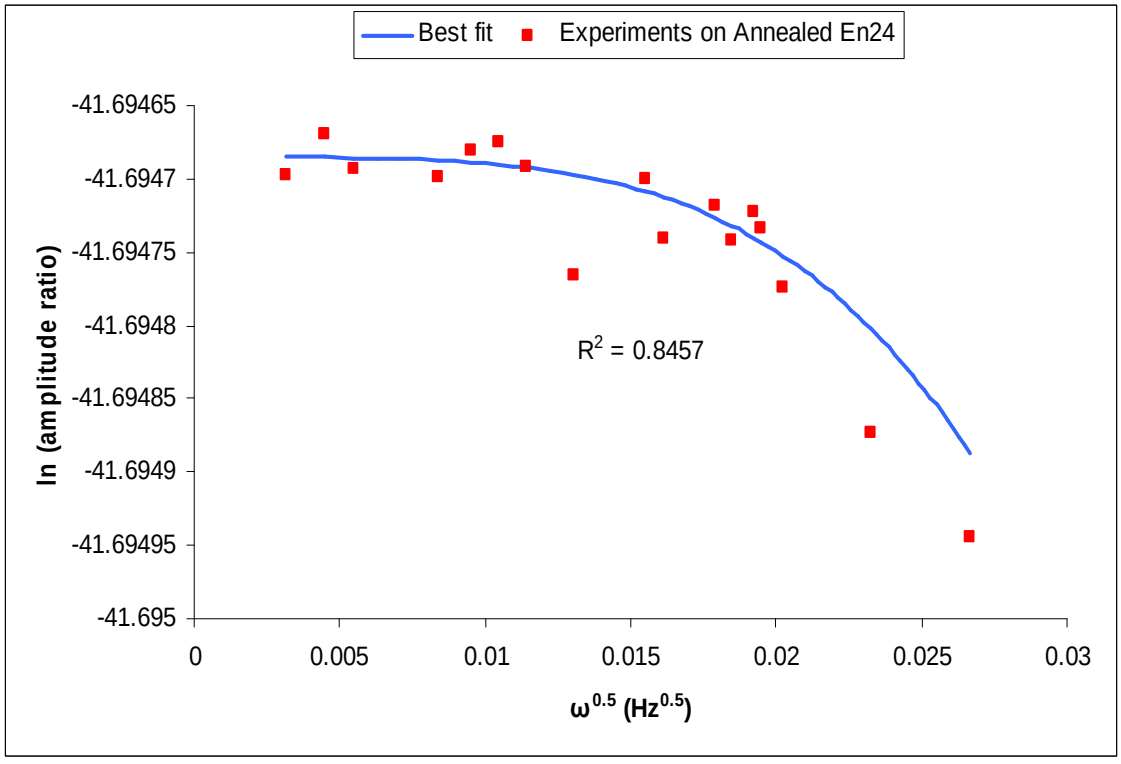

Figure 6-11: Amplitude ratio results for annealed En24 fitted to surface equilibrium amplitude ratio equation.

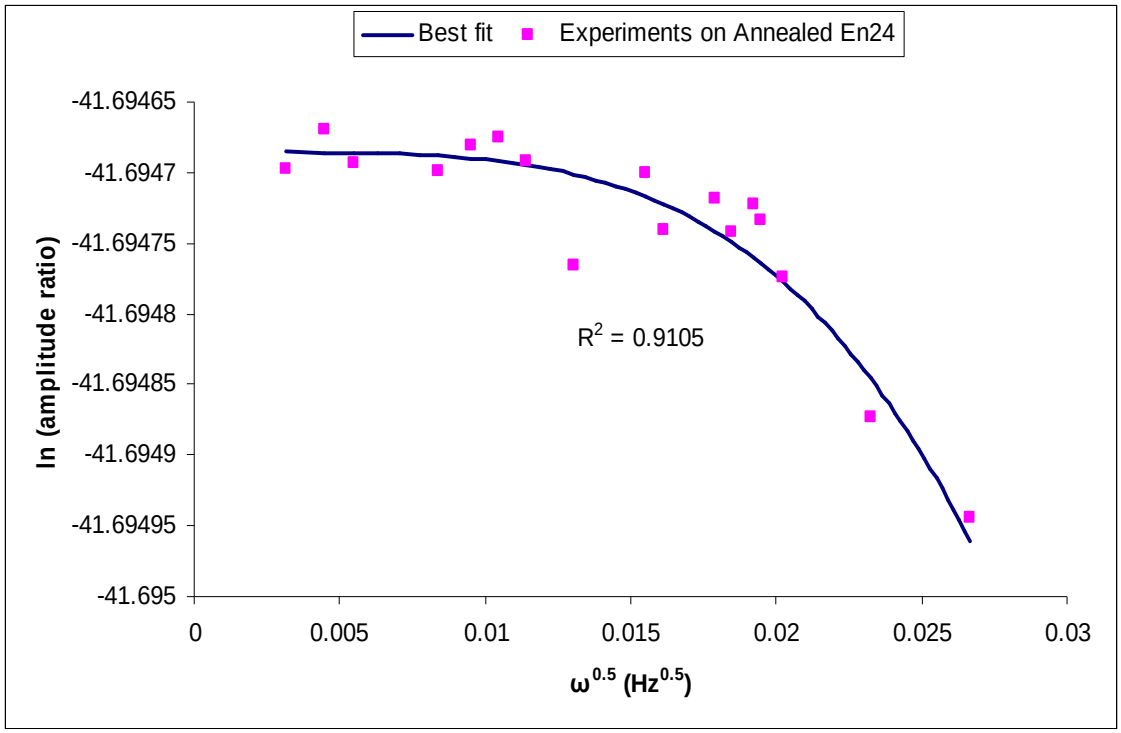

Figure 6-12: Amplitude ratio results fitted to trapping effects amplitude ratio equation.

The fitting to the surface equilibrium phase lag equation (6-1) resulted in a value of $D = (5.34\pm0.86)\times10^{-9}$ m^2/s, while the fitting to the amplitude ratio equation (6-2) gave $D = (3.55\pm1.18)\times10^{-9}$ m^2/s and $K = (1.7\pm0.54)\times10^{-11}$ mol H_2/m^3 mbar$^{0.5}$.

Results of applying the fitting procedures to the trapping equations are shown in Table 6-1.

Fitting to the phase lag trapping equation	Fitting to amplitude ratio trapping equation
$D = (2.45\pm0.82)\times10^{-10}$ m^2/s $p = 0.54\pm0.26$ s^{-1} $kN = 4.68\pm0.25$ s^{-1}	$D = (6.33\pm1.1)\times10^{-10}$ m^2/s $K = (4.2\pm1.3)\times10^{-9}$ mol H_2/m^3 mbar$^{0.5}$ $p = 0.95\pm0.21$ s^{-1} $kN = 1.98\pm0.33$ s^{-1}

Table 6-1: Results of the fitting procedures on trapping effects equations for the annealed En24 specimen.

Fitting the data to the surface effects equations (for all En24 specimens) was only possible for the phase lag equation (6-4) but not for the amplitude ratio equation as the attempts to carry out the fit procedure resulted in a very poor fit with negative values for R^2. Results from the fitting to the surface effects phase lag equation for annealed En24 are shown in Figure 6-13.

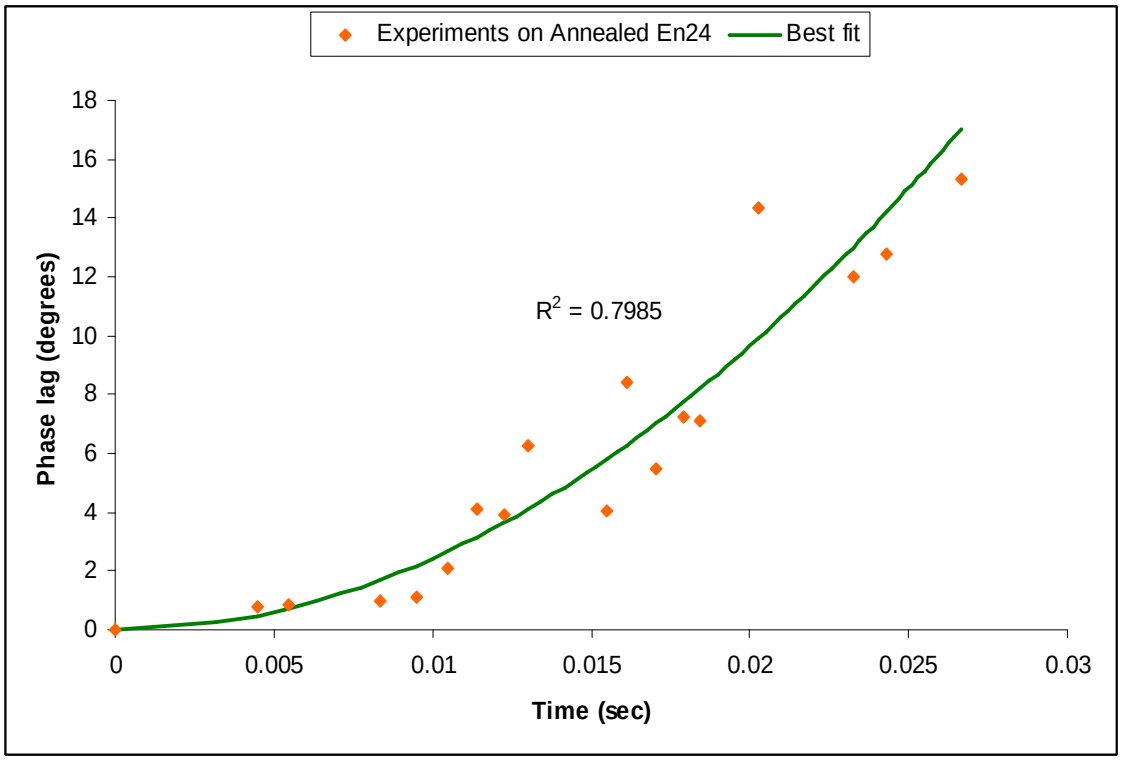

Figure 6-13: Phase lag results for annealed En24 fitted to surface effects phase lag equation.

The surface kinetic parameters derived from the fit shown in Figure 6-13 are presented in Table 6-2.

k_{des} (m/s)	k_{abs} (s^{-1})	k_{ev} (s^{-1})	θ	D (m^2/s)
$(9.6\pm0.62)\times10^{-3}$	$(1.61\pm0.2)\times10^{-2}$	$(9.84\pm1.05)\times10^{-3}$	0.6 ± 0.07	$(1.22\pm1.7)\times10^{-8}$

Table 6-2: Results of the fitting procedures to the surface effects phase lag equation for annealed En24.

Following this set of experiments, the specimen was heated up to 45°C for about 2 days in an attempt to remove any diffusible hydrogen; after that, another set of similar experiments were done to investigate whether this treatment had any effect on the hydrogen trapping behaviour of this specimen. Figures 6-14 to 6-19 show the results from these experiments and the fitting to the surface equilibrium and trapping equations. For good measure, the phase lag data were also fitted to the surface kinetic equation, Figure 6-20.

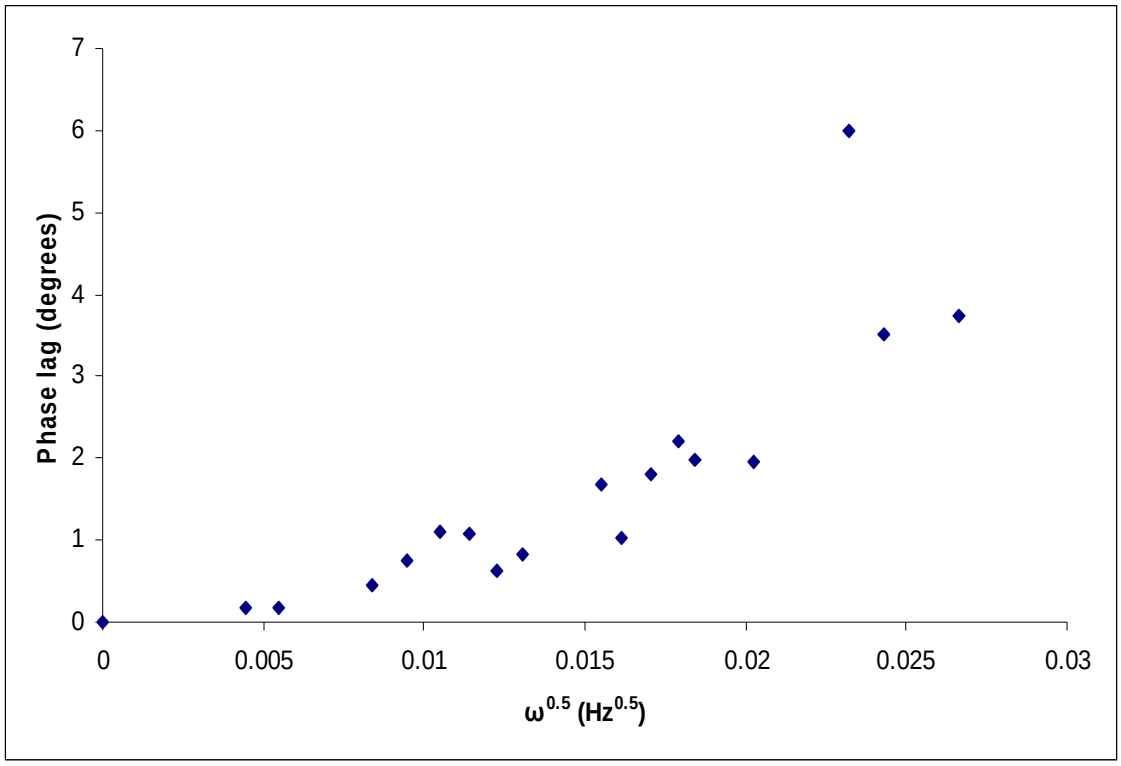

Figure 6-14: Phase lag results from the experiments on annealed En24 after heating up the specimen.

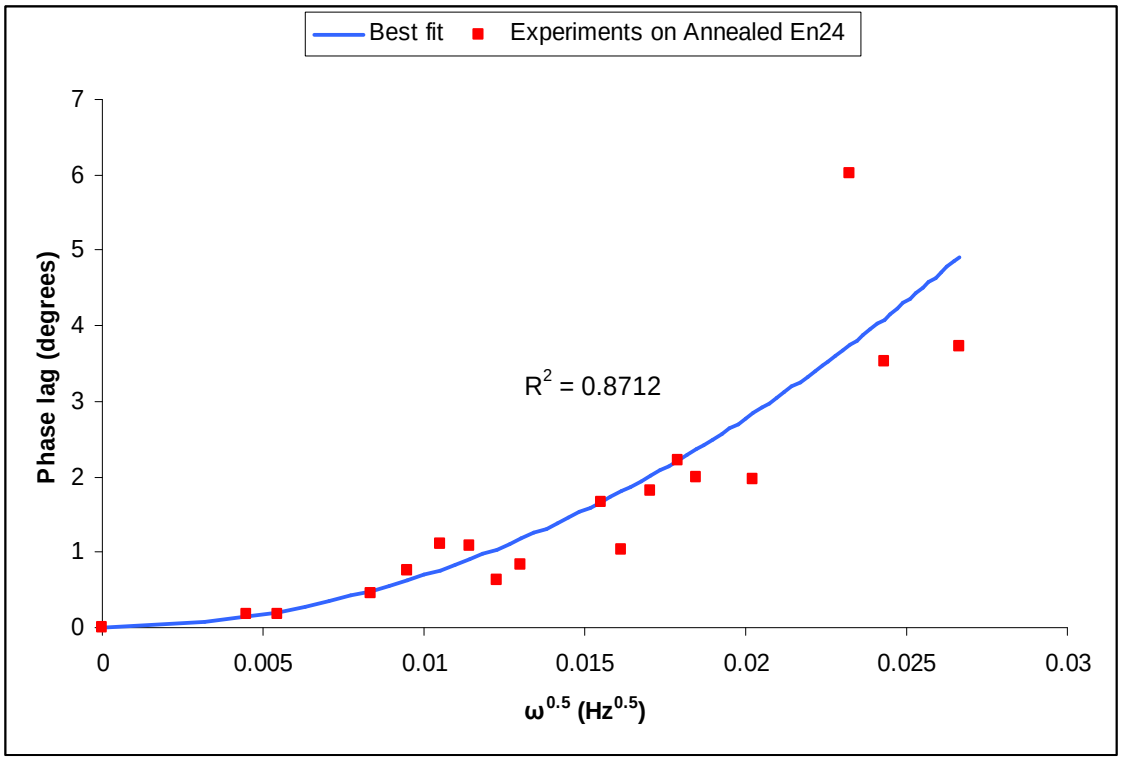

Figure 6-15: Phase lag results shown in Figure 6-14 fitted to surface equilibrium phase lag equation.

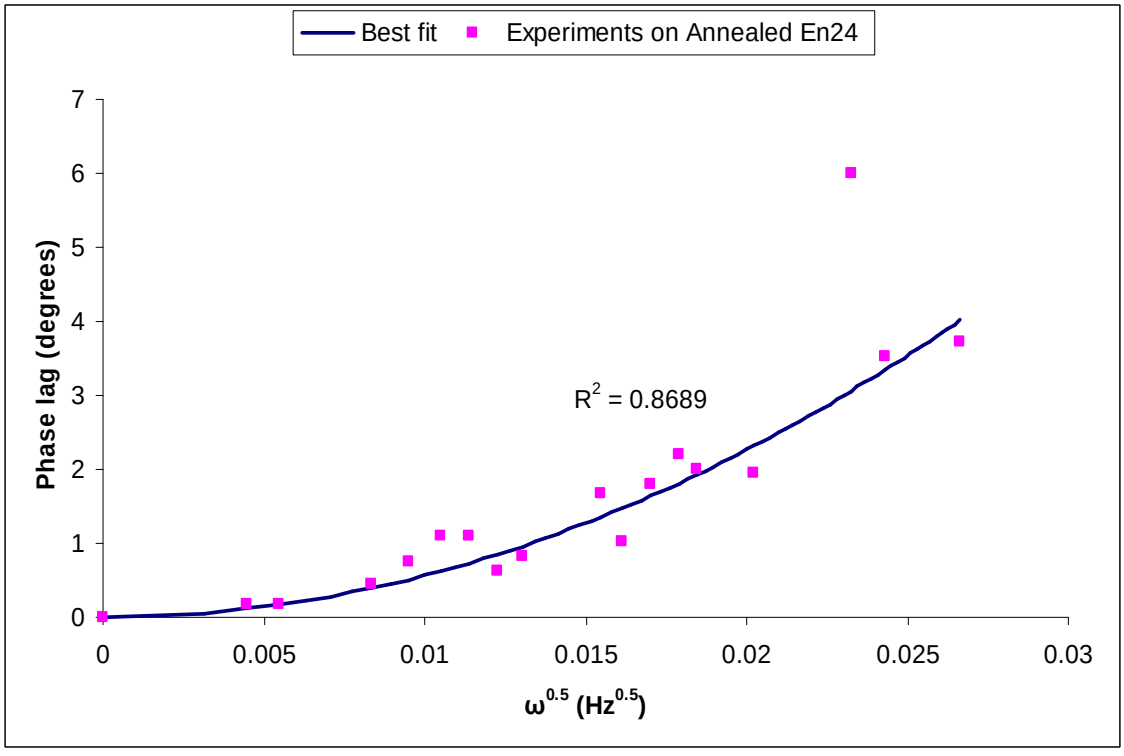

Figure 6-16: Phase lag results shown in Figure 6-14 fitted to trapping effects phase lag equation.

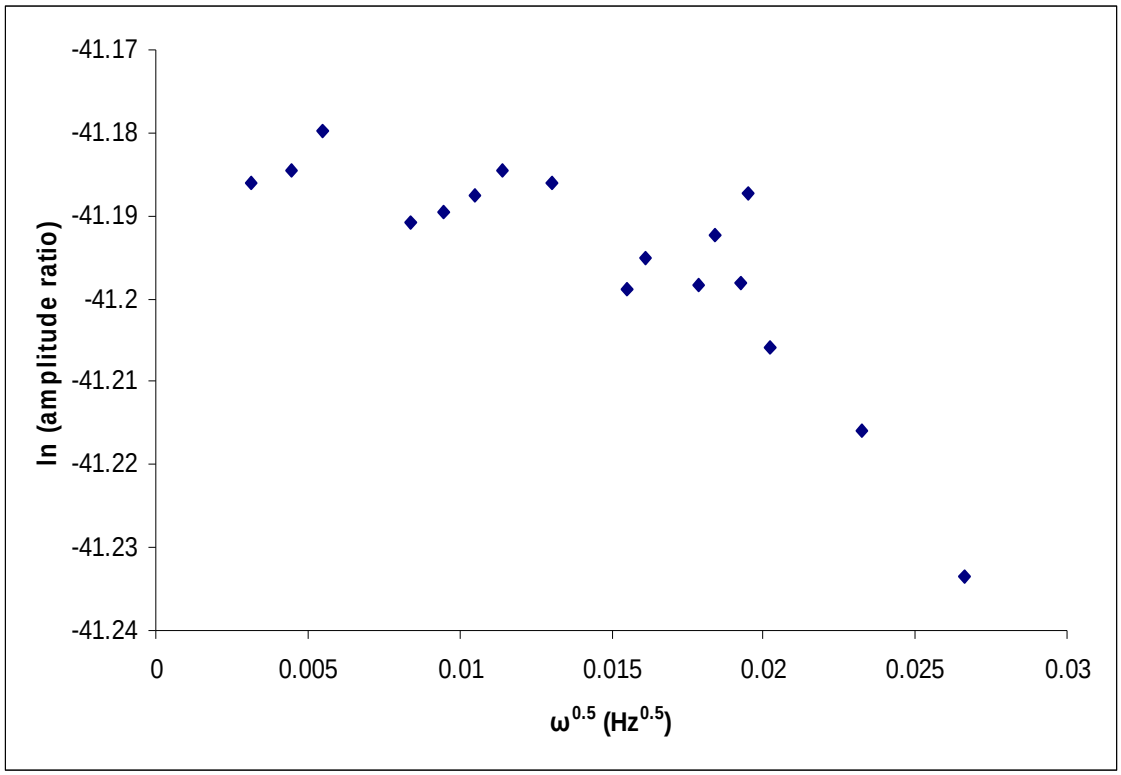

Figure 6-17: Amplitude ratio results from the experiments on annealed En24 after heating up the specimen.

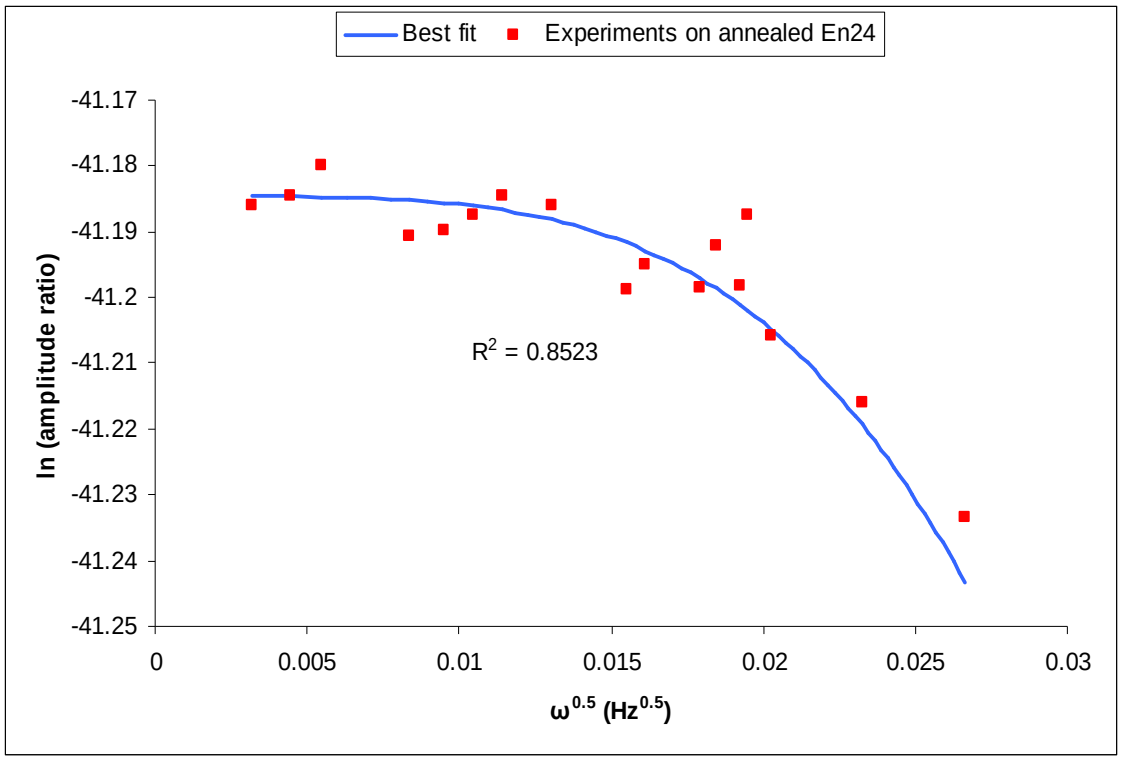

Figure 6-18: Amplitude ratio results from the experiments on annealed En24, after heating up the specimen, fitted to the surface equilibrium amplitude ratio equation.

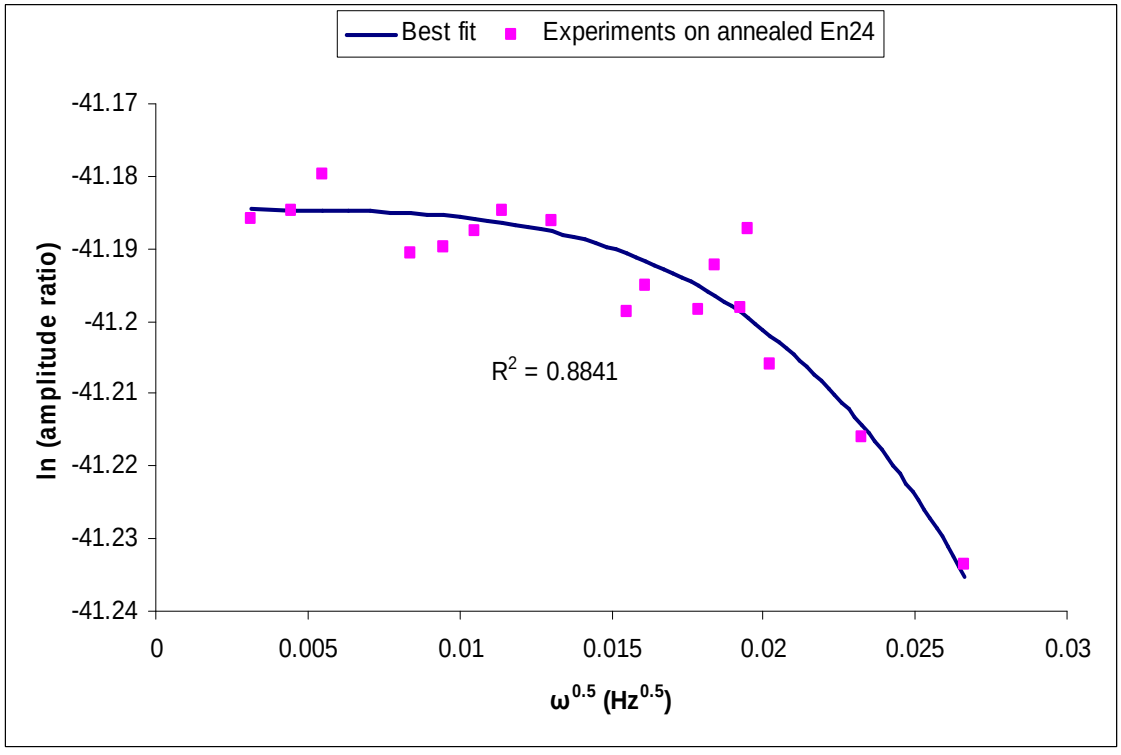

Figure 6-19: Amplitude ratio results shown in Figure 6-17 fitted to trapping effects amplitude ratio equation.

The fitting procedure to the surface equilibrium phase lag equation gave $D = (6.42\pm1.15)\times10^{-9}$ m^2/s, while the fitting to the amplitude ratio equation resulted in $D = (8.08\pm0.74)\times10^{-9}$ m^2/s and $K = (7.33\pm0.25)\times10^{-11}$ mol H_2/m^3 $mbar^{0.5}$.

Results from the trapping effects fitting are shown in Table 6-3.

Fitting to the phase lag trapping equation	Fitting to amplitude ratio trapping equation
$D = (8.34\pm1.4)\times10^{-10}$ m^2/s $p = 0.31\pm0.08$ s^{-1} $kN = 2.16\pm0.42$ s^{-1}	$D = (6.94\pm0.74)\times10^{-10}$ m^2/s $K = (6.37\pm1.65)\times10^{-9}$ mol H_2/m^3 $mbar^{0.5}$ $p = 0.09\pm0.02$ s^{-1} $kN = 4.48\pm0.68$ s^{-1}

Table 6-3: Results of the fitting procedures to trapping effects equations for the annealed En24 specimen (second set of experiments).

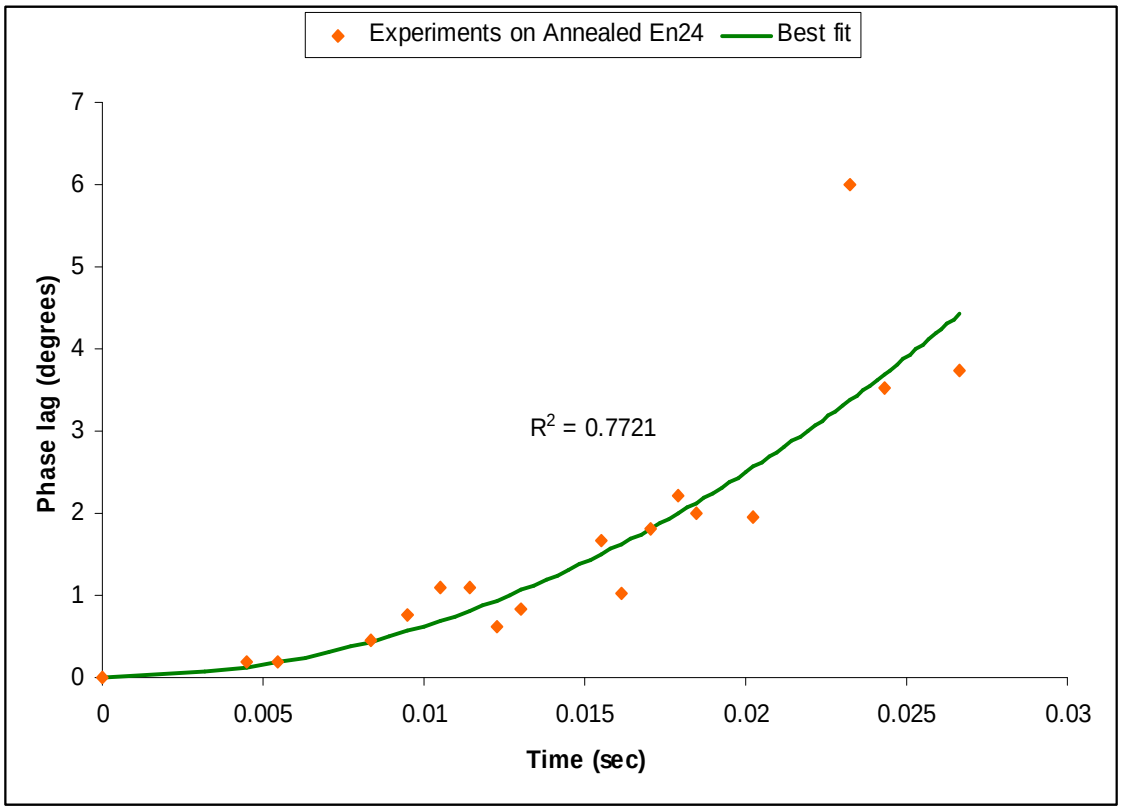

Figure 6-20: Phase lag results for annealed En24 (second run) fitted to surface effects equation.

k_{des} (m/s)	k_{abs} (s^{-1})	k_{ev} (s^{-1})	θ	D (m^2/s)
$(7.05\pm1.32)\times10^{-3}$	$(6.26\pm0.8)\times10^{-2}$	$(4.44\pm0.45)\times10^{-3}$	0.25 ± 0.15	$(3.5\pm1.2)\times10^{-7}$

Table 6-4: Results of the fitting procedures to the surface effects phase lag equation for annealed En24 (second run).

6.2 Quenched En24

In this condition, where the hardness was 508±1 HV, the diameter of the specimen was the same as the annealed one (83 mm) with an effective area of 25.5 cm^2 in contact with sodium hydroxide, but the thickness was about 0.35 mm. The same permeation conditions (potential modulations and frequencies) as were used for the annealed specimen, were used here for the quenched one.

Figures 6-21 to 6-25 show the phase lag and amplitude ratio results fitted to the surface equilibrium, trapping and surface hold-up equations. As before, a fit could not be obtained for the amplitude ratio with surface effects as a negative value for R^2 was obtained indicating a very poor (unreliable) fit for this case.

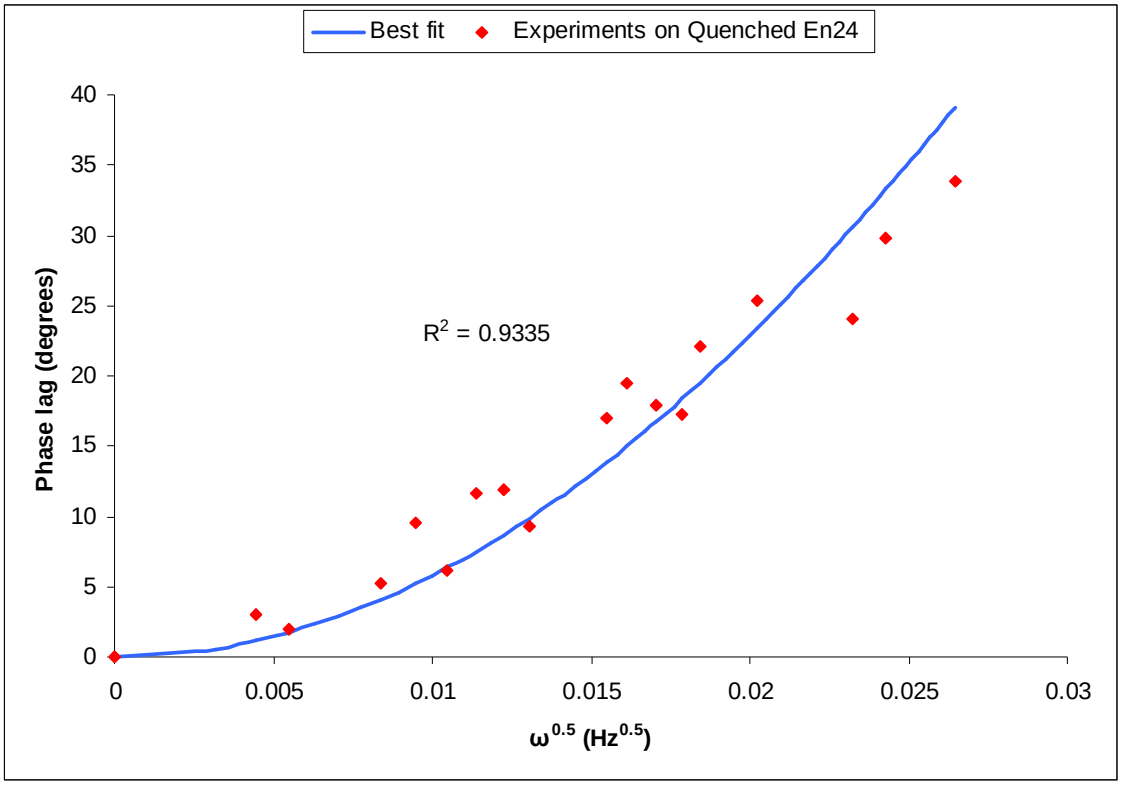

Figure 6-21: Phase lag results from the experiments on quenched En24 fitted to the surface equilibrium phase lag equation.

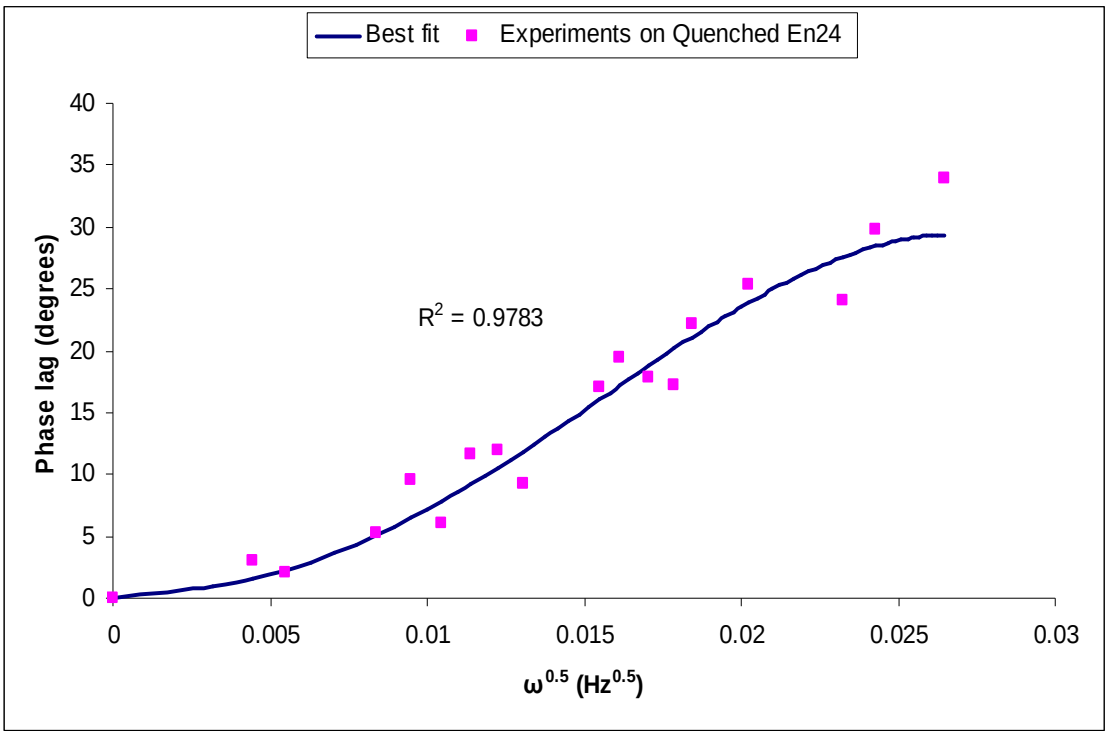

Figure 6-22: Phase lag results from the experiments on quenched En24 fitted to trapping effects phase lag equation.

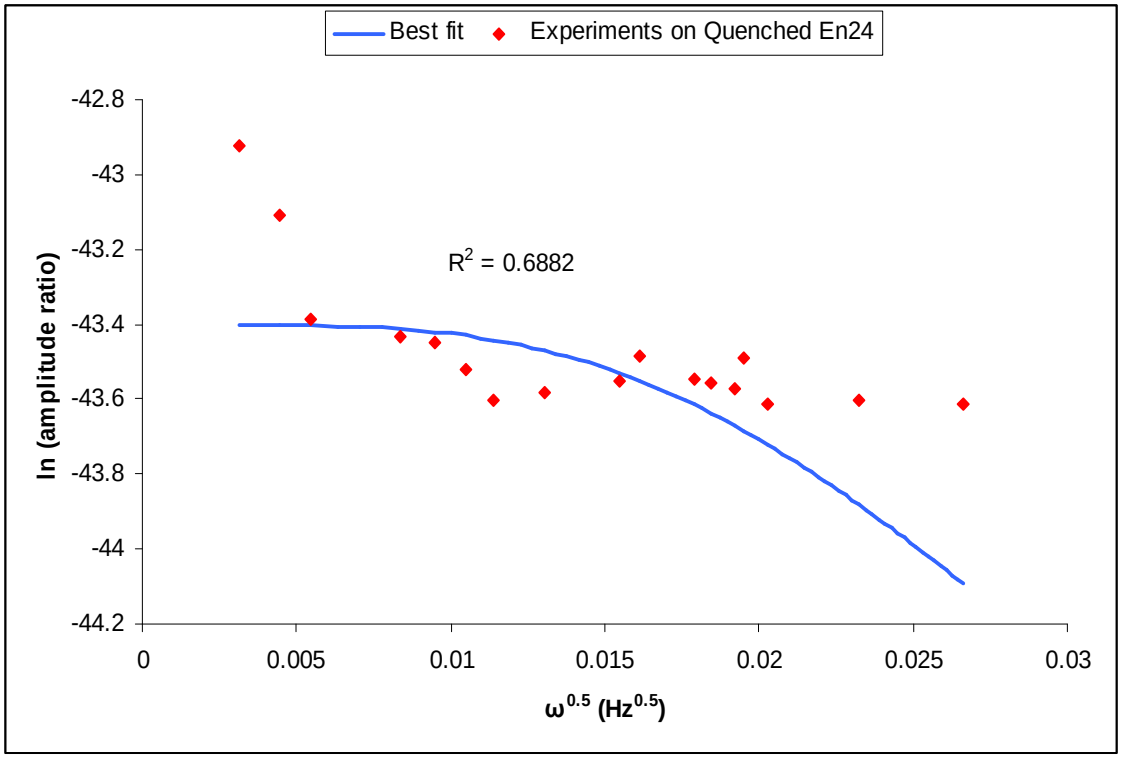

Figure 6-23: Amplitude ratio results from the experiments on quenched En24 fitted to the surface equilibrium amplitude ratio equation.

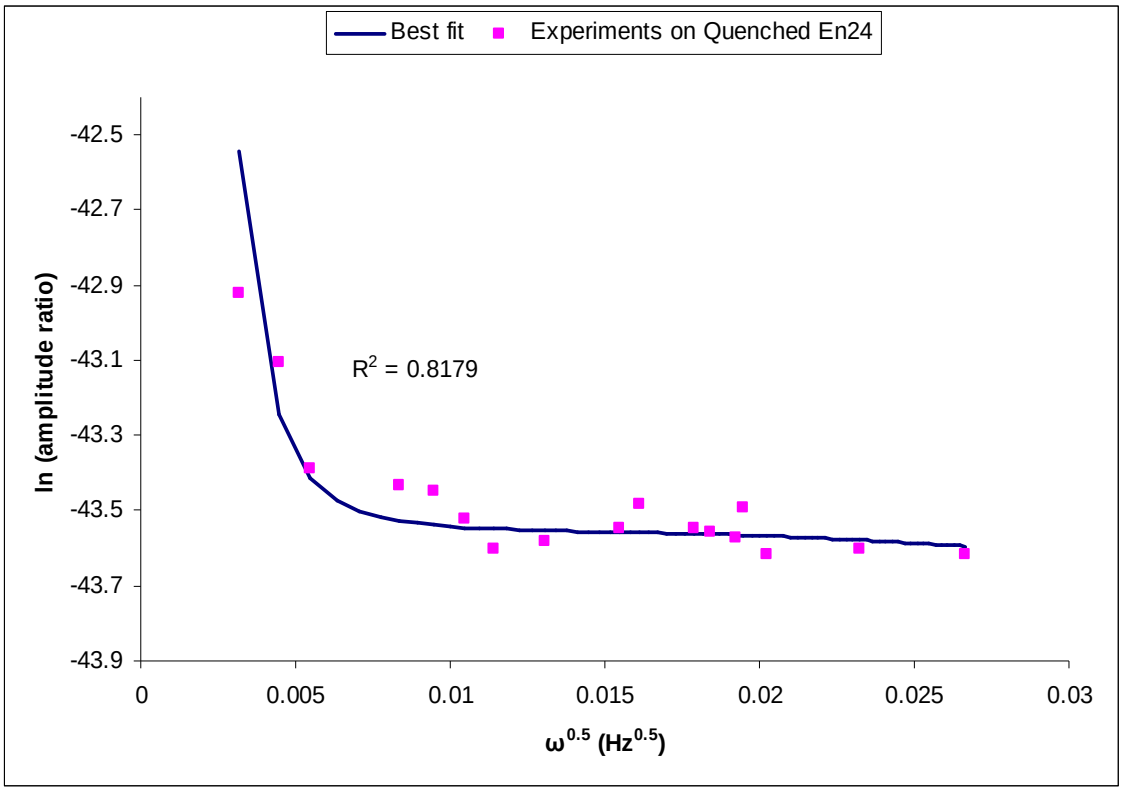

Figure 6-24: Amplitude ratio results from the experiments on quenched En24 fitted to trapping effects amplitude ratio equation.

The diffusion coefficient resulting from the fitting to the surface equilibrium equation was $D = (2.26\pm1.5)\times10^{-11}$ m^2/s, while fitting to the amplitude ratio equation, for diffusion coefficient and solubility coefficient independently, gave a diffusion coefficient of $D = (3.18\pm0.42)\times10^{-11}$ m^2/s and solubility coefficient of $K = (4.8\pm0.5)\times10^{-7}$ mol H_2/m^3 $mbar^{0.5}$.

The permeation/trapping parameters obtained from fitting to the same data are shown in Table 6-5.

Fitting to the phase lag trapping equation	Fitting to amplitude ratio trapping equation
$D = (8.98\pm0.57)\times10^{-12}$ m^2/s $p = (1.21\pm1.05)\times10^{-7}$ s^{-1} $kN = (2.47\pm0.36)\times10^{-3}$ s^{-1}	$D = (6.8\pm1.8)\times10^{-12}$ m^2/s $K = (3.28\pm0.94)\times10^{-5}$ mol H_2/m^3 mbar$^{0.5}$ $p = (6.68\pm1.17)\times10^{-6}$ s^{-1} $kN = (3.2\pm0.75)\times10^{-3}$ s^{-1}

Table 6-5: Results of the fitting procedures to trapping effects equations for the quenched En24 specimen.

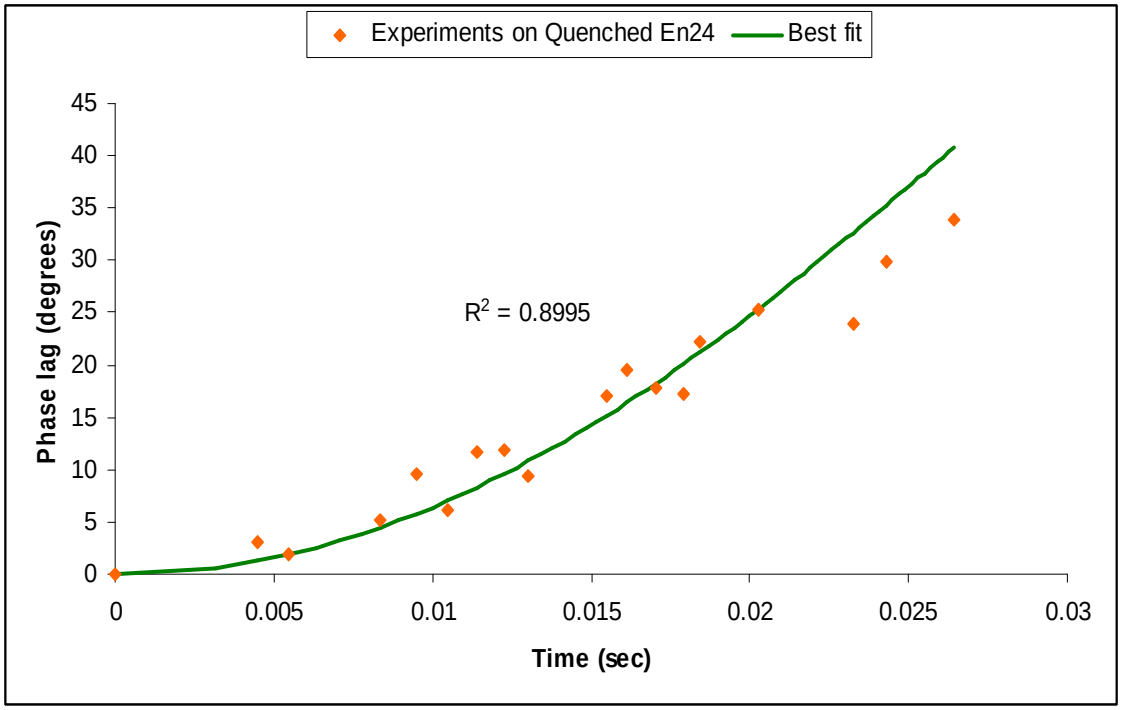

Figure 6-25: Phase lag results from the experiments on quenched En24 fitted to surface effects equation.

Results from the fitting to the surface effects equation for quenched En24 are displayed in Table 6-6.

k_{des} (m/s)	k_{abs} (s^{-1})	k_{ev} (s^{-1})	θ	D (m^2/s)
$(5.8\pm0.85)\times10^{-5}$	0.57±0.12	$(5.2\pm0.38)\times10^{-4}$	0.86±0.25	$(2.8\pm1)\times10^{-11}$

Table 6-6: Results of the fitting procedures to the surface effects phase lag equation for quenched En24.

6.3 Quenched and Tempered En24

In this condition, the hardness was reduced to 413±2 HV. All dimensions were as before, except that the thickness was about 0.65 mm.

The potential was modulated between 1000 and 3000 (mV) vs. SCE because this relatively thicker specimen required a higher potential than that used for specimens in the two previous heat treatment conditions and thicknesses to generate a detectable hydrogen flux in the vacuum chamber. Frequencies ranged between 1.3×10^{-5} and 7×10^{-4} Hz.

Figures 6-26 to 6-29 show the results of the phase lag and amplitude ratio fitted to the surface equilibrium, trapping and surface hold-up equations. Again, it was not possible to fit the data to both the surface equilibrium and surface hold-up amplitude ratio equations because of very poor indications.

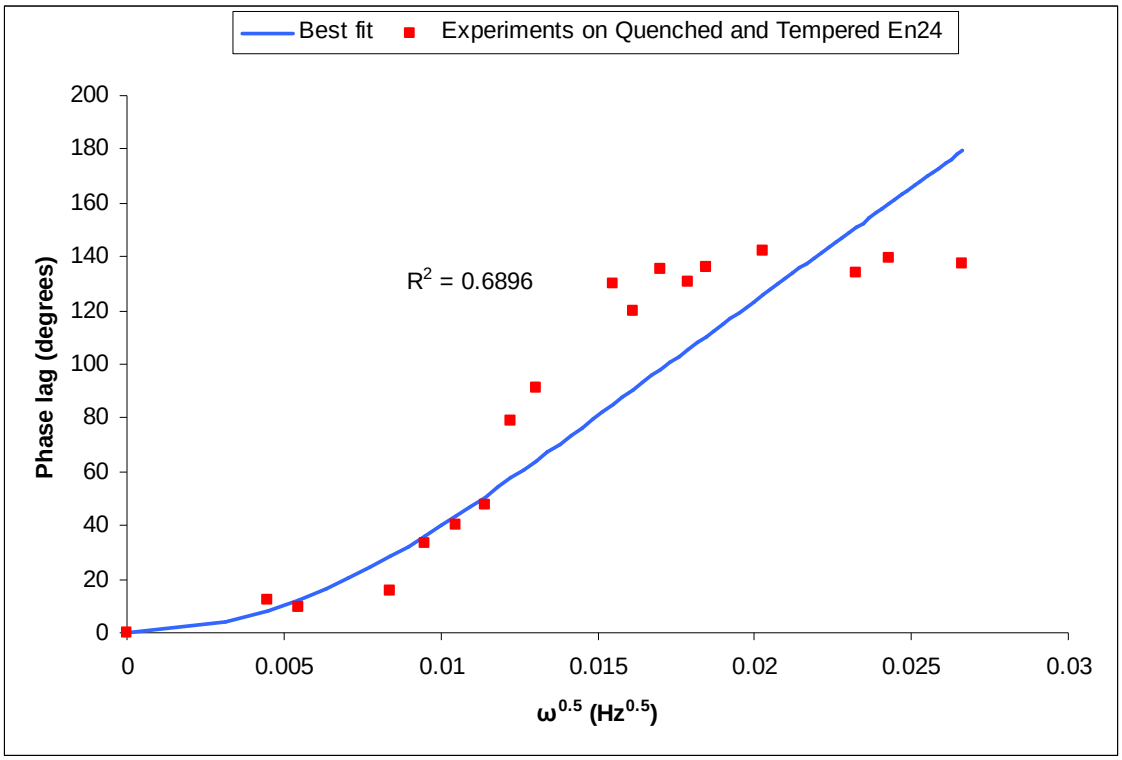

Figure 6-26: Phase lag results from the experiments on quenched and tempered En24 fitted to the surface equilibrium phase lag equation.

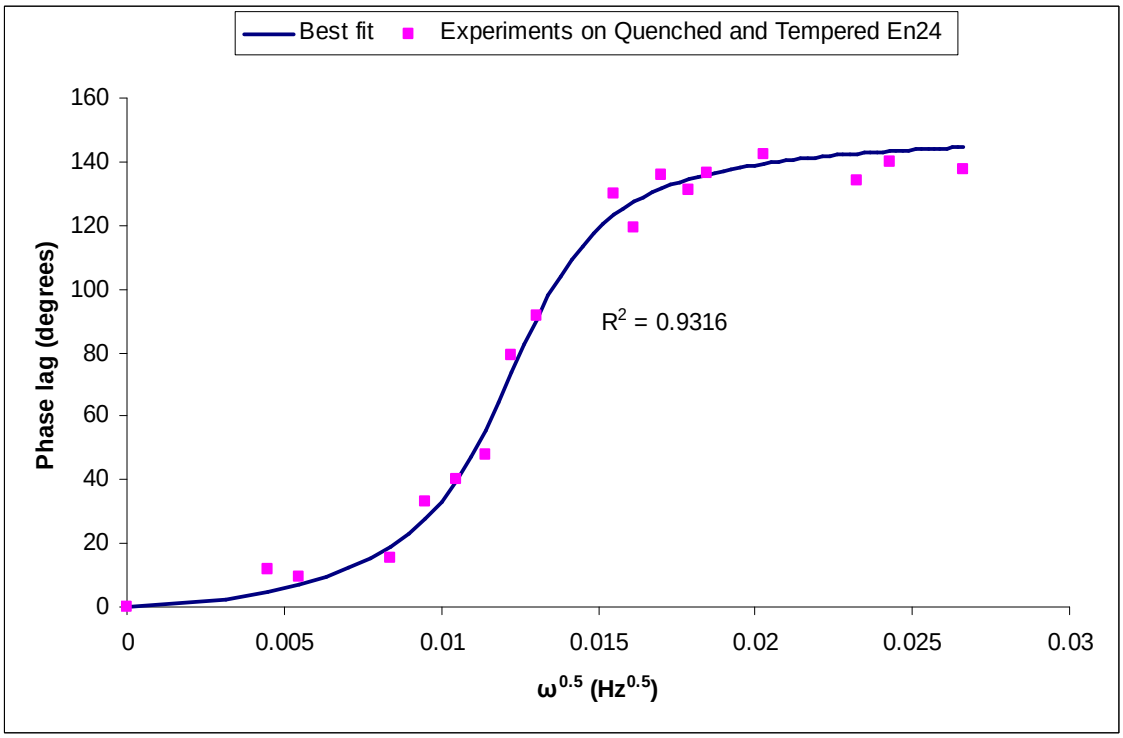

Figure 6-27: Phase lag results from the experiments on quenched and tempered En24 fitted to the trapping effects phase lag equation.

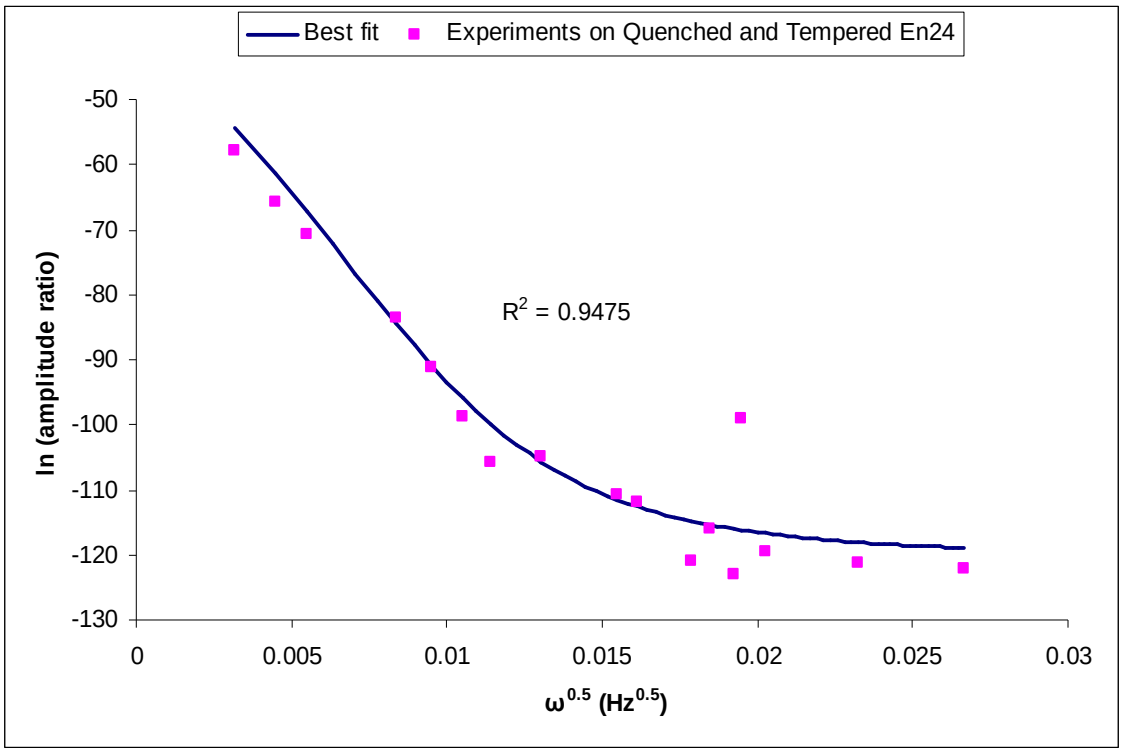

Figure 6-28: Amplitude ratio results from the experiments on quenched and tempered En24 fitted to the trapping effects amplitude ratio equation.

Fitting to the surface equilibrium phase lag equation gave $D = (2.3\pm0.56)\times10^{-12}$ m^2/s.

Fitting to the phase lag trapping equation	Fitting to amplitude ratio trapping equation
$D = (2.94\pm1.25)\times10^{-11}$ m^2/s $p = (2.98\pm1.5)\times10^{-4}$ s^{-1} $kN = 0.3\pm0.13$ s^{-1}	$D = (3.57\pm0.35)\times10^{-11}$ m^2/s $K = (1.22\pm0.6)\times10^{-7}$ mol H_2/m^3 mbar$^{0.5}$ $p = (1.4\pm0.86)\times10^{-4}$ s^{-1} $kN = 0.6\pm0.28$ s^{-1}

Table 6-7: Results of the fitting procedures to trapping effects equations for the quenched and tempered En24 specimen.

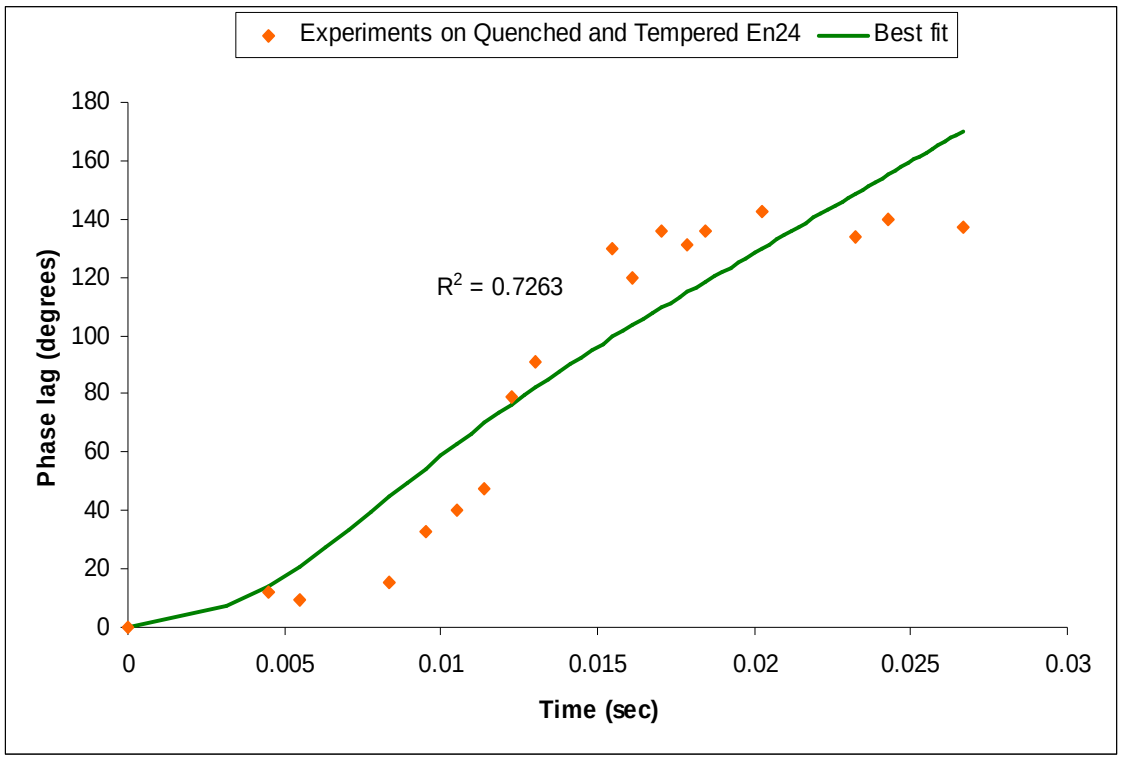

Figure 6-29: Phase lag results from the experiments on quenched and tempered En24 fitted to surface effects phase lag equation.

Results from the fitting to the surface effects equation for quenched and tempered En24 are displayed in Table 6-8.

k_{des} (m/s)	k_{abs} (s^{-1})	k_{ev} (s^{-1})	θ	D (m^2/s)
$(4.28\pm1.18)\times10^{-6}$	0.48 ± 0.2	$(1.5\pm0.11)\times10^{-2}$	0.65 ± 0.06	$(2.52\pm0.34)\times10^{-12}$

Table 6-8: Results of the fitting procedures to the surface effects phase lag equation for quenched and tempered En24.

6.4 Summary of Results

Tables 6-9 to 6-11 summarise the results obtained for the En24 specimens, in terms of the parameters which can be derived assuming surface equilibrium (Table 6-9), trapping (Table 6-10) and surface hold-up (Table 6-11). These results are discussed in the next

chapter in the context of the literature data on diffusion coefficients, solubility coefficients and trapping and surface effects in low alloy steels.

Specimen	Surface Equilibrium				
	Phase lag	R^2	Amplitude ratio		R^2
	D (m^2/s)		D (m^2/s)	K (mol H_2/m^3 $mbar^{0.5}$)	
Annealed (thickness = 0.25 mm)	$(5.34\pm0.86)\times10^{-9}$	0.8825	$(3.55\pm1.18)\times10^{-9}$	$(1.7\pm0.54)\times10^{-11}$	0.8457
Annealed (second run) (thickness = 0.25 mm)	$(6.42\pm1.15)\times10^{-9}$	0.8712	$(8.08\pm0.74)\times10^{-9}$	$(7.33\pm0.25)\times10^{-11}$	0.8523
Quenched (thickness = 0.35 mm)	$(2.26\pm1.5)\times10^{-11}$	0.9335	$(3.18\pm0.42)\times10^{-11}$	$(4.8\pm0.5)\times10^{-7}$	0.6882
Quenched and Tempered (thickness = 0.65 mm)	$(2.3\pm0.56)\times10^{-12}$	0.6896	-	-	-

Table 6-9: Results from fitting En24 data to surface equilibrium equations (effective diffusion and solubility coefficients.)

Specimen	Trapping Effects								
	Phase lag			R^2	Amplitude ratio				R^2
	D (m^2/s)	p (s^{-1})	kN (s^{-1})		D (m^2/s)	K (mol H_2/m^3 $mbar^{0.5}$)	p (s^{-1})	kN (s^{-1})	
Annealed (thickness = 0.25 mm)	$(2.45\pm0.82)\times10^{-10}$	0.54±0.26	4.68±0.25	0.8992	$(6.33\pm1.1)\times10^{-10}$	$(4.2\pm1.3)\times10^{-9}$	0.95±0.21	1.98±0.33	0.9105
Annealed (second run) (thickness = 0.25 mm)	$(8.34\pm1.4)\times10^{-10}$	0.31±0.08	2.16±0.42	0.8689	$(6.94\pm0.74)\times10^{-10}$	$(6.37\pm1.65)\times10^{-9}$	0.09±0.02	4.48±0.68	0.8841
Quenched (thickness = 0.35 mm)	$(8.98\pm0.57)\times10^{-12}$	$(1.21\pm1.05)\times10^{-7}$	$(2.47\pm0.36)\times10^{-3}$	0.9783	$(6.8\pm1.8)\times10^{-12}$	$(3.28\pm0.94)\times10^{-5}$	$(6.68\pm1.17)\times10^{-6}$	$(3.2\pm0.75)\times10^{-3}$	0.8179
Quenched and Tempered (thickness = 0.65 mm)	$(2.94\pm1.25)\times10^{-11}$	$(2.98\pm1.5)\times10^{-4}$	0.3±0.13	0.9316	$(3.57\pm0.35)\times10^{-11}$	$(1.22\pm0.6)\times10^{-7}$	$(1.4\pm0.86)\times10^{-4}$	0.6±0.28	0.9475

Table 6-10: Results from fitting En24 data to trapping effects equations.

Specimen	Surface Effects					
	Phase lag					R^2
	D (m^2/s)	k_{des} (m/s)	k_{abs} (s^{-1})	k_{ev} (s^{-1})	θ	
Annealed (thickness = 0.25 mm)	$(1.22\pm1.7)\times10^{-8}$	$(9.6\pm0.62)\times10^{-3}$	$(1.61\pm0.2)\times10^{-2}$	$(9.84\pm1.05)\times10^{-3}$	0.6±0.07	0.7985
Annealed (second run) (thickness = 0.25 mm)	$(3.5\pm1.2)\times10^{-7}$	$(7.05\pm1.32)\times10^{-3}$	$(6.26\pm0.8)\times10^{-2}$	$(4.44\pm0.45)\times10^{-3}$	0.25±0.15	0.7721
Quenched (thickness = 0.35 mm)	$(2.8\pm1)\times10^{-11}$	$(5.8\pm0.85)\times10^{-5}$	0.57±0.12	$(5.2\pm0.38)\times10^{-4}$	0.86±0.25	0.8995
Quenched and Tempered (thickness = 0.65 mm)	$(2.52\pm0.34)\times10^{-12}$	$(4.28\pm1.18)\times10^{-6}$	0.48±0.2	$(1.5\pm0.11)\times10^{-2}$	0.65±0.06	0.7263

Table 6-11: Results from fitting En24 data to surface effects equations.

Chapter 7

Discussion

This discussion is divided into two parts. Firstly, the results on nickel are discussed against the claim that the degree of averaging possible in the current experiment provides a very precise measure of kinetic parameters. Secondly, the results on steel are discussed, here in the context of non-diffusion-controlled permeation phenomena and also in the context of the meaning of reported values of diffusivity and solubility.

7.1 Nickel

Hydrogen permeation in nickel has been studied extensively in the literature with a high level of reproducibility and consistency especially at temperatures above 100°C, (Volkl and Alefeld, 1978). Those studies have included measuring the diffusion coefficient, solubility and permeability at different temperatures but only a few measurements have been made at room temperature (about 22°C), (Robertson, 1973, Yamakawa and Fujita, 1977, Altunoglu and Braithwaite, 1995). Low temperature diffusion measurements are particularly challenging because the coefficients are small and therefore permeation rates are correspondingly small.

In this work, nickel was chosen partly to validate the permeation technique but also to give an indication of precision. This is on the basis that there are no surface complications known when measuring the diffusivity and solubility for nickel (no corrosion involved), and, perhaps consequently, because the effects of inhomogeneities such as impurities and grain boundaries have been well studied.

As explained earlier, the frequency parameter introduced into the solutions of the differential equations describing diffusion enabled the determination of the diffusion and solubility coefficients from two different equations that describe the variation of the phase lag and amplitude ratio between the current and the hydrogen partial pressure with oscillation frequency. Thus, each value of, say, diffusion coefficient is the result of signal averaging around 15 cycles at each frequency and then fitting the variation of the phase lag and amplitude ratio with the expected relationship.

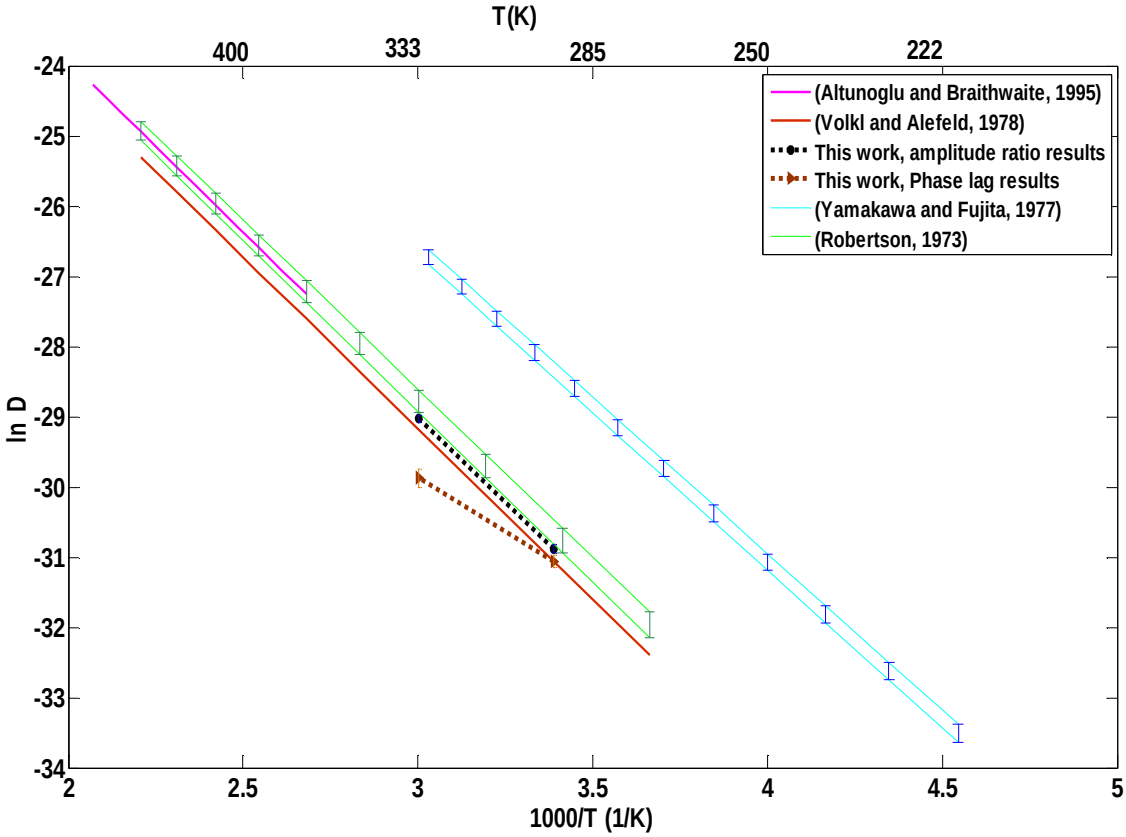

Figure 7-1: Hydrogen diffusion coefficients for pure nickel from the literature and this work.

Figure 7-1 shows that the diffusion coefficient results measured here at 22°C and 60°C are consistent with the general body of data on hydrogen transport in nickel at a range of temperatures. In the current work, the nickel specimen was 99% pure while in the work of the other authors it was at least 99.98% pure, (Robertson, 1973, Volkl and Alefeld, 1978, Yamakawa and Fujita, 1977). However, the values of the diffusion coefficient are not significantly different except for the values measured by Yamakawa and Fujita (1977) which are an order of magnitude higher than the results in this work at both 22°C and 60°C.

Table 7-1 shows that there is a high internal consistency of the diffusion and solubility coefficient values derived from the model developed in this work, using two different equations; the phase lag equation which is relatively independent of pumping rate effects, and the amplitude ratio equation which is affected by the net pumping rate, perhaps including adsorption on the walls of the chamber. It might be noted that the value of *D* at 60°C derived from the amplitude ratio fit was about twice that derived from the phase lag fit. The possible reason for this is that the walls of the vacuum

chamber give rise to a higher effective pumping rate at 60°C, thus resulting in an underestimate of β.

Temp.	**Fitting to**	***D*** **(m^2/s)**	***K*** **(mol H_2/m^3 $mbar^{0.5}$)**	***R^2***
22°C	Phase lag	$(3.3 \pm 0.55)\times10^{-14}$	-	0.9798
	Amplitude ratio	$(3.9\pm0.45)\times10^{-14}$	$(2.07\pm0.1)\times10^{-2}$	0.9382
	Amplitude ratio but using *D* from phase lag fit	-	$(2.16 \pm 0.08)\times10^{-2}$	0.9516
60°C	Phase lag fitting	$(1.1\pm0.3)\times10^{-13}$	-	0.9432
	Amplitude ratio fitting	$(2.5\pm0.28)\times10^{-13}$	$(3.05\pm0.25)\times10^{-2}$	0.9208
	Amplitude ratio but using *D* from phase lag fit	-	$(3.34\pm0.12)\times10^{-2}$	0.9476

Table 7-1: Permeation data from the experiments on nickel where *D* is the diffusion coefficient, (m^2/s) and *K* is the solubility coefficient (mol H_2/m^3 $mbar^{0.5}$).

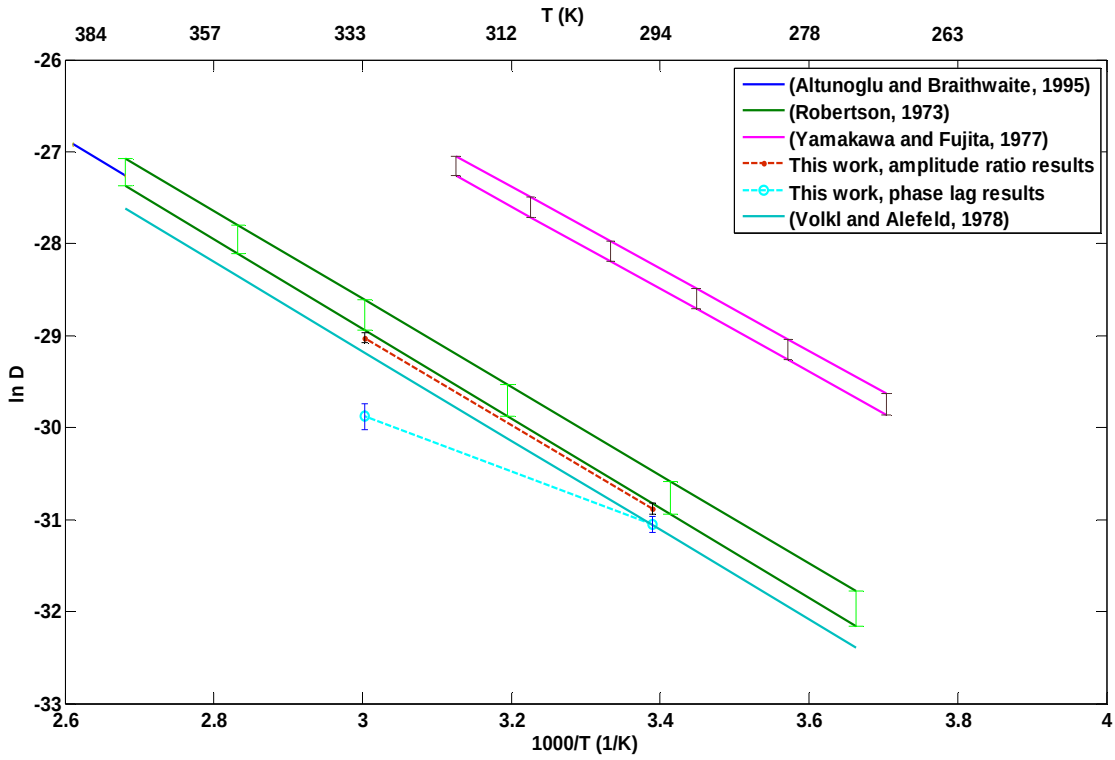

Figure 7-2: Hydrogen diffusion coefficients for pure nickel from the literature and this work between 273 and 373K.

Figure 7-2 shows a magnified plot of the relationship between the diffusion coefficient and absolute temperature for pure nickel between 273 and 373K and Table 7-2 shows the activation energies and pre-exponential factors corresponding to the plotted data. It is clear from the table that even though the uncertainty of derived activation energy in this work is much higher than those in the literature and the values of the pre-exponential factor are one order of magnitude different, the overall consistency among the values of the diffusion coefficient between the literature and this work is maintained. This is perhaps unsurprising given that the temperature range in the current work is very small. The most striking aspect of Figure 7-2 is that the data of Yamakawa and Fujita (1977) are in disagreement with all other workers in the temperature range in question. These authors measured the diffusion coefficient using a technique involving electrical resistivity change due to diffusion of hydrogen out of wire specimen, (Yamakawa and Fujita, 1977).

Reference	Temperature (K)	D_0 (m^2/s)	Q (J/mol)
Robertson (1973)	273-1669	$(6.44\pm0.35)\times10^{-7}$	40200±300
Yamakawa and Fujita (1977)	220-330	$(19\pm1.1)\times10^{-7}$	37190±130
Altunoglu and Braithwaite (1995)	373-623	$(7.12\pm0.12)\times10^{-7}$	40640
Volkl and Alefeld (1978)	≤ 627	4.80×10^{-7}	39340
This work, phase lag fit	295 and 333	$(2.15\pm2.14)\times10^{-8}$	25350±9630
This work, amplitude ratio fit	295 and 333	$(1.53\pm1.46)\times10^{-6}$	39940±4910

Table 7-2: Diffusion activation energy and pre-exponential coefficient for pure nickel from the literature and this work.

Figure 7-3 shows an Arrhenius plot of published solubility data along with the values measured in this work in the relevant temperature range. Table 7-3 shows the corresponding activation energies and solubility pre-exponential factors. As with the diffusion coefficient, the values measured here are consistent with the literature although the uncertainties in activation energy and pre-exponential factor are considerable.

In terms of evaluation the precision of the technique, the easiest comparison is with the work of Robertson (1973), Table 7-4.

Reference	**Temperature (K)**	**K_0 (mol H_2/m^3mbar$^{0.5}$)**	**Q_K (J/mol)**
Robertson (1973)	273-1669	5.01±0.25	14400±300
Altunoglu and Braithwaite (1995)	373-623	4.70±0.07	13610
This work, independently	295 and 333	0.88±0.70	7930±2840
This work, using *D* derived from phase lag fit	295 and 333	1.16±0.63	9370±1570

Table 7-3: Solubility activation energy and pre-exponential coefficient for pure nickel from the literature and this work.

Reference	$D_{60°C}$ **(m^2/s)**	$D_{22°C}$ **(m^2/s)**	$K_{60°C}$ **(mol $H_2/m^3 mbar^{0.5}$)**	$K_{22°C}$ **(mol $H_2/m^3 mbar^{0.5}$)**	$DK_{60°C}$ **(mol H_2/m.s.$mbar^{0.5}$)**	$DK_{22°C}$ **(mol H_2/m.s.$mbar^{0.5}$)**
Robertson (1973)	2.7×10^{-13} - 3.74×10^{-13}	4.1×10^{-14} - 5.84×10^{-14}	2.35×10^{-2} - 2.8×10^{-2}	1.18×10^{-2} - 1.42×10^{-2}	7.56×10^{-15} - 8.8×10^{-15}	5.85×10^{-16} - 6.93×10^{-16}
This work	1.51×10^{-13} - 2.09×10^{-13}	3.1×10^{-14} - 4.1×10^{-14}	3.01×10^{-2} - 3.38×10^{-2}	2.02×10^{-2} - 2.2×10^{-2}	4.54×10^{-15} - 7.06×10^{-15}	6.26×10^{-16} - 9.02×10^{-16}

Table 7-4: A comparison between Robertson's data (1973) and data from this work for nickel at 22ºC and 60ºC; values for this work are average between those found from phase and amplitude fits.

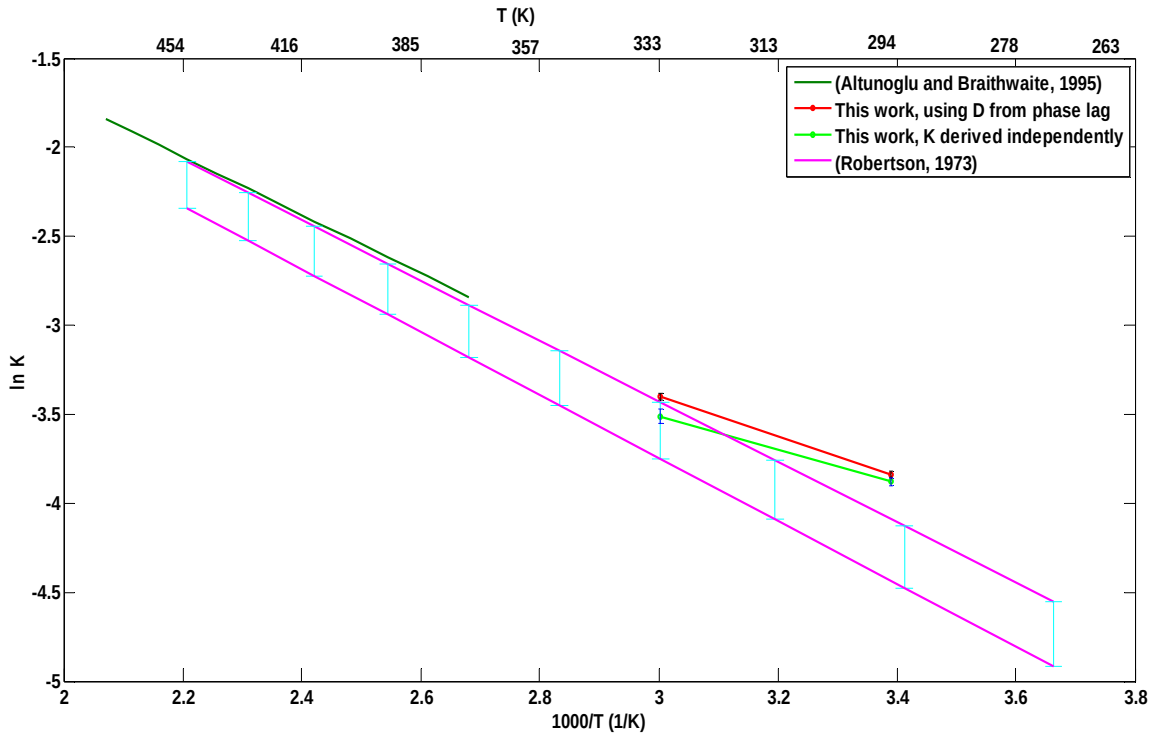

Figure 7-3: Hydrogen solubility coefficients for pure nickel from the literature and this work.

7.2 En24 Low Alloy Steel

When comparing with literature data, it is important to acknowledge that some authors have measured effective diffusion coefficients and solubilities, whereas others have specifically addressed surface or trapping effects.

The vast majority of hydrogen permeation related research in Ni-Cr-Mo low alloy steel of the type used here has focused on the quenched and tempered condition; this is mainly because the best mechanical properties for this alloy are obtained in such a condition. There are few studies with annealed samples, and the as-quenched condition has attracted little or no interest. A comparison between the literature values of the effective diffusion coefficient *D* in quenched and tempered AISI 4340 at room temperature and this work is shown in Table 7-5. Clearly there is only agreement amongst the authors within a factor of five, with some (e.g. Scully and Moran) showing rather high values and others (e.g. Griffiths et al) showing rather low values. It is difficult to attribute these differences to any aspect of the alloy condition since few authors give any details of the quenching and tempering process, so it can only be said that the changes reflect range of trapping effects to be expected in nominally identified

low alloy steels. The effective diffusion coefficient measured in the current work is a factor of five lower than even the lowest literature value, although it should be noted (Table 6-9) that it was not possible to get a suitable fit to the data using a surface equilibrium assumption. The diffusion coefficient obtained using a fit allowing for trapping is more in line with the literature data.

In the current work, three different heat-treated samples were used, and one sample was re-tested after de-solution treatment. The results are summarised in Table 7-6, where values of diffusion coefficients are taken as the mean of phase lag and amplitude ratio derived results, except for the quenched and tempered specimen for the surface equilibrium fit and the surface effects fit for all specimens (see Tables 6-9 to 6-11).

Reference	D (m^2/s)	Conditions
(Nanis and Namboodhiri, 1973)	2.38×10^{-11} at 295 K	Quenched from 1075K; Tempered at 622K for 2 hours
(Nanis and Namboodhiri, 1973)	2.17×10^{-11} at 295 K	Quenched from 1144K; Tempered at 504K for 2 hours
(Robinson and Hudson, 1990)	2.5×10^{-11} at 295 K	Quenched and tempered
(Scully and Moran, 1988a)	4.5×10^{-11} at 298±2 K	Tempered
(Griffiths et al., 1994)	1.1×10^{-11} at 295±0.3 K	Oil quenched and tempered
(Popov et al., 1994)	4.2×10^{-11} at 296±1 K	Bismuth layer electroplated
(Devanathan and Stachurski, 1963)	2×10^{-11} at 298±1 K	Tempered
(Scully and Moran, 1988b)	1×10^{-11} at 298±2 K	Tempered
(Dull and Nobe, 1982)	4.7×10^{-11} at 295 K	Tempered at 703K for 2 hours
(Dull and Nobe, 1982)	8.85×10^{-11} at 295 K	Tempered 923 K for 2 hours
This work, surface equilibrium fit	$(2.3\pm0.56)\times10^{-12}$ at 295 K	Quenched and Tempered
This work, trapping effects fit	$(3.2\pm0.8)\times10^{-11}$ at 295 K	Quenched and Tempered

Table 7-5: Literature values of the diffusion coefficient for quenched and tempered AISI 4340 and for quenched and tempered En24 from this work.

As can be seen from Table 7-6, for the surface equilibrium fit, the effective diffusion coefficient is quite low for the quenched specimen while it decreases when this specimen is tempered, the highest diffusion coefficient having been found for the

annealed specimen after hydrogen de-solution treatment. The low value of the effective diffusion coefficient in the quenched sample could be explained by the delay of hydrogen transport due to trapping effects which might be expected to be high in a non-tempered martensitic microstructure although the further decrease on tempering is somewhat surprising. The observed decrease in effective diffusion coefficient for martensitic over ferrite-pearlitic structures is in good qualitative agreement with Nanis and Namboodhiri (1973) who carried out permeation experiments at 22°C on annealed and quenched and tempered AISI 4340 and found an effective diffusion coefficient of 7.5×10^{-10} m^2/s for the annealed specimen and 2.38×10^{-11} m^2/s for the quenched and tempered one. Also, Dull and Nobe (1982) have measured effective diffusion coefficients in AISI 4340 in a number of heat-treatment conditions, including one annealed for 1 hour at 1143 K and two tempering temperatures of 813 K for 1 hour and 703 K for 2 hours (Table 7-5). Whereas there was little difference between the two tempering treatments ($D = 4.95\times10^{-11}$ m^2/s and 4.7×10^{-11} m^2/s), consistent with the work of Nanis and Namboodhiri (1973) (Table 7-5), these authors also found a significant increase in effective diffusion coefficient for annealed specimens, to 9.75×10^{-11} m^2/s.

Table 7-6 also illustrates the effect of taking into account surface and trapping parameters, the detailed information being summarised in Tables 6-9 to 6-11. Two general observations emerge from Tables 6-9 to 6-11. The first is that taking account of surface effects almost always resulted in a poorer fit to the data than for surface equilibrium, whereas trapping almost always gives rise to improved fits, often significantly so. The second observation is that taking account of surface effects results in a divergence of diffusion coefficients, whereas taking account of trapping effects gives rise to a convergence.

Condition	Annealed	Annealed (de-solution treated)	Quenched and Tempered	Quenched
Surface equilibrium fit	$(4.45\pm1.02)\times10^{-9}$	$(7.25\pm0.94)\times10^{-9}$	$(2.3\pm0.56)\times10^{-12}$	$(2.72\pm0.96)\times10^{-11}$
Trapping effects fit	$(4.4\pm0.96)\times10^{-10}$	$(7.74\pm1.07)\times10^{-10}$	$(3.2\pm0.8)\times10^{-11}$	$(7.9\pm1.2)\times10^{-12}$
Surface effects fit	$(1.22\pm1.7)\times10^{-8}$	$(3.5\pm1.2)\times10^{-7}$	$(2.52\pm0.34)\times10^{-12}$	$(2.8\pm1)\times10^{-11}$

Table 7-6: Hydrogen diffusion coefficient measurements for En24 at three heat treatment conditions; values are average between those found from phase and amplitude fits, (Table 6-9).

Condition	Annealed	Annealed (de-solution treated)	Quenched and Tempered	Quenched
Surface equilibrium fit	$(1.7\pm0.54)\times10^{-11}$	$(7.33\pm0.25)\times10^{-11}$	-	$(4.8\pm0.5)\times10^{-7}$
Trapping effects fit	$(4.2\pm1.3)\times10^{-9}$	$(6.37\pm1.65)\times10^{-9}$	$(1.22\pm0.6)\times10^{-7}$	$(3.28\pm0.94)\times10^{-5}$

Table 7-7: Hydrogen solubility coefficient, K (mol $H_2/m^3.mbar^{0.5}$), measurements for En24 at three different heat treatment conditions.

Table 7-7 summarises the solubility data from the current work, again averaging according to whether or not the diffusion coefficient was allowed to float. The main observation that can be made is the significant increase in solubility in the martensitic condition, whether or not tempered.

The solubility values in the literature for BCC iron and most steels are highly scattered, (Kiuchi and McLellan, 1983). Furthermore, many authors do not report solubility coefficients but many do report surface hydrogen concentrations along with some thermo-dynamic measure of the environment (hydrogen partial pressure or an

electrochemical potential), so some means of conversion is required in order to make comparisons.

If the hydrogen partial pressure is reported, Sievert's Law, can be used:

$$C = K\sqrt{P_{H_2}} \tag{7-1}$$

where P_{H_2} is the hydrogen partial pressure at the input surface, C is the surface concentration and K is the solubility coefficient.

If an electrochemical potential is given, hydrogen partial pressure can be found from the Nernst Equation, (Bockris and Reddy, 1970):

$$E = E_0 + \frac{RT}{F}\,pH - \frac{RT}{2F}\ln(P_{H_2}) \tag{7-2}$$

where E is the applied potential (volts), and E_0 is the standard potential for the hydrogen dissolution reaction, R is the universal gas constant (8.314 J/mol.K), T is the absolute temperature (K), and F is Faraday's constant (96485 C/mol).

In some studies, the potential is not available but the applied current density is given, and this can be related to the potential using the following equation, (Fontana, 1987):

$$\eta = \pm\beta_1 \log\frac{i}{i_0} \tag{7-3}$$

where η is the overvoltage, β_1 is the Tafel constant, i is the current density and i_0 is the exchange current density. Values of i_0 and β_1 can be found for a particular reaction and solution, (Fontana, 1987), and so the current density can be used to obtain the overvoltage and hence the potential.

Assuming the above relationships to hold, solubility coefficients for AISI 4340 from the literature can be compared with the findings in this work for En 24 as shown in Table 7-8.

Reference	***K* (mol $H_2/m^3.mbar^{0.5}$)**	**Condition**
Nanis and Namboodhiri (1973)	2.31×10^{-9}	Annealed
This work, surface equilibrium fit	$(1.7\pm0.54)\times10^{-11}$	Annealed
This work, surface equilibrium fit	$(7.33\pm0.25)\times10^{-11}$	Annealed, de-solution treated
This work, trapping effects fit	$(4.2\pm1.3)\times10^{-9}$	Annealed
This work, trapping effects fit	$(6.37\pm1.65)\times10^{-9}$	Annealed, de-solution treated
Nanis and Namboodhiri (1973)	5.56×10^{-8}	Quenched and tempered
Griffiths et al. (1994)	6.1×10^{-7}	Quenched and tempered
Dull and Nobe (1982)	3.454×10^{-6}	Quenched and tempered
This work, trapping effects fit	$(1.22\pm0.6)\times10^{-7}$	Quenched and tempered

Table 7-8: Solubility coefficients for AISI 4340 at room temperature from the literature compared to those derived in this work for En24.

Nanis and Namboodhiri (1973) reported values for annealed material and, as can be seen, the values obtained from the trapping fit from this work are rather more consistent than the less good fit given by the surface equilibrium assumption. The solubilities

obtained here are, nevertheless, somewhat higher than those measured by Nanis and Namboodhiri, although this is balanced by the somewhat lower diffusion coefficient measured here in comparison with the same work, Table 7-9.

Reference	***DK* (mol H_2/m.s.mbar$^{0.5}$); annealed condition**	***DK* (mol H_2/m.s.mbar$^{0.5}$); quenched and tempered condition**
Nanis and Namboodhiri (1973)	1.73×10^{-18}	1.3×10^{-18}
This work	$(3.17\pm1.4)\times10^{-18}$	$(3.9\pm0.48)\times10^{-18}$

Table 7-9: A comparison of the permeability *DK* (mol H_2/m.s.mbar$^{0.5}$) between Nanis and Namboodhiri's work and this work.

For quenched and tempered material, the value for the solubility coefficient measured here lies between the highest and lowest reported values, themselves ranging over almost two orders of magnitude. Again, the values measured here are around twice those measured by Nanis and Namboodhiri, although, this time there is not a compensating reduction in the diffusion coefficient. It is worth noting that the only two observations of solubility in both conditions (this work and Nanis and Namboodhiri, 19973) agree that there is a 20-30 fold increase in solubility coefficient between the annealed and quenched and tempered states.

The discrepancies in reported solubilities have been pointed out and discussed in the literature, (Volkl and Alefeld, 1978, Kiuchi and McLellan, 1983), and the suggested causes have included surface effects, the possible trapping of hydrogen atoms at such discontinuities and impurities, grain boundaries and dislocations, the nature of such traps (reversible and/or irreversible), and the experimental technique used for the permeation. For example, the electrochemical technique, though simple, might be misleading if the boundary conditions are not kept constant and determined correctly, (Turnbull, 1995, Volkl and Alefeld, 1978).

Trapping parameters, derived from fitting the results in this work to McNabb and Foster model, showed a good internal consistency, Table 7-10. The rate of releasing an atom from a trap, *p*, is very low in the quenched material increasing by three orders of magnitude in the tempered specimen and by a further five orders of magnitude in the annealed condition, consistent with the expectation that quenched material will have the deepest traps. Furthermore, the relatively slight decrease in *p* for the de-solution treated material is consistent with only the relatively shallow traps dominating behaviour, while some of the deeper traps, are cleared by the de-solution treatment.

The product of the rate of a trap capturing an atom per second and the density of traps per volume, *kN*, was highest in the annealed specimens and decreased for the quenched and the tempered specimen and further still for the as-quenched specimen. Although this is contrary to what might be expected (a greater density of more attractive traps in the quenched material) it might be noted that the residual diffusion coefficient (Table 6-10) also decreases between the three conditions. This behaviour is consistent with the residual diffusion coefficient being associated with irreversible traps, which can be accounted for using the Oriani equation 2-34. Using an average value for the annealed specimens, and supposing this to be equivalent to D_L (i.e. assuming no irreversible traps), values of $K_a N_x/N_L$ can be calculated for the as-quenched and the quenched and tempered material as 75.3 and 17.52, respectively.

Condition	Annealed	Annealed, de-solution treated	Quenched and Tempered	Quenched
***k.N* (s^{-1}), phase lag fit**	4.68±0.25	2.16±0.42	0.3±0.13	$(2.47\pm0.36)\times10^{-3}$
***k.N* (s^{-1}), amplitude ratio fit**	1.98±0.33	4.48±0.68	0.6±0.28	$(3.2\pm0.75)\times10^{-3}$
***p* (s^{-1}), phase lag fit**	0.54±0.26	0.31±0.08	$(2.98\pm1.5)\times10^{-4}$	$(1.21\pm1.05)\times10^{-7}$
***p* (s^{-1}), amplitude ratio fit**	0.95±0.21	0.09±0.02	$(1.4\pm0.86)\times10^{-4}$	$(6.68\pm1.17)\times10^{-6}$

Table 7-10: Hydrogen trapping parameters, *kN* and *p*, for En24 at three different heat treatment conditions.

Data for trapping parameters are rather difficult to come by, but Griffiths et al. (1994) have measured trapping parameters similar for those used here for a quenched and tempered AISI 4340 specimen. They used a model developed by Ferriss and Turnbull (1988) which took into consideration earlier models for trapping phenomena during hydrogen diffusion in metals, (Iino, 1982, McNabb and Foster, 1963, Leblond and Dubois, 1983a). Their results, (Griffiths et al., 1994), gave the density of traps $N = (2.1\pm0.5)\times10^{18}$ sites/m^3 and the trap site binding energy ΔE = -49±0.5 kJ/mol from which the ratio k/p can be found as follows, (Turnbull et al., 1989a, Turnbull and Carroll, 1990):

$$\frac{k}{p} N_L = \exp(-\frac{\Delta E}{RT}) \tag{7-4}$$

where ($N_L \approx 5.2\times10^{29}$ sites/m^3) is the density of lattice diffusion sites, (Turnbull and Carroll, 1990) giving a value of $\frac{k}{p} = 9.13\times10^{-22}$ m^3.

In the current work, it is only possible to obtain values for kN and p, so, the comparison between the results presented in Table 7-10 and the one by Griffiths et al. can only be achieved by comparing the ratio kN/p between the two studies; from the current study as presented in Table 7-10, $\frac{kN}{p} = 2055$ while, from Griffiths et al. (1994), $\frac{kN}{p} = 1920$ which is remarkably close.

By way of sensitivity analysis, the value of the diffusion coefficient for quenched and tempered AISI 4340 from Griffiths et al, $D = 1.1\times10^{-11}$ m^2/s, was implemented in the model developed in this work and the values of p and kN were re-calculated from the phase lag fit as $p = (3.53\pm0.81)\times10^{-4}$ (s^{-1}), $kN = 0.40\pm0.22$ (s^{-1}), and from the amplitude ratio fit as $p = (1.92\pm0.25)\times10^{-4}$ (s^{-1}), $kN = 0.71\pm0.16$ (s^{-1}). Using these new values, the ratio kN/p was calculated as about 2037 which is very close to the ratio calculated using the original results.

Chapter 8

Conclusions and Recommendations for Future Work

8.1 Conclusions

The oscillatory technique used in this study for the hydrogen permeation experiments through nickel and a low alloy steel along with the developed mathematical model proved to be a very effective method to calculate the hydrogen diffusion and solubility coefficients; the results for nickel showed a high consistency with the literature findings and the results for quenched and tempered En24 (equivalent to AISI 4340) were in a quite good agreement with the available data from the literature.

This technique, which included introducing the frequency as a new dimension into the solution for the differential equations describing permeation, enabled the distinction between surface equilibrium permeation and that including further surface and/or bulk kinetic effects (trapping).

Detailed comparison of the results for nickel with the literature at similar (low) temperatures has shown the technique to be more precise in its determination of diffusion coefficient and solubility giving values of $D = (3.6\pm0.5)\times10^{-14}$ m^2/s and $(1.8\pm0.29)\times10^{-13}$ m^2/s at 22°C and 60°C, respectively, and solubility of $K = (2.11\pm0.09)\times10^{-2}$ mol $H_2/m^3 mbar^{0.5}$ and $(3.2\pm0.18)\times10^{-2}$ mol $H_2/m^3 mbar^{0.5}$ at 22°C and 60°C, respectively. This improved precision is attributed to the use of flux into a high vacuum as the means of measurement as well as the very high degree of averaging possible using the oscillatory technique.

For the four conditions of En 24 steel studied, the permeation data are best described using a model that takes into account trapping effects. Input surface effects do not appear to play an important role in permeation in the conditions used here as evidenced by the very poor fit for the relevant model and by the insignificant phase lag measured between current and potential.

The effective diffusion coefficients for En24 steel measured in this work were comparable with those reported in the literature, although the comparisons can only sensibly be made for quenched and tempered material. For the few other studies in

which such a comparison is made, the current work concurs that annealed low alloy steel has significantly higher effective diffusion coefficient than has the quenched and tempered condition.

The solubility coefficients for En 24 steel measured in this work are broadly comparable with the measurements reported in the literature and, in the few cases where a comparison can be made, highly consistent with changes in heat treatment. The values for the solubility coefficient at 22°C are shown in Table 8-1:

Condition	Annealed	Annealed (de-solution treated)	Quenched and Tempered	Quenched
Solubility (mol $H_2/m^3 mbar^{0.5}$); trapping effects fit	$(4.2\pm1.3)\times10^{-9}$	$(6.37\pm1.65)\times10^{-9}$	$(1.22\pm0.6)\times10^{-7}$	$(3.28\pm0.94)\times10^{-5}$

Table 8-1: Solubility coefficients for En24 specimens studied in this work.

The diffusion coefficients for En24 steel measured here can be explained by a combination of reversible and irreversible trapping effects. The reversible effects are described by the following trapping parameters; $\frac{kN}{p} = 7$ for the annealed specimen, $\frac{kN}{p} = 834$ for the quenched and $\frac{kN}{p} = 2055$ for the quenched and tempered one. These values compare well with the only other reported measurement, this for the quenched and tempered condition (Griffiths et al, $\frac{kN}{p} = 1920$). The reversible trapping model yields a residual diffusion coefficient for each condition as follows; D = $(6\pm1)\times10^{-10}$ m^2/s for the annealed, $(7.89\pm1.2)\times10^{-12}$ m^2/s for the quenched and $(3.25\pm0.8)\times10^{-11}$ m^2/s for the quenched and tempered condition. Assuming a reference for the annealed material, a measure of the irreversibly trapped hydrogen ($K_a N_x/N_L$ in the Oriani model) can be obtained for the quenched and quenched and tempered conditions as 75.3 and 17.52, respectively.

8.2 Recommendations for Future Work

The oscillatory method has proven to be a very useful tool in the assessment of hydrogen permeation kinetics in low alloy steels. A number of immediate lines of investigation suggest themselves in the interest of addressing the key technological problem of improved hydrogen resistance:

- Carrying out permeation experiments on a wider range of low alloy steels and conditions (heat treatments, different phase compositions such as austenite, ferrite, martensite, and dislocation pile-up) and over a wider range of temperatures and hydrogen potential of industrial significance; it is acknowledged that the experimental rig needs to be modified for carrying out permeation experiments at temperatures higher than the boiling point of the electrolyte used for hydrogen charging.

- Introduction of specific surface effects on hydrogen transport, such as introducing coatings, corrosion layers, and pre-oxidation treatments.

Other studies related to the topic of hydrogen permeation that would be addressed in future work are listed below:

- Conducting micrographs and AFM (atomic force microscope) studies to explore the influence of grain sizes on hydrogen transport and what effects might evolve when static and dynamic stresses are applied.

- Use of finite element simulations to study the relationship between hydrogen permeation and residual and/or static and dynamic applied stresses along with the possible effects of temperature, fatigue and other fracture mechanisms.

- Investigating the possible application of the permeation technique for in-situ applications monitoring (e.g. crack initiation and propagation).

- Investigating the potential involvement of hydrogen protons, in addition to molecular and atomic hydrogen, in the permeation process.

References

Addach H, Bercot P, Rezrazi M and Wery M, (2005). "Hydrogen permeation in iron at different temperatures", Materials Letters, **59**, pp 1347– 1351.

Al-Faqeer F M and Pickering H W (2002) "Kinetics of electrochemical hydrogen absorption in metals." In Moody N R, Thompson A W, Ricker R E, Was G W and Jones R H (Eds.) *Hydrogen Effects on Materials Behaviour and Corrosion Deformation Interactions.* TMS (The Minerals, Metals and Materials Society), Wyoming.

Altunoglu A K and Braithwaite N S J, (1995). "The science and application of modulated permeation experiments", Journal of Alloys and Compounds, **231**, pp 302-306.

Bockris J O' M (1973) "On hydrogen damage and the electrical properties of interfaces." In Staehle R W, Hochmann J, McCright R D and Slater J E (Eds.) *Stress Corrosion Cracking and Hydrogen Embrittlement of Iron Base Alloys*. Houston.

Bockris J O' M, McBreen J and Nanis L, (1965). "The hydrogen evolution kinetics and hydrogen entry into alpha–iron", Journal of the Electrochemical Society, **112**, pp 1025-1031.

Bockris J O M and Reddy A K N (1970) *Modern Electrochemistry*, Plenum Press, New York.

Boes N and Zuchner H, (1976). "Electrochemical methods for studying diffusion, permeation and solubility of hydrogen in metals", Journal of the Less Common Metals, **49**, pp 223-240.

Bruzzoni P, Carranza R M, Lacoste J R C and Crespo E A, (1999). "Hydrogen diffusion in α-iron studied using an electrochemical permeation transfer function", Electrochimica Acta, **44**, pp 2693-2704.

Chambers A, Fitch R K and Halliday B S (1998) *Basic Vacuum Technology*, IOP Publishing Ltd, Bristol

Crank J (1975) *The Mathematics of Diffusion*. Oxford University Press, New York.

Cummings D L, Reuben R L and Blackburn D A, (1984). "The effect of pressure modulation on the flow of gas through a solid membrane: Permeation and diffusion of hydrogen through nickel", Metallurgical Transactions A, **15A**, pp 639-648.

Devanathan M A V and Stachurski Z, (1962). "The adsorption and diffusion of electrolytic hydrogen in palladium", Proceedings of the Royal Society of London, **A270**, pp 90-102.

Devanathan M A V and Stachurski Z, (1963). "A technique for the evaluation of hydrogen embrittlement characteristics of electroplating baths", Journal of the Electrochemical Society, **110**, pp 886-890.

Devanathan M A V and Stachurski Z, (1964). "The mechanism of hydrogen evolution on iron in acid solutions by determination of permeation rates", Journal of the Electrochemical Society, **111**, pp 619-623.

Dull D L and Nobe K, (1982). "Hydrogen trapping in Ferrovac E-iron, mild steel and 4340 steel", Werkstoffe und Korrosion, **33**, pp 439-448.

Ebisuzaki Y, Kass W J and O'Keeffe M, (1967). "Diffusion and solubility of hydrogen in single crystals of Nickel and Nickel—Vanadium alloy", Journal of Chemical Physics, **46**, pp 1378-1381.

Elhamid M H A, Ateya B G and Pickering H W, (2000). "Determination of the rate constants of hydrogen absorption into metals", Journal of the Electrochemical Society, **147**, pp 2959-2963.

Ferriss D H and Turnbull A, (1988). "Analysis of reversible and irreversible trapping in metals", NPL Report DMA A, pp 154.

Fontana M G (1987) *Corrosion Engineering*. McGraw-Hill Book Company, Singapore.

Garet M, Brass A M, Haut C and Guttierez-Solana F, (1998). "Hydrogen trapping on non metallic inclusions in Cr-Mo low alloy steels", Corrosion Science, **40**, pp 1073-1086.

Griffiths A J, Hutchings R B and Turnbull A (1994) "Hydrogen uptake and transport in low alloy steels." *Second International Conference on Interaction of Pipeline Steels with Hydrogen in Petroleum Industry Pressure Vessel and Pipeline Service*. Vienna.

Hirth J P, (1980). "Effects of hydrogen on the properties of iron and steel", Metallurgical Transactions, **11A**, pp 861-890.

Iacoviello F, Galland J and Habashi M, (1998). "A thermal outgassing method (T.O.M) to measure the hydrogen diffusion coefficients in austenitic, austeno-ferritic and ferritic-perlitic steels", Corrosion Science, **40**, pp 1281-1293.

Iino M, (1982). "A more generalised analysis of hydrogen trapping", Acta Metallurgica, **30**, pp 367-375.

Iyer R N, Pickering H W and Zamanzadeh M, (1989). "Analysis of hydrogen evolution and entry into metals for the discharge-recombination process", Journal of the Electrochemical Society, **136**, pp 2463-2470.

Johnson E W and Hill M L, (1960). "Hydrogen in cold worked iron-carbon alloys and the mechanism of hydrogen embrittlement", Transactions of the Metallurgical Society of AIME, **218**, pp 1104-1112.

Kim C D and Wilde B E, (1971). "Kinetics of hydrogen absorption into iron during cathodic hydrogen evolution", Journal of the Electrochemical Society, **118**, pp 202-206.

Kiuchi K and McLellan R B, (1983). "The solubility and diffusivity of hydrogen in well-annealed and deformed iron", Acta Metallurgica, **31**, pp 961-984.

Leblond J B and Dubois D, (1983a). "A general mathematical description of hydrogen diffusion in steels—I. Derivation of diffusion equations from Boltzmann-type transport equations", Acta Metallurgica, **31**, pp 1459-1469.

Leblond J B and Dubois D, (1983b). "A general mathematical description of hydrogen diffusion in steels—II. Numerical study of permeation and determination of trapping parameters", Acta Metallurgica, **31**, pp 1471-1478.

Lee J-L and Lee J-Y, (1982). "The hydrogen solubility in AISI 4340 steel in the temperature range of 298 to 873 K and atmospheric hydrogen pressure", Journal of Materials Science Letters, **1**, pp 489-492.

Manolatos P, Jerome M, Duret-Thual C and Coze J L, (1995). "The electrochemical permeation of hydrogen in steels without palladium coating. Part I: interpretation difficulties", Corrosion Science, **37**, pp 1773-1783.

Maroef I, Olson D L, Eberhart M and Edwards G R, (2002). "Hydrogen trapping in ferritic steel weld metal", International Materials Reviews, **47**, pp 191-223.

McBreen J, Nanis L and BecK W, (1966). "A method for determination of the permeation rate of hydrogen through metal membranes", Journal of the Electrochemical Society, **113**, pp 1218-1222.

McCright R D (1973) "Effects of environmental species and metallurgical structure on the hydrogen entry into steel." In Staehle R W, Hochmann J, Mccright R D and Slater J E (Eds.) *International Conference on Stress Corrosion Cracking and Hydrogen Embrittlement of Iron based alloys*. Houston.

McNabb A and Foster P K, (1963). "A new analysis of the diffusion of hydrogen in iron and ferritic steels", Metallurgical Transactions, **227**, pp 618-627.

Merrick R D, (1989). "An overview of hydrogen damage to steels at low temperatures", Materials Performance, February, pp 53-55.

NACE, (1977). "Testing of metals for resistance to sulphide stress cracking at ambient temperature", Standard TM-01-77, NACE Houston.

NACE, (1984). "Sulphide stress cracking resistant metallic materials for oil field equipment", Standard MR-01-75, NACE Houston.

NACE, (2005). "Laboratory testing of metals for resistance to sulphide stress cracking and stress corrosion cracking in H_2S environments", Standard TM-01-77-2005, NACE Houston.

Nagano M, (1982). "Hydrogen diffusivity in high purity alpha iron", Scripta Metallurgica, **16**, pp 973-976.

Nanis L and Namboodhiri T K G (1973) "Analysis of the permeation technique for the study of hydrogen entry into iron-base alloys." In Staehle R W, Hochmann J, Mccright R D and Slater J E (Eds.) *Stress Corrosion Cracking and Hydrogen Embrittlement of Iron Base Alloys*. Houston.

Newman J F and Shreir L L, (1969). "Role of hydrides in hydrogen entry into steel from solutions containing promoters", Corrosion Science, **9**, pp 631-641.

Ningshen S, Uhlemann M, Schneider F and Khatak H S, (2001). "Diffusion behaviour of hydrogen in nitrogen containing austenitic alloys", Corrosion Science, **43**, pp 2255-2264.

Oriani R A, (1970). "The diffusion and trapping of hydrogen in steel", Acta Metallurgica, **18**, pp 147-157.

Owczarek E and Zakroczymski T, (2001). "Hydrogen transport in a duplex stainless steel", Acta Materialia, 4**8**, pp 3059-3070.

Perng T P and Altstetter C J, (1986). "Effects of deformation on hydrogen permeation in austenitic stainless steels", Acta Metallurgica, **34**, pp 1771-1781.

Perng T P and Altstetter C J, (1988). "Effects of water vapour and hydrogen sulfide on hydrogen permeation in stainless steels", Acta Metallurgica, **36**, pp 1251-1260.

Popov B N, Zheng G and White R E, (1994). "Surface treatment for inhibition of corrosion and hydrogen penetration of type 718 alloy", Corrosion Science, **50**, pp 613-619.

Pyun S I and Oriani R A, (1989). "The permeation of hydrogen through the passivating films on iron and nickel", Corrosion Science, **29**, pp 485-496.

Robertson W M, (1973). "Hydrogen permeation, diffusion, and solution in nickel", Zeitschrift fuer Metallkunde, **64**, pp 436-443.

Robinson M J and Hudson D R J, (1990). "Measurements of hydrogen concentrations in BS4360 grade 50D carbon manganese steel using an electrochemical probe", British Corrosion Journal, **25**, pp 279-284.

Santos D S D and Miranda P E V D, (1998). "Hydrogen solubility in amorphous and crystalline materials", International Journal of Hydrogen Energy, **23**, pp 1011-1017.

Scully J R and Moran P J, (1988a). "The influence of strain on hydrogen entry and transport in a high strength steel in sodium chloride solution", Journal of the Electrochemical Society, **135**, pp 1337-1348.

Scully J R and Moran P J, (1988b). "Influence of strain on the environmental hydrogen-assisted cracking of a high-strength steel in sodium chloride solution", Corrosion, **44**, pp 176-185.

Stroud K A (1996) *Further Engineering Mathematics*. MacMillan Press Ltd, London.

Timmins P F (1997) *Solutions to Hydrogen Attack in Steels*. ASM International, Materials Park, Ohio.

Turnbull A (1995) "Standardisation of hydrogen permeation measurement by the electrochemical technique." In Turnbull A (Ed.) *Hydrogen Transport and Cracking in Metals.* National Physical Laboratory, The University Press, Cambridge.

Turnbull A and Carroll M W, (1990). "The effect of temperature and H_2S concentration on hydrogen diffusion and trapping in a 13% chromium martensitic stainless steel in acidified NaCl", Corrosion Science, **30**, pp 667-679.

Turnbull A, Carroll M W and Ferriss D H, (1989a). "Analysis of hydrogen diffusion and trapping in a 13% chromium martensitic stainless steel", Acta Metallurgica, **37**, pp 2039-2064.

Turnbull A, Maria M S D S and Thomas N D, (1989b). "The effect of H_2S concentration and pH on hydrogen permeation in AISI 410 stainless steel in 5% NaCl", Corrosion Science, **29**, pp 89-104.

Volkl J and Alefeld G (1978) "Diffusion of hydrogen in metals." In Alefeld G and Volkl J (Eds.) *Hydrogen in Metals*. Springer, Berlin.

Warren D, (1987). "Hydrogen effects on steel", Materials Performance, January, pp 38-48.

Yamakawa K and Fujita F E, (1977). "Diffusion of hydrogen in hydrogen-quenched nickel", Japanese Journal of Applied Physics, **16**, pp 1747-1752.

Yen S K and Huang I B, (2003). "Critical hydrogen concentration for hydrogen-induced blistering on AISI 430 stainless steel", Materials Chemistry and Physics, **80**, pp 662-666.

Yen S K and Shih H C, (1988). "A mathematical solution to the determination of the permeation rate of hydrogen through metal membrane", Journal of the Electrochemical Society, **135**, pp 1169-1170.

Zhang T-Y and Zheng Y-P, (1998). "Effects of absorption and desorption on hydrogen permeation -I. Theoretical modeling and room temperature verification", Acta Materialia, **46**, pp 5023-5033.